Copyright

by

Zheren Ma

2017

The Dissertation Committee for Zheren Ma Certifies that this is the approved version of the following dissertation:

COST-CONSCIOUS CONTROL STRATEGIES FOR WIND TURBINE SYSTEMS

Committee:

Dongmei Chen, Supervisor

Ross Baldick

Dragan Djurdjanovic

Raul G. Longoria

Ronald Barr

Cost-Conscious Control Strategies for Wind Turbine Systems

by

Zheren Ma, B. E.

Dissertation

Presented to the Faculty of the Graduate School of

The University of Texas at Austin

in Partial Fulfillment

of the Requirements

for the Degree of

Doctor of Philosophy

The University of Texas at Austin

May 2017

Acknowledgements

First, I would like to express my sincere gratitude to my academic supervisor, Dr. Dongmei Chen. With her help and encouragement, I was able to overcome difficulties in research and successfully completed this dissertation. Despite busy work and schedule, she is always willing to provide continuous guidance both for my research and career. This dissertation will not be possible without her support.

Second, I would also like to thank the professors on my Ph.D. defense committee: Dr. Ross, Dr. Djurdjanovic, Dr. Longoria and Dr. Barr. I appreciate your feedback and suggestions for my dissertation. I also took three classes lectured by the committee professors. From their lectures, I gained valuable knowledge that was very helpful to my research.

Third, I appreciate all the help from my friends in our research group. I learned a lot through discussions with these smart minds. They are always willing to help and collaborate. I will never forget the days when we discussed and learned together.

Finally, I would like to thank my parents. Whenever I suffered from setbacks, you always stood by me, comforted me, and helped me overcome difficulties. Without your support, I would not be able to get where I am today. Thank you so much for the selfless love!

This research was supported by National Science Foundation (NSF) CAREER Award CMMI-1056020, "CAREER: Control of Integrated Wind Turbine and Rechargeable Battery Systems" and by NSF Award CMMI-1334698, "Collaborative Research: Control of Reconfigurable Microgrids with Significant Renewable Power Sources".

Cost-Conscious Control Strategies for Wind Turbine Systems

Zheren Ma, Ph.D.

The University of Texas at Austin, 2017

Supervisor: Dongmei Chen

Wind energy is one of the most abundant renewable energy sources that can meet future energy demands. Despite its fast growth, wind energy is still a marginal player in electricity generation. The key issues preventing wider deployment of wind turbines include low energy conversion efficiency, high maintenance cost, wind intermittency and unpredictability etc. These issues lead to considerably higher cost of wind power compared to that of traditional power sources. This work is focused on control designs to overcome the above challenges.

First, control algorithms are developed for energy capture maximization. During partial load operation, wind turbine rotor speed is continuously adjusted to remain optimal operation by manipulating the electromagnetic torque applied to the generator. In this dissertation, a dynamic programming based real-time controller (DPRC) and a gain modified optimal torque controller (GMOTC) are developed for faster convergence to optimal power operation under volatile wind speed and better robustness against modeling uncertainties.

Secondly, fatigue loading mitigation techniques are developed to reduce the maintenance cost of a wind turbine. During partial load operation, a generator torque-based fatigue mitigation method is devised to reduce the impact of exacerbated tower

bending moments associated with the resonance effect. During full load operation, a $\mathcal{H}_2$ optimization has been carried out for gain scheduling of a Proportional-Integral blade pitch controller. It improves speed regulation and reduces drivetrain fatigue loading with less oscillations of turbine rotor speed and generator torque.

Thirdly, battery energy storage systems (BESS) have been integrated with wind turbines to mitigate wind intermittence and make wind power dispatchable as traditional power sources. Equipped with a probabilistic wind speed forecasting model, a new power scheduling and real-time control approach has been proposed to improve the performance of the integrated system.

Finally, control designs are oriented to wind turbine participation in grid primary frequency regulation. The fast active power injection/absorption capability of wind turbine enables it to rapidly change its power output for stablizing the grid frequency following an sudden power imbalance event. In addition to quick response to grid frequency deviation event, the proposed controller guarantees turbine stability with smooth control actions.

Table of Contents

List of Tables

List of Figures

Chapter 1: *Background and Introduction*

1.1 WIND ENERGY

Wind energy, as a clean and widely distributed resource, has been considered as one of the most promising renewable sources to generate electricity. The worldwide potential of wind power is more than 400 terawatts that is almost 20 times what the entire human population needs [1]. As shown in Figure 1.1, the installed wind power capacity has been experiencing an annual increase rate of nearly 21% from 59.1 GW in 2005 to 486.7 GW in 2016 [2]. Wind energy industry is expected to keep growing rapidly in the next few decades. In 2006, President Bush emphasized the nation's need for greater energy efficiency and a more diversified energy portfolio. This led to a collaborative effort to explore a modeled energy scenario in which wind provides 20% of U.S. electricity by 2030 [3]. In 2015 Paris Climate Change Conference, 195 nations reached a landmark accord that will commit nearly every country to lowering planet-warming greenhouse gas emissions to help stave off the most drastic effects of climate change [4]. This deal is a signal to global energy markets, triggering a fundamental shift away from investment in coal, oil and gas as primary energy sources toward zero-carbon energy sources like wind power. According to the new wind energy agenda from American Wind Energy Association [5], 7 GW of new wind projects will be installed per year from 2017 through 2020 and the annual wind energy generation will be doubled in the US by 2020. In Europe, 230 GW of wind capacity are expected to be installed by 2020, which will produce up to 17% of the EU's electricity [6]. As a wind power giant, China's installed wind capacity will grow from 115.6 GW to 347.2 GW by 2025 according to [7]. Globally, wind installations are expected to reach 962.6 GW by the end of 2025.

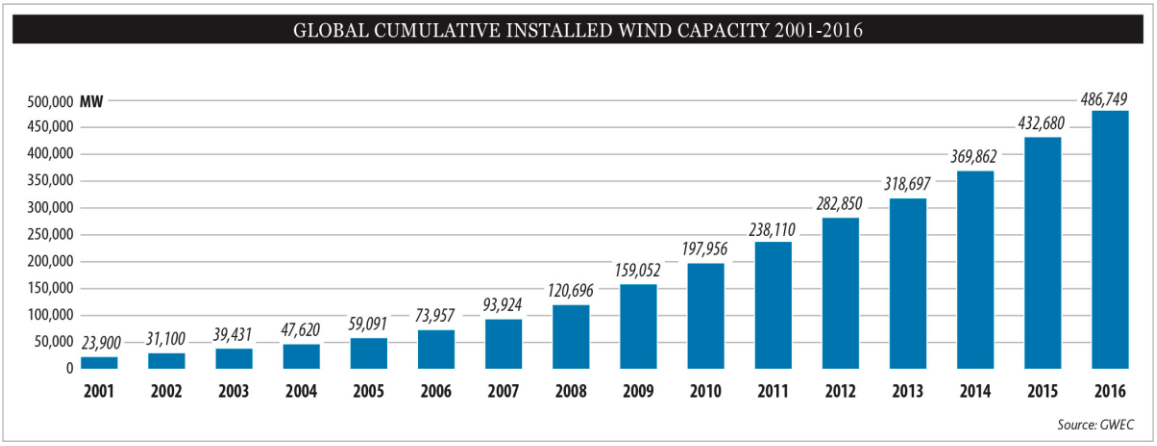

Figure 1.1: Global wind power cumulative capacity.

Despite its fast growth, wind energy is still a marginal player in electricity generation. As shown in Figure 1.2, wind energy only accounts for about 5.6% of the total energy generation in the United States by the end of 2016 [8]. To give wind power a fair chance in the fierce competition against already well-established energy sources, it is necessary to lower the cost associated with wind energy, which is considerably higher than that of fossil-fuel or nuclear power generation [9].

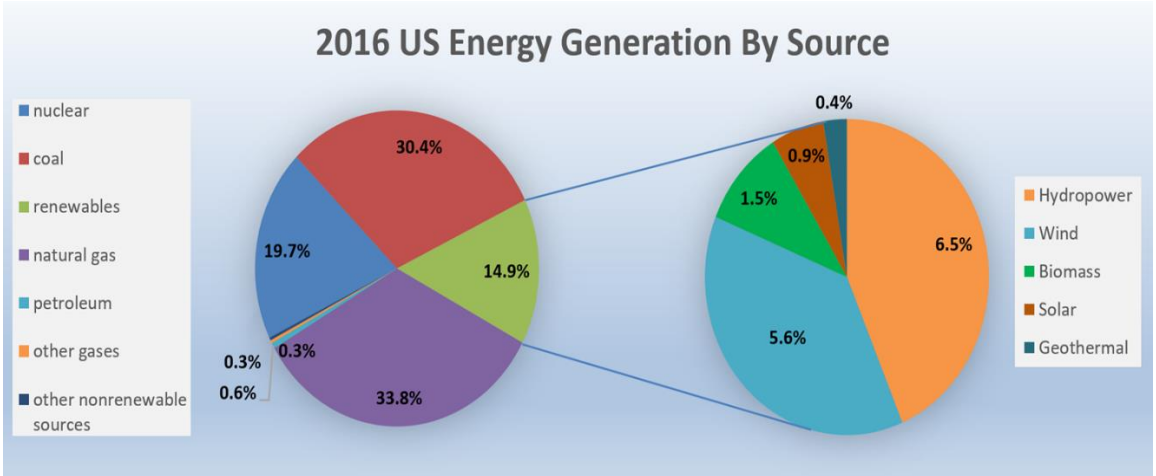

Figure 1.2: 2016 U.S. energy chart.

Low energy conversion efficiency is one of significant factors that cut down the revenue of a wind farm. Additionally, fatigue loads and mechanical stress lead to operation and maintenance costs that constitute a sizeable share of the total annual costs of a wind turbine. It can easily make up 20%-35% of the total levelized cost per kWh produced over the lifetime of the turbine [10]. Another challenge that prevents wider deployment of wind energy is wind intermittency and unpredictability, which is a major barrier to wind power dispatch. On one hand, wind energy only works when it is windy. On the other hand, too much wind may create more energy than the system can handle. Inconsistent and unreliable power supply poses a challenge for grid integration of wind energy. Traditionally, wind turbine provides oscillatory power to the grid under volatile wind speed. Wind power is considered to be disturbances or negative loads to the grid. As wind energy penetration increases, the frequency regulation burden on conventional generators also increases since wind energy not only has no contribution to frequency regulation, but also introduces oscillatory power that weakens frequency stability of the grid. Grid stability is a big concern that prevents higher wind energy penetration. Addressing the aforementioned challenges will make wind energy a more competitive player in electricity generation.

1.2 WIND TURBINE BASICS

A wind turbine is a revolving device that converts wind's kinetic energy into electrical power that can be fed into the grid. As shown in Figure 1.3, wind turbines can be configured to rotate about either a vertical or a horizontal axis. Therefore, wind turbines can be categorized into two major types, horizontal-axis wind turbine (HAWT) and vertical-axis wind turbines (VAWT).

(a) HAWT

(b) VAWT

Figure 1.3: Configurations of vertical-axis wind turbine (VAWT) and horizontal-axis wind turbine (HAWT).

Extensive comparisons between the two types have been discussed in [11]–[13]. In general, the maximum aerodynamic efficiency of any vertical-axis wind turbine (VAWT) is 15-25% lower than available horizontal-axis wind turbine (HAWT) designs [14]. The savings that a VAWT may enjoy due to lower drivetrain and maintenance costs are unlikely to balance the lower energy capture and higher initial rotor costs. Therefore, the HAWT configuration is more common and preferred for modern wind turbines [15]. The major components of a HAWT are shown in Figure 1.4:

1. Tower: The tower supports the entire wind turbine structure and absorbs the dynamic loads caused by volatile wind speeds. Since wind speed increases as height increases, a taller tower can capture more wind energy at the expense of more severe dynamic loads.

2. Rotor and blades: A turbine rotor consists of a hub and blades. Most wind turbine has two or three blades. The wind inflow causes aerodynamic forces on the turbine blades and spins the turbine rotor. Wind energy is converted to rotational kinetic energy of the turbine rotor.
3. Nacelle and drivetrain: A nacelle with drivetrain is on the top of turbine tower. A low-speed shaft connects the turbine rotor to the gearbox, which increases the rotational speed by the gear ratio. The speed transmission is completed by a high-speed shaft that connects the gearbox to the generator.
4. Generator: The generator converts kinetic energy to the electrical power, which is injected to the grid through a power converter.

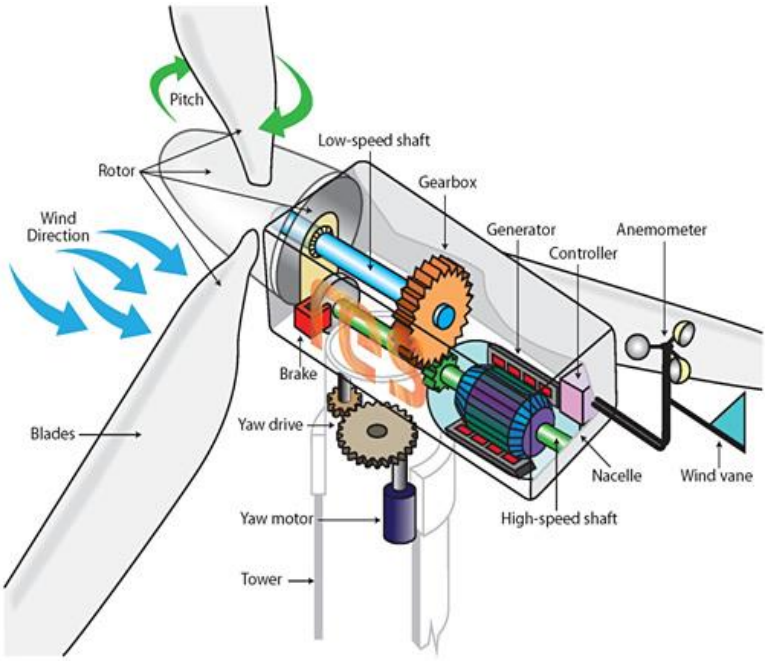

Figure 1.4: Components of a horizontal-axis wind turbine.

Wind speed and direction are measured by the anemometer and wind vane mounted on the top of the turbine tower. The wind causes lift and drag forces on the blades which subsequently generate a torque and turn the blades. Then, the blades turn the low-speed shaft inside the nacelle. The low-speed shaft goes into a gearbox that increases the rotational speed, which is subsequently transmitted to the generator by the high-speed shaft. Finally, the generator converts the mechanical power into electrical power. As the power output of generator may not be at the nominal frequency of the grid, power electronic converters are used for interfacing the electrical machine with the grid. As shown in Figure 1.5, the power is converted and transmitted from the wind to the grid by the wind turbine and its associated power electronics.

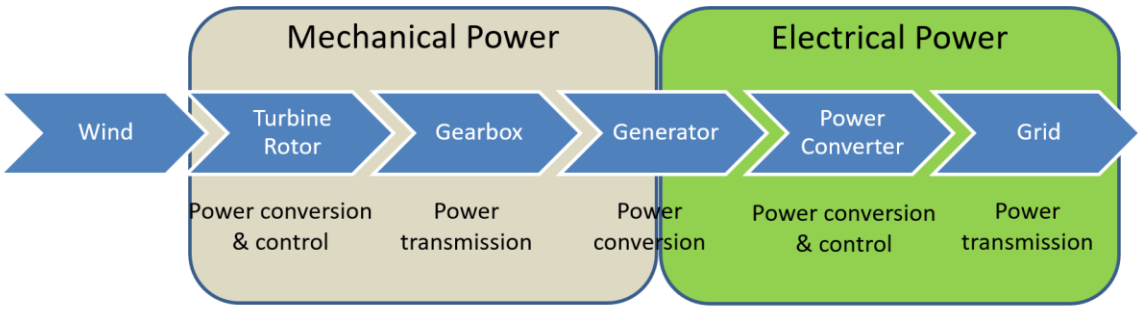

Figure 1.5: Power conversion and transmission from the wind to the grid.

There are four major types of generators: squirrel-cage induction generator, wound rotor induction generator, doubly fed induction generator and synchronous generator with full scale converter. The wind turbines with the above four types of generators are known as Type 1, 2, 3, 4, respectively. A wind turbine with a squirrel-cage induction generator (SCIG) operates at a fixed rotational speed corresponding to the frequency of the electrical grid. The fixed speed operation results in lower wind energy

conversion efficiency. A 10% speed variation can be achieved by using a wound rotor induction generator. The employment of a doubly fed induction generator with a variable frequency alternating current excitation in the rotor circuit, allows a turbine speed variation of 40% above and below the synchronous speed [16]. Due to the balance between cost and flexibility of operation, this type of generators have been widely used in the wind energy industry [17]. To completely overcome speed variation limit, a full-scale frequency converter is equipped with a synchronous generator. With this technique, the turbine rotor speed can be completely independent from the grid frequency. This allows more flexibility in turbine structure and control design. As the speed variation ability of a generator increases, the wind turbine is more capable of adjusting the rotor speed under varying wind turbine, resulting in more power extracted from the wind. However, the improvement of power conversion efficiency is at the expense of higher generator complexity and cost.

Based on the power characteristics for high wind speeds, wind turbines can be classified into two major types: pitch-regulated and stall-regulated. Under high wind speeds, a stall-regulated system relies on the blade aerodynamic design to avoid high aerodynamic torque or over-speeding of a wind turbine. The blade pitch angle remains unchanged during turbine operation. On the other hand, a pitch-regulated system actively controls the blade pitch angle to regulate the rotor speed around its rated value. As a result, the power output of a pitch-regulated wind turbine remains at a constant level under high wind speeds, while a stall-regulated wind turbine generates less than the rated power under high wind speeds [18]. Most modern wind turbines are variable-speed and variable-pitch, which enable maximized wind energy extraction comparing to old wind turbines with constant-speed and constant-pitch [19]. This work will be focused on control designs for variable-speed and variable-pitch wind turbines.

Due to the requirements in speed control, wind turbine operation is separated into three regions as show in Figure 1.6. In Region 1, the power generation is halted because the wind speed is below the cut-in speed and the available wind power is too small to compensate for the friction and operational costs. In Region 2, the wind turbine operates with partial load below the rated power. Therefore, Region 2 is also called the partial load region. In Region 3, also known as full load region, the power generation reaches its rated value and tries to maintain at that value. A blade pitch controller is used for speed regulation that adjusts the generator speed around its rated value. When the wind speed exceeds the cut-out speed, the turbine is shut off to prevent structural damages. Due to restrictions on acoustic noise emission, generator speed must be regulated to limit the blade tip speed below 80 m/s [20]. Therefore, the rated speed of a wind turbine decreases as the rotor diameter increases.

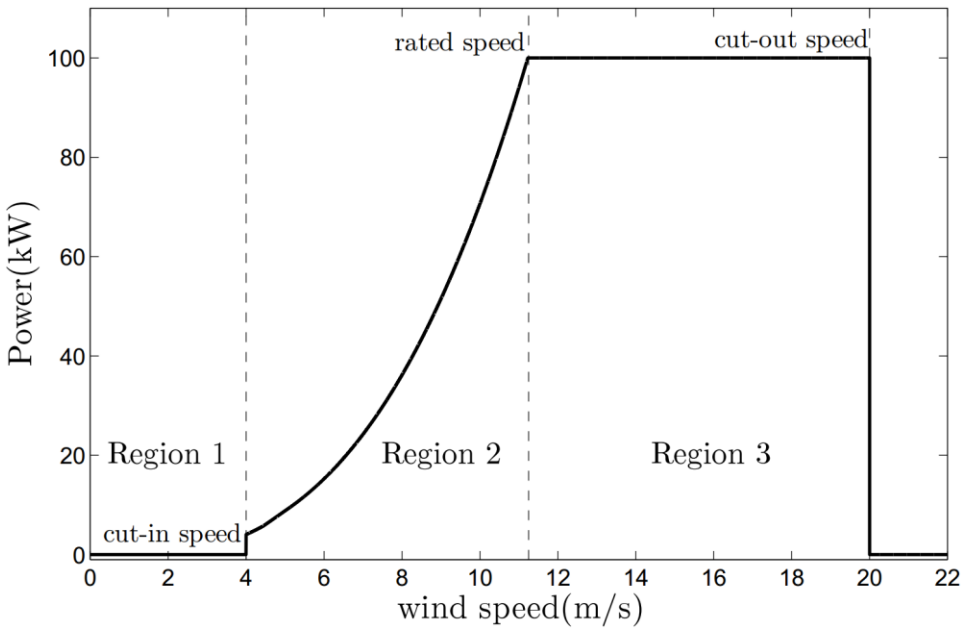

Figure 1.6: The ideal power conversion curve for a 100 kW wind turbine.

The wind turbine control system plays a crucial role in reducing the cost associated with wind energy. In general, there are three major manipulated control variables: the yaw angle, the generator torque and the blade pitch angle. The yaw system is actively controlled for adjusting the wind turbine orientation towards the wind direction. By minimizing the misalignment between the wind speed direction and wind turbine pointing direction, the power output is optimized and non-symmetrical loads are minimized. Generator torque and blade pitch angle are controlled to adjust the rotor speed, forces and torques acting on the turbine structures for optimizing wind turbine operation.

Numerous control objectives are considered when controlling a wind turbine. First, higher efficiency of energy conversion is desirable to extract as much energy out of wind turbine as possible. Load mitigation is another important objective to ensure safe operation, reduce the maintenance cost and extend the useful life of a wind turbine. Considering grid connection, predictable and consistent power output is preferable. In addition, the capability of fast active power injection/absorption is beneficial for maintaining frequency stability. These objectives, however, may conflict with one another. The wind turbine control system should be adjusted to find a well-balanced compromise among the control objectives. The next four sections will cover literature reviews regarding different topics investigated throughout this dissertation. Section 1.3 is focused on the studies related to enhancing energy capture during wind turbine partial load operation. Section 1.4 discusses fatigue loading mitigation for both partial load and full load operations of a wind turbine. Section 1.5 covers latest research advances in terms of power dispatch of intermittent wind power. Section 1.6 presents recently developed grid connected wind turbine technologies for frequency regulation. Finally, Section 1.7 summarizes the main contributions of this dissertation.

1.3 WIND ENERGY CAPTURE MAXIMIZATION

Higher energy conversion efficiency is desired for lowering the cost of wind energy. The power curve under a series of wind speeds for a typical 100kW wind turbine is shown in Figure 1.7, where λ is the tip speed ratio (TSR), defined as the ratio of turbine rotor tip speed over the wind speed, V_w. As the red dash line indicates, there exists a fixed optimal TSR, where the energy capture is maximized. As wind speed varies, the rotor speed needs to be controlled so that the TSR could seek its optimal value along the dashed line.

Research geared towards increasing wind energy capture has focused on exploring control algorithms to improve wind turbine efficiency, particularly for operation in the partial load region, where the generator operates below its rated power and the turbine speed varies significantly. Several maximum power point tracking (MPPT) methods have been developed to track the optimal TSR. In [21], TSR feedback control is designed for direct optimal TSR tracking. This controller is intuitive and simple for implementation. However, the direct TSR feedback approach does not consider the system nonlinearity which often leads to poor tracking performance. A standard torque controller (STC) has been developed and widely used for commercial wind turbines [21], [22] during partial load operation. The commanded generator torque of STC is proportional to the square of generator speed with a proportional control gain that is determined based on the wind turbine model. With an ideal wind turbine model, an optimal control gain can be obtained. The STC will allow the wind turbine to track the corresponding optimal reference tip speed ratio (TSR) that maximizes energy capture. However, the STC does not consider the wind speed measurement in its control design [23], and takes long time to converge to its optimal operating condition. Therefore, the STC does not effectively track the reference TSR under highly varying wind inflow. To

accelerate the controller's convergence to the turbine reference TSR, an optimally tracking rotor (OTR) controller was proposed [24]. Based on different wind speed measurements, the OTR adjusts the generator torque to assist in rotor acceleration and deceleration, thereby expediting the turbine's response under highly varying wind speed. A direct speed controller (DSC) was also developed using wind inflow information to improve the tracking performance of the reference TSR [25], [26].

Despite their effectiveness in accelerating turbine's response under high wind speed variation, the control gain and reference TSR employed by OTR and DSC are derived based on an ideal wind turbine model. Consequently, they are not robust against modeling uncertainties. It has been found that the simulation-derived reference TSR and torque control gain can deviate from their actual optimal values due to the aero-elastic response of turbine blades and the stochastic non-uniform wind inflow [27]. Experimental results from [28], [29] also confirm that there exists a large difference between the selected torque control gain and its true value because of the model-plant mismatch or structural degradation over time. To address this issue, adaptive algorithms have been developed to improve the controller robustness against modeling uncertainties [28], [29]. However, in order to eliminate the influence of volatile wind speeds, traditional adaptive gain-scheduling algorithms need to evaluate the average system performance over a long time horizon before adapting the control gain in real time [30], [31]. In addition, the tuning range of the gain is large and may vary significantly for different wind turbines. Thus, the adaptation rates of these algorithms are slow. The hill-climb searching (HCS) method is another model-free optimal point tracking technique [32]–[35]. This control law observes the performance change after applying a perturbation in control inputs. Then, the searching direction of the control input stays the same or goes in the opposite direction based on whether the observed performance is

better or worse. However, HCS requires distinguishing whether the performance change is caused by the control inputs or varying wind speed [36]. The HCS algorithm is only applicable when the detected wind speed disturbance is very small to the point that its impact can be neglected. This undermines the effectiveness of HCS because many wind turbines operate under volatile wind speed profiles. Therefore, it is desirable to develop a controller that can rapidly and robustly track the optimal operating point that leads to maximum power generation under model uncertainties.

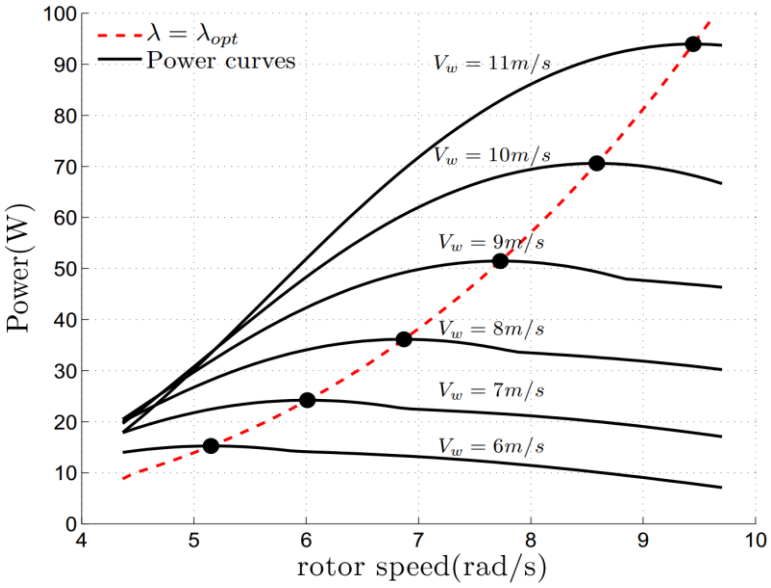

Figure 1.7: Power curves under different wind speeds and the optimal TSR curve for a 100 kW wind turbine.

1.4 Fatigue Loading Mitigation and Speed Regulation

In addition to maximizing wind energy capture, minimizing the maintenance cost of wind turbine system is also important for reducing the overall cost of wind power. As the rotor speed varies, the loads acting on the wind turbine also change. Cyclic forces or torques will introduce fatigue loadings to the turbine structure and potentially cause its

premature failure [37], [38]. The tower, blades and drivetrain of a wind turbine are three main components subjected to critical fatigue loads under fluctuating wind speeds [39].

Extensive research effort has been conducted to develop controllers for mitigating fatigue loads on turbine blades [37], [38], [40]–[43]. A disturbance accommodating controller was proposed to mitigate blade loads by rejecting a step-wise/periodic wind speed disturbance [44]. This controller applies linear quadratic optimization by linearizing the nonlinear turbine model at a specific operating point. Therefore, its performance may performance degradation may occur for other operating conditions. Linear parameter varying (LPV) techniques were used for gain scheduling under various operating conditions of a wind turbine [45]. However, the developed LPV controllers can be unstable in certain conditions. Feedforward controllers including a ZPETC and a FX-RLS were assisted with the light detection and ranging (LIDAR) technology, which can be used for measuring upcoming wind disturbance in front of the turbine [41]. The LILAR-assisted ZPETC controller mitigates the fatigue loads acting on the blades at the expense of worse tower loads and pitch rates. The LIDAR-assisted FX-RLS controller reduces blade loads without exacerbating the tower loads. But it is highly sensitive to the initial conditions. Modern large wind turbines experience asymmetric loads due to spatial variations of wind speed across the rotor plane. Individual pitch controllers are proposed to mitigate the once-per-revolution (1P) loads acting on the turbine blades [40], [43].

Most of the above controllers are designed for wind turbine operations at above-rated wind speeds because more than 95% of blade fatigue damage occurs at or above the rated wind speed [46]. During the partial load operation where wind speed is below the rated speed, cyclic variation of the rotor torque and thrust force introduce bending moments to the base of turbine tower [47] which could potentially cause significant damage when their frequencies coincide with the natural frequency of the tower.

Therefore, for partial load operation, it is necessary to develop a controller that not only maximizes wind energy capture but also minimizes fatigue loading on a turbine tower. For full load operation, the wind turbine power output remains the rated power. The turbine rotational speed is maintained at the desired value by controlling the blade pitch angle. The speed regulation is an important task for reducing the chance of over-speeding of a generator. Also, the drivetrain fatigue loads can be effectively reduced by mitigating speed oscillations around the rated value. For this purpose, an optimized blade pitch controller for speed regulation and drivetrain fatigue mitigation is desired.

1.5 POWER DISPATCH FOR INTERMITTENT WIND ENERGY

In order to accelerate the deployment of wind energy, it is necessary to remove the barrier to wind power grid integration. One of the biggest challenges to wind power grid integration is the intermittence of wind power, which makes it difficult to be dispatchable as traditional power sources. Currently, the electric grid control system dispatches power at different time scales [48]. A long-term dispatch schedule is usually planned a day ahead to determine the switch status of each power source in the grid. A short-term dispatch schedule is often made 30 minutes (30min) before the operating time to decide the amount of power output from a certain power source. Due to the intermittence of wind power generation, wind farm owners often schedule the power output conservatively so that they can avoid cost associated with using conventional spin reserves in case the wind power generation is lower than its scheduled target [49]. This will reduce the efficiency of the wind energy conversion. In order to address this issue, a battery energy storage system (BESS) can be integrated with wind turbines [49]–[51]. The BESS stores extra wind energy that cannot be absorbed by the grid and releases the stored energy in the presence of power shortage, hence resulting in higher efficiency of

the overall wind power system. It will improve the cost competitiveness of wind energy. Furthermore, a BESS will also help improve the output power quality by actively limiting the power ramp rate.

For an integrated BESS and wind power system, power output scheduling from the battery and wind turbine plays a critical role in maximizing the entire system efficiency. Recently, a heuristic algorithm is developed based on the direct feedback of BESS state of charge (SOC) [49]. Using this method, more power output is scheduled with a higher SOC and less power output is scheduled with a lower SOC so that the SOC is maintained at its mid-level. The heuristic method is simple to implement; however, it requires the BESS to have a large capacity to compensate for wind power intermittence and leads to a high system cost. In order to minimize the cost associated with battery system installation, model predictive scheduling algorithms have been developed. A dynamic programming (DP) approach is applied in [52]. In addition, a multi-pass DP is combined with particle swarm optimization to improve the solution quality of nonlinear optimal scheduling problem [53]. A standard quadratic programming (QP) algorithm is also proposed in [54] to minimize the ramp rate of scheduled power output with reduced battery size. Although the above algorithms theoretically optimize the scheduled power output, they generally require long-term multi-step-ahead predictions [55] in order to implement DP or QP. In general, the confidence intervals of predictions become wider the further we look into the future. For k-step-ahead wind power prediction, the prediction accuracy drops quickly as the value of k increases [56]. This undermines the effectiveness of these optimization approaches. Moreover, these methods incur higher computational expense as the optimization horizon is extended, and renders this type of algorithm not applicable for real time application. Therefore, it is desirable to develop an

efficient and reliable power output scheduling strategy for wind turbine systems with BESS.

In addition to determining the scheduled power output, accurately tracking the scheduled target in real-time is also important. To smooth out the variations in wind power and thus accurately track the scheduled target, a wind turbine should be actively controlled to track a reference power set point that optimizes the performance of the integrated wind turbine and BESS. In [50], control techniques are presented for an individual turbine to track a reference power set point. A pitch-based control is recommended for Region 2, also defined as the below-rated speed region, while a torque-based control is preferred for Region 3, also defined as the rated speed region. Despite its capability of set point tracking, this controller induces significantly large turbine torque variation during certain generator speed ranges. Besides, the pitch controller drives the wind turbine to operate at a lower-than-optimal tip speed ratio (TSR) during the below-rated region. With a lower tip speed ratio, thus less stored kinetic energy in turbine rotor, the wind turbine is less capable of delivering consistent power output in the presence of wind shortage. Another active power controller named as torque-speed tracking controller (TTC), is detailed in [58], [59] for power set point following. Similarly to the standard controller [60] used in the industry, the generator torque of TTC is proportional to the square of generator speed during the below-rated speed operation. The improvement is that TTC uses a new torque feedback gain to track a higher-than-optimal tip speed ratio (TSR). For Region 3 operation, the torque is directly controlled to track the reference power. Using TTC, even though capturing more wind energy, the turbine is more likely to switch between Region 2 and Region 3 when the actual wind power is oscillating around the reference power set point. This could cause significant rotor speed and torque fluctuations that lead to increased loadings on the turbine structure. Therefore,

it is necessary to develop a real-time controller that improves wind turbine performances in addition to achieving accurate power set point tracking.

1.6 Wind Turbine Participation in Grid Frequency Regulation

Grid operators are responsible for maintaining the balance between electricity generation and load [61]. Traditional thermal/hydro units are required to provide regulation in order to maintain power balance and grid frequency [62]. Generally, the grid frequency regulation can be separated into 2 stages, namely, primary control and secondary control [63]. Primary control establishes the balance between the generated and demanded power by a proportional control action: droop control. During the first 20-30 seconds, primary control stabilizes the frequency drop with possible bias compared to the nominal frequency. Subsequently, secondary control modifies the power set point for each unit in order to restore the grid frequency to its nominal value. The time scale of secondary control is typically around 5 to 10 minutes.

Most variable-speed modern wind turbine generators are decoupled from grid frequency through power electronic converters. The inertia of the generator and the turbine rotor do not participate in grid inertial response as conventional thermal/hydro generating units. Hence, the burden of frequency regulation increases as more conventional units are replaced by wind turbines, resulting in a decline of grid response to frequency deviation events. To improve the competitiveness of wind power, it is necessary for wind turbines to provide inertial response to frequency deviation events. Although wind power is historically considered as merely a cause of frequency variability, it is capable of regulating grid frequency by exploitation of the rotational energy stored in the turbine rotor. A wind turbine can emulate the inertial response of traditional synchronous generator by controlling the generator torque [64]. The power

electronics used by modern variable-speed wind turbines allow fast actuation of generator torque. Therefore, wind turbines are capable of providing faster inertial frequency regulation than traditional generators of the same inertia [62].

The interest in the potential for wind turbines to provide regulation services has motivated new opportunities in control system research and development [62]. An inertial response emulation approach for wind turbine is discussed in [65]. It adjusts the generator torque set point based on the rate of change of grid frequency. This approach is limited in real application due to the estimation of frequency derivative, which is very sensitive to the measurement noise. A similar torque-based controller proposed in [66] eliminates the need to evaluate the frequency derivative. Instead, it calculates the additional torque based on the deviation between the grid frequency and its nominal value. Because this controller fails to consider turbine aerodynamics, this method may lead to instability or shut-down of a wind turbine, which may result in impaired frequency response. A maximum-power point tracker (MPPT) is included in [67] to provide the controller with a self-stabilizing mechanism that prevents stalling or slowing down a wind turbine too much. With this controller, the capability of providing inertial response under low wind speed is limited due to low rotational energy stored in the turbine rotor. Deloaded wind turbine controllers are proposed in [68], [69] to create a controllable power reserve. Instead of maximizing power extraction, the wind turbine is controlled to operate at a reduced power level, usually 80% - 90% of the maximum power. Hence, the wind turbine is able to increase 10%-20% of its power production in case of under-frequency events. Both blade pitch angle and generator torque can be manipulated to effectively deload the power production [68]. A variable droop method for deloaded wind turbine controller is developed in [63]. The frequency support from individual wind turbine is regulated based on the available power reserve in turbine rotor, which depends on the prevailing wind

speed. By applying variable droops under varying wind speed, the frequency regulation capability is improved during low wind speed periods. In case of under-frequency events, the above deloaded wind turbine controllers first increase the captured wind power and subsequently the generated electric power. These controllers are stable by design. However, the loss of energy capture due to deloading hinders their deployments. Energy storage systems such as batteries and supercapacitors are applied to provide power reserves such that the wind turbine can generate close to the maximum energy available [70]–[75]. But it causes additional costs for the system. A robust and efficient wind turbine control strategy for supporting grid frequency is in high demand for increasing wind energy penetration.

1.7 CONTRIBUTIONS

In this dissertation, cost-conscious control designs are developed. The cost-competitiveness of a wind turbine is enhanced by maximizing energy conversion efficiency, reducing maintenance cost, improving power dispatch and enhancing capability of grid frequency regulation. To this end, control designs are focused on maximizing wind energy capture [76], [77], mitigating fatigue loading [78], [79], overcoming wind intermittence and supporting grid frequency following a power imbalance event [80], [81]. The effectiveness of the proposed controllers is demonstrated through simulations using high-fidelity wind turbine models with real wind speed profiles.

Chapter 2: *Modeling of Wind Turbine Systems*

Figure 2.1 shows a simulation model of wind turbine system. It contains 5 major parts: sensor, generator, pitch actuator, wind turbine plant and controller. The sensor measurements are modeled with bias, noise and delay. Since the electrical generator has a much faster response than the wind turbine and pitch actuator, a simple first order generator model is sufficient for the purpose of simulation:

$$\dot{T_g} + \frac{1}{\tau}(T_g - T_{g,cmd}) = 0 \tag{2.1}$$

where τ, T_g and $T_{g,cmd}$ are the generator time constant, generator torque and commanded generator torque, respectively. The generator torque and its changing rate are saturated by limits.

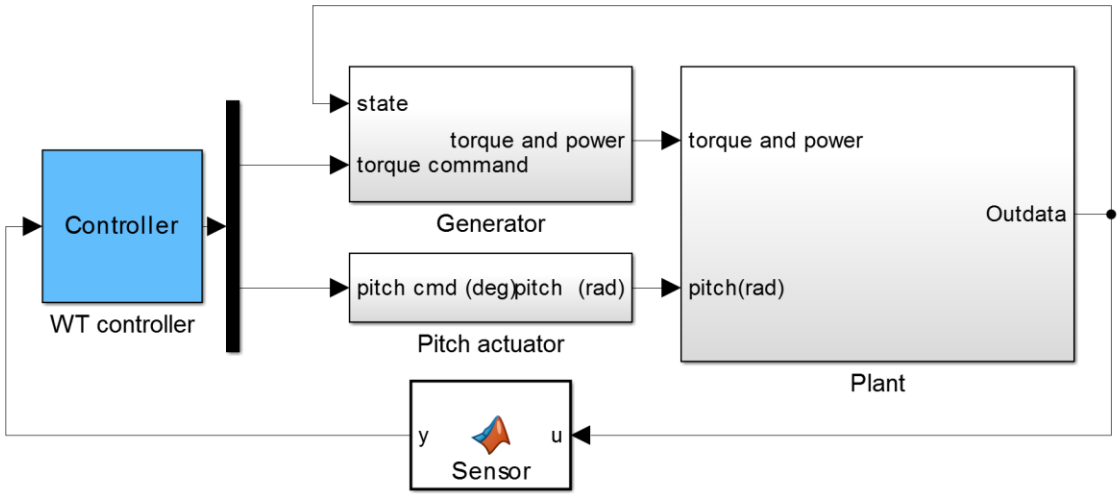

Figure 2.1: Simulation model of a wind turbine system.

A hydraulic blade pitch actuator can be modeled as a second order system:

$$\ddot{\beta} + 2\zeta\omega_n\dot{\beta} + \omega_n^2(\beta - \beta_{cmd}) = 0 \tag{2.2}$$

where ζ, ω_n, β and β_{cmd} are the pitch actuator damping ratio, pitch actuator natural frequency, pitch angle and commanded pitch angle, respectively. The pitch angle and its changing rate are saturated by limits.

2.1 WIND TURBINE MODELS

Wind turbine modeling is crucial for understanding and optimizing the operation of wind turbine systems. On one hand, a high-fidelity model is required to represent an actual wind turbine and get accurate simulation results. On the other hand, a simplified control-oriented model is preferred for controller design and analysis. In this chapter, bond graph modeling method is used to derive the dynamic equations of wind turbine with different complexities. The presented wind turbine models include a one-mass model, a two-mass model with a rigid tower, a two-mass model with a flexible tower and an aero-elastic high-fidelity model. The reduced order models are compared with the high-fidelity model to validate the model reduction.

a. One-mass Model

A wind turbine one mass model assumes rigid low-speed shaft, blades and tower. Due to a rigid low-speed shaft, rotor inertia and generator inertia are lumped together. Its bond graph is shown in Figure 2.2. The corresponding state space equation can be derived as:

$$\left(J_r + G_r^2 J_g\right)\dot{\omega} + b\omega = T_{aero} - G_r T_g \tag{2.3}$$

where J_g, T_g, ω_g, J_r, ω, G_r, b are the generator inertia, generator torque, generator speed, rotor inertia, turbine rotor speed, gear ratio and rotor frictional coefficient, respectively. The aerodynamic torque is given by:

$$T_{aero} = \frac{\pi}{8}\rho_{air} D_r^2 V_w^3 C_p/\omega \tag{2.4}$$

where ρ_{air}, D_r, V_w and C_p are the air density, rotor diameter, rotor effective wind speed and energy coefficient of a wind turbine, respectively. C_p is a nonlinear function of the tip speed ratio (TSR) and blade pitch angle. The TSR (λ) is defined as the ratio of blade tip speed to wind speed:

$$\lambda = \frac{\omega D_r}{2V_w} \tag{2.5}$$

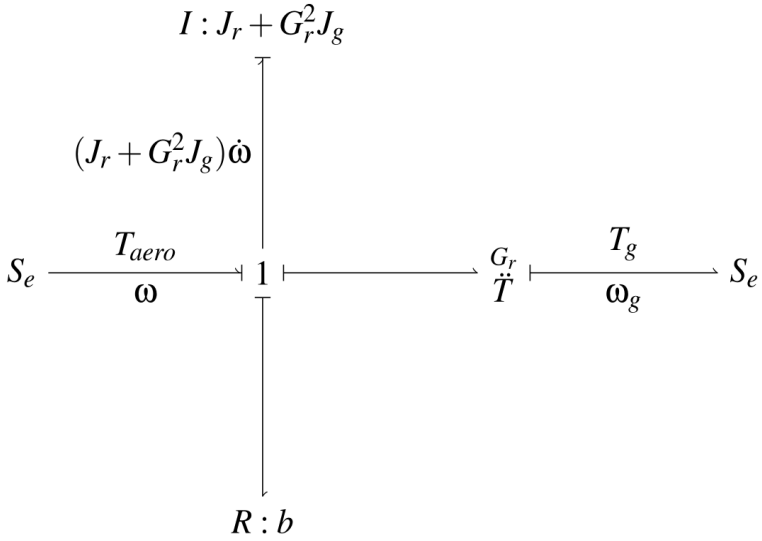

Figure 2.2: Bond graph for wind turbine one-mass model.

b. Two-mass Model with a Rigid Tower

A wind turbine two mass model with a rigid tower assumes rigid blades and tower. However, the low-speed shaft is flexible in this model. Its bond graph is shown in Figure 2.3. The corresponding state space equation is:

$$\begin{bmatrix} \dot{\omega} \\ \dot{\omega}_g \\ \dot{\varphi} \end{bmatrix} = \begin{bmatrix} -\frac{B+b}{J_r} & \frac{B}{G_r J_r} & -\frac{K}{J_r} \\ \frac{B}{G_r J_g} & -\frac{B}{G_r^2 J_g} & \frac{K}{G_r J_g} \\ 1 & -\frac{1}{G_r} & 0 \end{bmatrix} \begin{bmatrix} \omega \\ \omega_g \\ \varphi \end{bmatrix} + \begin{bmatrix} \frac{1}{J_r} & 0 \\ 0 & -\frac{1}{J_g} \\ 0 & 0 \end{bmatrix} \begin{bmatrix} T_{aero} \\ T_g \end{bmatrix} \tag{2.6}$$

where B, K and φ are low-shaft torsional damping, low-shaft torsional stiffness and low-shaft torsional deflection, respectively. The rotor torque is given by $T_r = K\varphi$. The aerodynamic torque T_{aero} is obtained as (2.4).

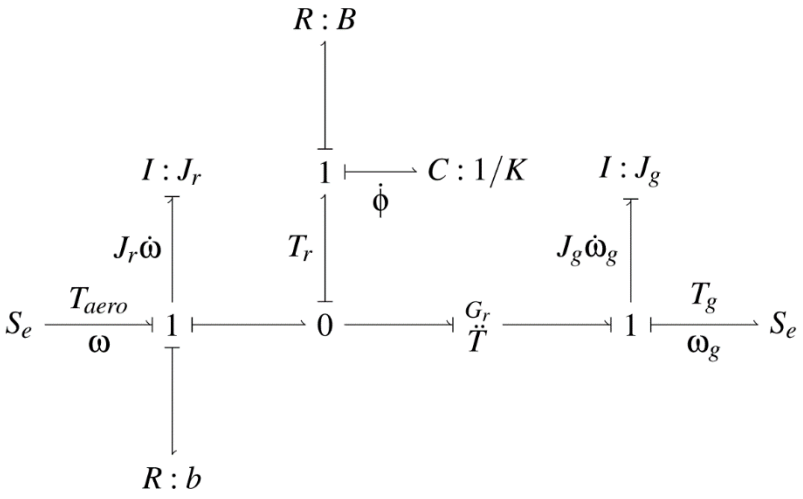

Figure 2.3: Bond graph for wind turbine two-mass model with a rigid tower.

c. Two-mass Model with a Flexible Tower

A wind turbine two mass model with a flexible tower assumes rigid blades. However, the low-speed shaft and tower are flexible in this model. The bond graph for a flexible tower is shown in Figure 2.4. The corresponding state space equation is:

$$\begin{bmatrix} \dot{x} \\ \dot{v} \end{bmatrix} = \begin{bmatrix} 0 & 1 \\ -\frac{K_{twr}}{M_{twr}} & -\frac{B_{twr}}{M_{twr}} \end{bmatrix} \begin{bmatrix} x \\ v \end{bmatrix} + \begin{bmatrix} 1 \\ \frac{1}{M_{twr}} \end{bmatrix} F_t \tag{2.7}$$

where B_{twr}, K_{twr}, M_{twr}, x and v are tower top equivalent damping, tower top equivalent stiffness, tower top equivalent mass, tower top fore-aft displacement and tower top fore-aft velocity, respectively. The rotor thrust force is given by:

$$F_t = \frac{\pi}{8}\rho_{air} D_r^2 V_w^2 C_t \tag{2.8}$$

where C_t refers to the thrust coefficient of a wind turbine. C_t is a nonlinear function of the TSR and blade pitch angle. Using this model, the wind speed across the rotor plane is modified due to tower fore-aft velocity. Hence, the aerodynamic torque for two-mass model with a flexible tower is obtained as:

$$T_{aero} = \frac{\pi}{8}\rho_{air} D_r^2 (V_w - v)^3 C_p/\omega \tag{2.9}$$

The corresponding TSR is obtained as $\frac{\omega D_r}{2(V_w - v)}$.

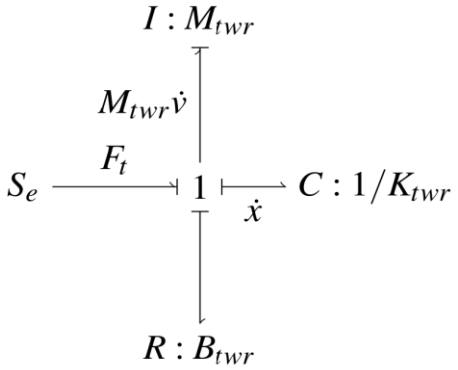

Figure 2.4: Bond graph for a flexible tower.

d. High-fidelity Aero-elastic Model

A high-fidelity aero-elastic model (FAST) is provided by National Renewable Energy Laboratory (NREL). FAST joins aerodynamics models, hydrodynamics models for offshore structures, electrical system (servo) dynamics models, and structural (elastic)

dynamics models to enable coupled nonlinear aero-hydro-servo-elastic simulation in the time domain [82]. In the FAST model, blades, tower and low-speed shaft are all flexible. The following degrees of freedom are enabled in the FAST model: drivetrain mode, generator mode, first and second tower side-to-side modes, first and second tower fore-aft modes, first and second blade flapwise modes and first blade edgewise mode. The high-fidelity model is used for simulation and validation of the reduced-order models.

2.2 BASELINE CONTROLLER

A controller developed for NREL 5 MW wind turbine [60] is widely used in the industry and hence it is selected as the baseline controller for this study. The controller requires measurements of rotor speed ω and blade pitch angle β. It applies different control laws during Region 3 and non-Region 3 operation. Specifically, a wind turbine is said to be operating in non-Region 3 when its rotor speed is below the rated value and the blade pitch angle is less than $\beta^* + 1°$, where β^* is a fixed blade pitch angle operating point where the C_p is maximized. Otherwise, the wind turbine is said to be operating in Region 3.

a. Non-Region3 Control

During non-Region 3 operation ($\omega \leq \omega_{rated}$ and $\beta \leq \beta^* + 1°$), the commanded pitch angle is fixed at β^*. As shown in Figure 2.5, the commanded generator torque is given by the following equation:

$$T_{g,cmd}(\omega) = \begin{cases} 0 & \omega \leq \omega_{cutin} \\ linear\ interp & \omega_{cutin} < \omega \leq 1.3\omega_{cutin} \\ K_{stc}\omega^2 & 1.3\ \omega_{cutin} < \omega \leq 0.99\omega_{rated} \\ linear\ interp & 0.99\omega_{rated} < \omega \leq \omega_{rated} \\ \dfrac{P_{rated}}{G_r\omega} & \omega_{rated} < \omega \end{cases} \tag{2.10}$$

Where P_{rated}, ω_{cutin}, ω_{rated} and ω are the rated power, cut-in, rated and measured turbine rotor speed, respectively. K_{stc} is the standard torque controller gain given by:

$$K_{stc} = \frac{\pi}{64 G_r} \rho_{air} {D_r}^5 \frac{C_p(\lambda^*)}{{\lambda^*}^3} \tag{2.11}$$

where λ^* denotes the reference TSR. If the modeling parameters are exactly the same as the actual plant, then the reference TSR is equal to the optimal TSR λ_{opt} and $C_p(\lambda^*) = C_{p,max}$. The generator torque controller in Region 2 is also known as Standard Torque Controller (STC).

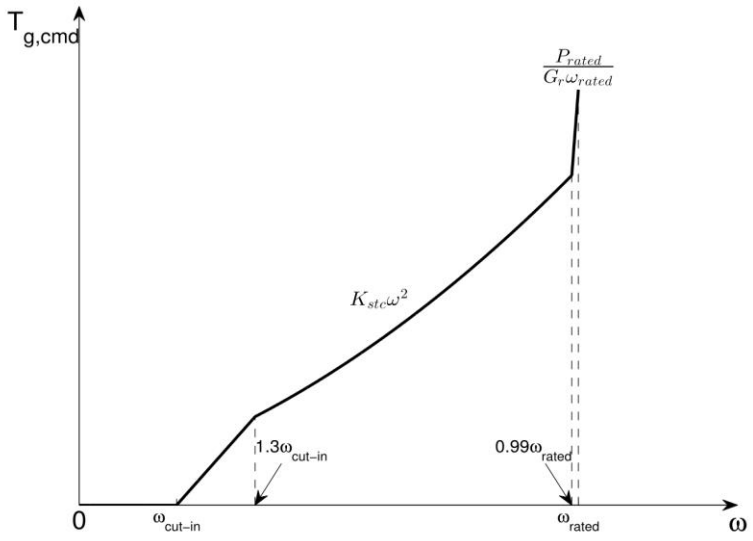

Figure 2.5: Commanded generator torque versus rotor speed for baseline controller during non-Region 3 operation.

b. Region3 Control

During Region 3 operation ($\omega > \omega_{rated}$ or $\beta > \beta^* + 1°$), the commanded generator torque is given by:

$$T_{g,cmd} = \frac{P_{rated}}{G_r \omega} \tag{2.12}$$

and the commanded pitch angle is controlled using a gained-scheduled Proportional-Integral (PI) Controller:

$$\beta_{cmd} = K_p(\beta)\Delta\omega + K_i(\beta)\int \Delta\omega dt \tag{2.13}$$

where $\Delta\omega = \omega - \omega_{rated}$. $K_p(\beta)$ and $K_i(\beta)$ are the scheduled proportional and integral gains [60], respectively.

2.3 Comparison of Different Wind Turbine Models with Baseline Controller

In this section, the established reduced order models are validated with the FAST model through simulations. Simulations are conducted using different models with the same wind profile and the same controller. Discussion of controller design will be detailed in the next chapters. Figure 2.6 compares the simulation results of the four models in Section 2.1 by applying a baseline controller [60] to NREL 5 MW wind turbine. The subplots of Figure 2.6 show the wind speed, rotor speed, generator torque, pitch angle, TSR and generator power, respectively. Figure 2.7 shows the simulation results of the two-mass model with flexible tower and FAST model by applying a baseline controller to NREL 1.5KW WindPact turbine [83]. The subplots of Figure 2.7 show the wind speed, rotor speed, pitch angle, rotor torque and rotor thrust force and tower fore-aft bending moment, respectively. The results of reduced order models are very close to that from FAST model with an error of less than 2%. Based on the simulation results, we can conclude that the reduced order models can simplify the dynamics of the high-fidelity model with little sacrifice of accuracy. Therefore, the reduced order models can serve the purpose of control designs.

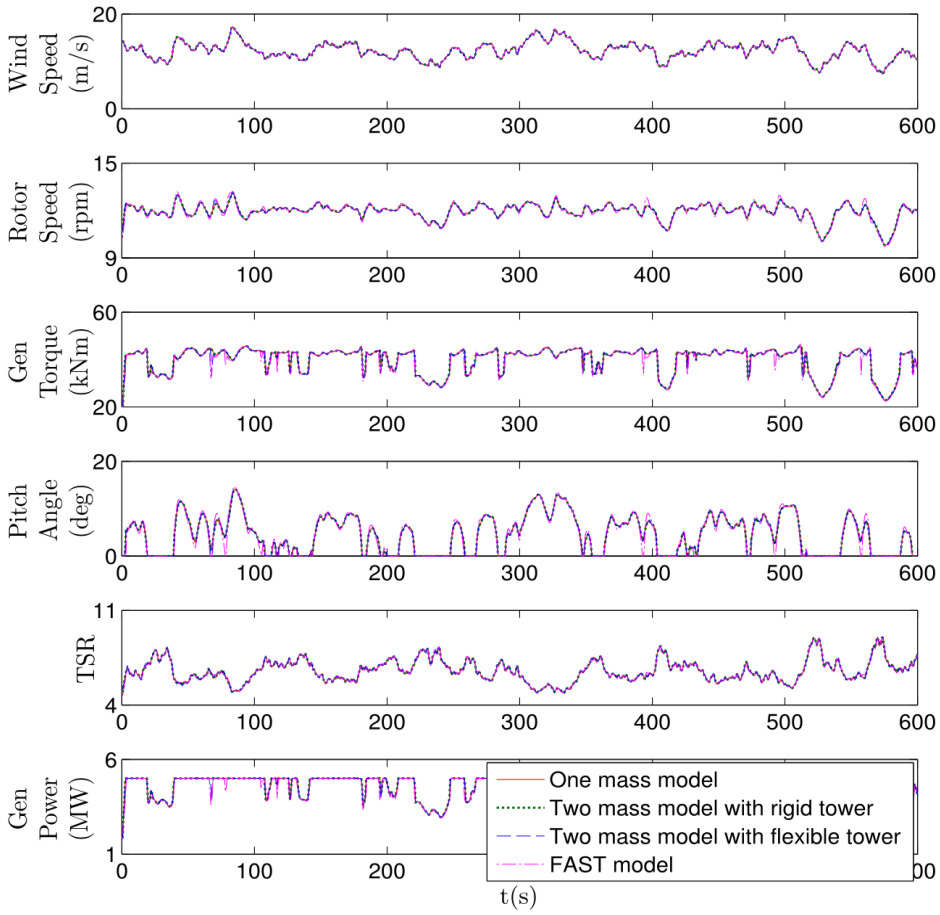

Figure 2.6: Comparisons of different wind turbine models on the NREL 5 MW wind turbine with baseline controller under varying wind inflow.

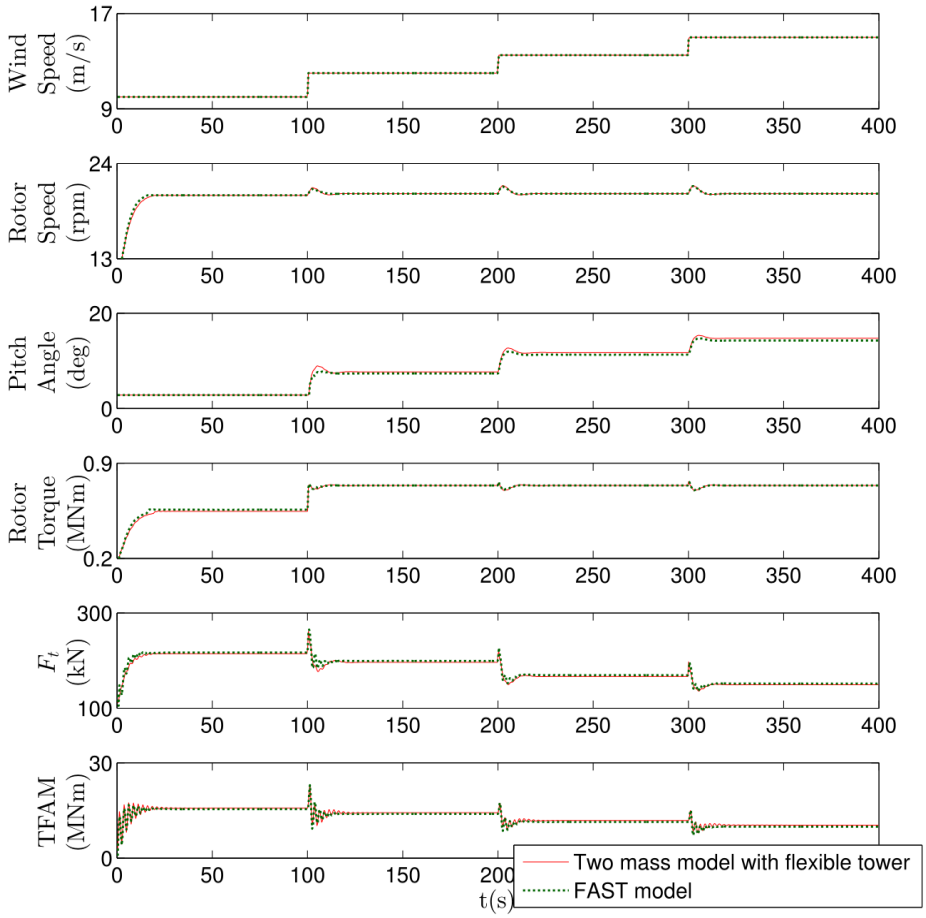

Figure 2.7: Comparisons of different wind turbine models on the NREL 1.5 MW WindPact turbine with baseline controller under stepwise wind inflow.

Chapter 3: *Control Designs for Maximizing Wind Energy Capture*

The main control objective during wind turbine partial load operation is to maximize wind energy capture. In this chapter, control algorithms are explored to maximize wind energy capture under volatile wind profiles. First, dynamic programming (DP) is applied to find the optimal control input for the theoretical maximum energy that can be captured over a given time horizon. Since DP relies on exhausted search for optimal solutions, its high computational intensity limits its application to off-line optimization. In order to address this issue, a DP-based real-time controller (DPRC) is developed to fast track the optimal performance. However, DPRC performance deteriorates in the presence of modeling error. A gain modified optimal torque controller (GMOTC) is then proposed to achieve both maximum wind energy capture and good robustness against model uncertainties. Light detection and ranging (LIDAR) technology is utilized to further improve the controller performance. Simulation results are presented to demonstrate the effectiveness of the proposed methods on maximizing wind energy capture and robustness against modeling uncertainties, such as the model-plant mismatch. Preventing turbine structural damage is another important aspect of wind turbine operation. Even though these controllers are not developed specifically for fatigue loading mitigation, their impact on generator torque is also compared to examine whether they will adversely affect the turbine fatigue loading.

Some portions of this chapter have appeared previously in the following publications:

1. Z. Ma, Z. Yan, M. L. Shaltout, and D. Chen, "Optimal Real-Time Control of Wind Turbine During Partial Load Operation," Control Syst. Technol. IEEE Trans. On, vol. 23, no. 6, pp. 2216–2226, 2015. (The author of this dissertation contributed to algorithm development, simulation and analysis)
2. Z. Ma, M. L. Shaltout, and D. Chen, "Adaptive Gain Modified Optimal Torque Controller for Wind Turbine Partial Load Operation," p. V002T18A002, Oct. 2014. (The author of this dissertation contributed to algorithm development, simulation and analysis)

Section 3.1 presents a 100 kW wind turbine model. An off-line DP optimization is presented in Section 3.2, which provides a benchmark for real-time controller design. The control design for DPRC and GMOTC are discussed in Section 3.3 and 3.4, respectively. Section 3.5 discusses LIDAR augmented control with previewed wind speed measurements. A number of simulations are conducted in Section 3.6 to compare the performances of different controllers. A summary is finally presented in Section 3.7.

3.1 WIND TURBINE MODELING PARAMETERS

Prior to introducing the control design, modeling parameters of a 100kW wind turbine is described in this section. The model will be used to demonstrate the developed control methodologies. The wind turbine model is detailed in [84]–[86]. The system parameters of this wind turbine are shown in Table 3.1. A control-oriented one-mass wind turbine model in (2.3) is rearranged as:

$$J_d\dot{\omega} = \frac{\pi}{64}\rho_{air}{D_r}^5\frac{C_p(\beta,\lambda)}{\lambda^3}\omega^2 - b\omega - G_rT_g \tag{3.1}$$

where $J_d = J_r + G_r^2J_g$ refers to the equivalent drivetrain inertia. The power coefficient C_p of this wind turbine is a nonlinear function of blade pitch angle β, and tip speed ratio λ, defined by [87]:

$$\begin{cases}\dfrac{1}{\lambda_i} = \dfrac{1}{\lambda + 0.08\beta} - \dfrac{0.035}{1+\beta^3} \\ C_p(\beta,\lambda) = 0.5(\dfrac{116}{\lambda_i} - 0.4\beta - 5)e^{-\frac{21}{\lambda_i}}\end{cases} \tag{3.2}$$

Figure 3.1 shows the power coefficient curve for the 100 kW wind turbine. The red thicker line on the surface indicates the local optimal pitch angle with respect to each TSR, which is defined as the function $\beta^{opt}(\lambda)$. The pentagram indicates the optimal

operating point. The blade pitch angle and generator torque are controlled simultaneously based on the measurements of rotor speed and wind speed. The control objective is to robustly converge to the optimal operating point under varying wind speed.

Parameter	magnitude
Rated power	$100\ kW$
Rotor diameter	$18.52\ m$
Drivetrain inertia	$2.6\times10^4 kg\cdot m^2$
Gear ratio	21.5858
Optimal tip speed ratio	7.9514
Optimal pitch angle	0°
Maximum power coefficient	0.4109
Cut-in wind speed	$4\ m/s$
Cut-out wind speed	$20\ m/s$
Rated wind speed	$11.25\ m/s$

Table 3.1: Modeling parameters of a 100kW wind turbine.

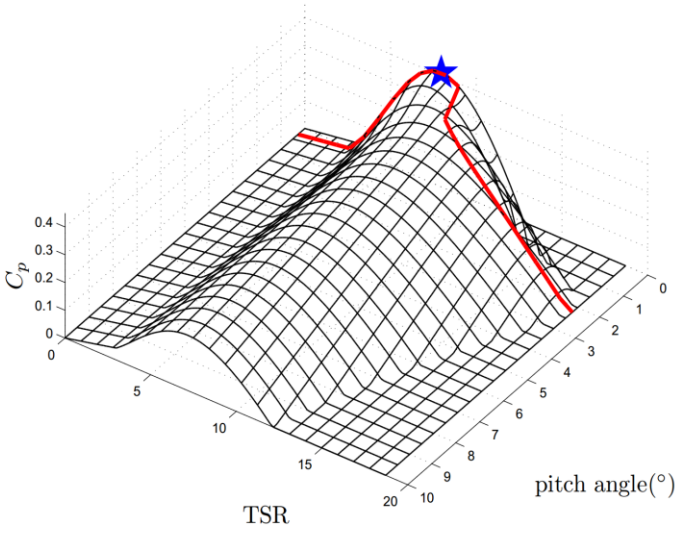

Figure 3.1: Power coefficient curve and local optimal pitch angle.

3.2 OFF-LINE ENERGY OPTIMIZATION USING DYNAMIC PROGRAMMING

Dynamic programming (DP) is first applied to search for the theoretical maximum energy capture over a given time horizon. The DP algorithm searches for the global optimal path by working backwards and performs optimization based on discretized system dynamics. Then, the result of DP is used as a benchmark to determine how well a real-time controller is designed and quantify the potential performance improvements. Let the length of each time step be h (0.5s) and the optimization time horizon be $[0, T]$. So, there are $N = T/(h + 1)$ nodes over the given time horizon. The rotor speed is chosen as the state variable. The pitch angle and generator torque are considered as control inputs. The cost function for the optimization problem is then defined as

$$E_0 = \frac{\gamma J_r}{2}[\omega_N^2 - \omega_0^2] + G_r \sum_{k=0}^{N-1} (\int_{t_k}^{t_{k+1}} T_{g,k}\omega dt), \tag{3.3}$$

where k denotes the k^{th} time step and E_0 denotes the total energy capture. The first and second terms in (3.3) refer to the increased kinetic energy and generated electrical energy, respectively. γ is an effective coefficient indicating the relative importance of kinetic energy with respect to the electrical energy generation. In this study, γ is selected to be 0.95 because the turbine frictional loss for the selected wind turbine is relatively small and most of the kinetic energy could be converted into electrical energy at the end. DP optimization starts from the end of the given time horizon with $E_N^*(\omega_N) = \gamma J_d[\omega_N^2 - \omega_0^2]/2$ and works backwards according to:

$$E_k^*(\omega_k) = max(E_{k+1}^*(\omega_{k+1}) + G_r \int_{t_k}^{t_{k+1}} \tau_k \omega dt), \tag{3.4}$$

where E_k denotes the cumulative energy capture from the k^{th} time step to the end of the given time horizon. Also, $T_{g,k}$ can be determined solely for every possible pair of $[\omega_k, \omega_{k+1}]$ by maximizing generator power within each time step. Specifically, it is assumed that the rotor speed changes linearly and the wind speed is constant within each time step $[t_k, t_{k+1}]$. So, the rotor speed and TSR are of the form:

$$\begin{cases} \omega = \omega_k + \dfrac{(t - t_k)(\omega_{k+1} - \omega_k)}{h} \\ \lambda = \dfrac{\omega D_r}{2V_w} \end{cases}. \tag{3.5}$$

By combining the discretized (3.1) with (3.5), the generator torque can be derived as:

$$T_{g,k} = \frac{1}{G_r}\left[\frac{\pi \rho_{air} {D_r}^5 C_p(\beta_k, \lambda)}{64\lambda^3}\omega^2 - b\omega - \frac{J_r(\omega_{k+1} - \omega_k)}{h}\right], \tag{3.6}$$

where β_k refers to the pitch angle at the k^{th} time step. Since $\beta_{opt}(\lambda)$ is the local optimal pitch angle, the following inequality always holds:

$$C_p(\beta_k, \lambda) \leq C_p(\beta_{opt}(\lambda), \lambda). \tag{3.7}$$

The rated power of the turbine generator is considered as an upper limit for the power generation. Therefore, the generator torque is upper-bounded by:

$$T_{g,k} \leq \frac{P_{rated}}{G_r \omega}. \tag{3.8}$$

Combining (3.5) - (3.8), the optimal generator torque can be derived as:

$$\begin{cases} T_{g,k} = \min(U_1, U_2) \quad with \\ U_1 = \dfrac{1}{G_r}\left(\dfrac{\pi \rho_{air} {D_r}^5 C_p\left(\beta_{opt}(\lambda), \lambda\right)}{64\lambda^3}\omega^2 - b\omega - \dfrac{J_d(\omega_{k+1} - \omega_k)}{h}\right) \\ U_2 = \dfrac{P_{rated}}{G_r \omega} \end{cases}. \tag{3.9}$$

β_k is then obtained by solving (3.6). The result of DP optimization will serve as a benchmark for subsequent real-time control designs.

3.3 DP-BASED REAL-TIME CONTROLLER DESIGN

Even though the DP algorithm provides the global optimal control for a given time horizon, its high computational expense renders it to be applicable only for off-line optimization. In order to benefit from DP in real-time control, a DP-based real-time controller (DPRC) is proposed in this section. This controller consists of two look-up tables resulting from an off-line DP analysis. The two tables are then used for on-line control of the blade pitch angle and generator torque based on the measurements of wind speed and rotor speed. The rotor speed can be readily measured. The wind speed can be obtained by using Light Detection and Ranging (LIDAR) technology, which was developed to predict the wind inflow with a relatively good accuracy [88].

To construct the two look-up tables, DP is applied to a time period $[0, T]$ with the assumption that the wind speed is constant during this period. T is selected to be 10s according to the capability of LIDAR technology [88]. Then, the optimal trajectories of the state and control inputs are obtained for every possible measurement of wind speed and rotor speed. Only the control input that indicates the optimal state changing direction at the first time step during $[0, T]$ is recorded. Based on this knowledge, two look-up tables are generated as shown in Figure 3.2 and Figure 3.3. The inputs to these two tables are the rotor speed and wind speed. The outputs are the blade pitch angle and generator torque. Since these two tables are obtained from off-line analysis, DPRC avoids the computational cost associated with DP and can be used for real-time control.

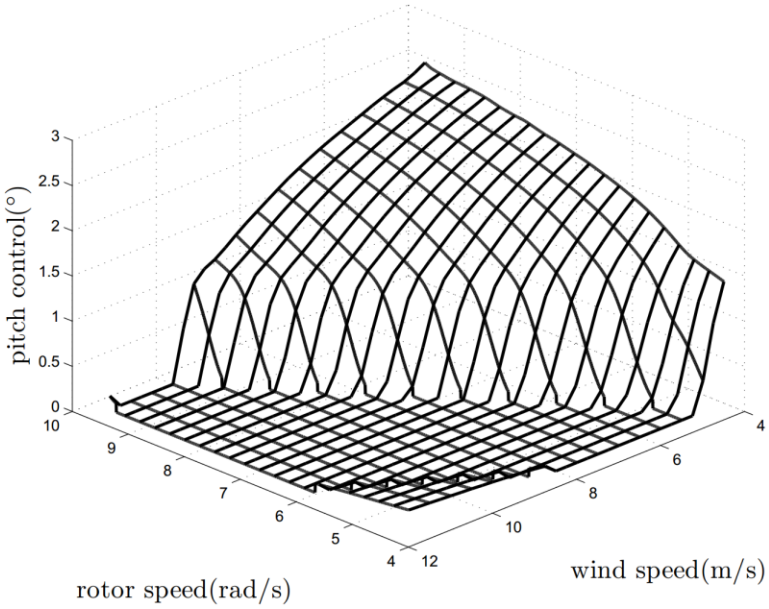

Figure 3.2: Blade pitch angle look-up table based on wind speed and rotor speed measurements for the DPRC controller

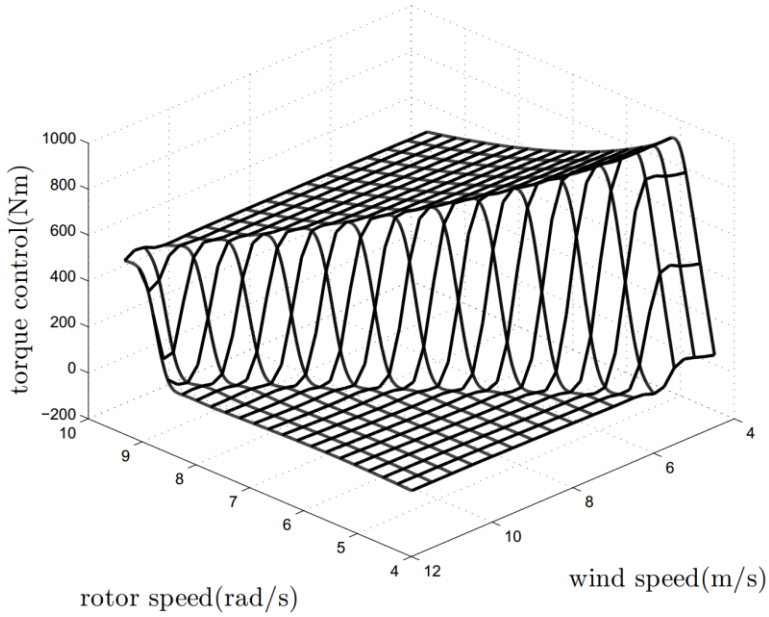

Figure 3.3: Generator torque look-up table based on wind speed and rotor speed measurements for the DPRC controller

Although the proposed DPRC can be highly efficient in wind energy harvesting, Figure 3.3 reveals that the generator torque is very sensitive to wind speed change, which may cause significant fatigue loading and structural damage to the wind turbine. Considering the trade-off between the energy capture and torque variance, the DP cost function is modified as

$$E_0 = \frac{\gamma J_d}{2}[\omega_N^2 - \omega_0^2] + \sum_{k=0}^{N-1}(G_r \int_{t_k}^{t_{k+1}} T_{g,k}\omega dt - c\Delta T_{g,k}^2), \tag{3.10}$$

where c is a coefficient that penalizes torque variance relative to energy capture. Figure 3.4 shows the modified torque control look-up table when c equals 0.0006. This modification flattens the torque control surface and therefore reduces the torque variance. As a result, the fatigue loading is mitigated. It is worth mentioning that the modification of the cost function negligibly affects the pitch angle look-up table.

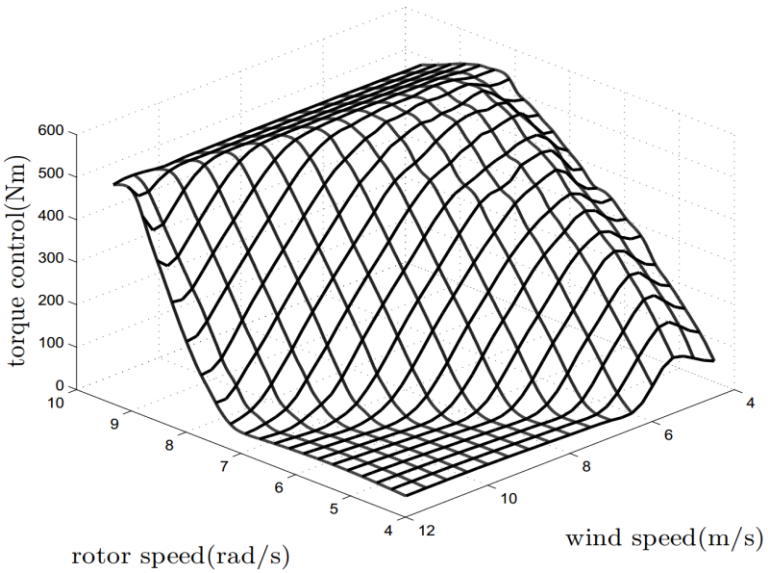

Figure 3.4: Modified generator torque control look-up table for the DPRC controller with $c = 0.0006$.

Figure 3.5 shows the step responses of DPRC controllers with different values of c as compared to the step response of the Standard Torque Controller (STC). It indicates that the controller with a smaller c has a faster step response and therefore tracks the optimal TSR better. However, the torque variance becomes larger at the same time. Depending on the system requirement, a trade-off can be achieved between wind energy capture and allowed torque variance.

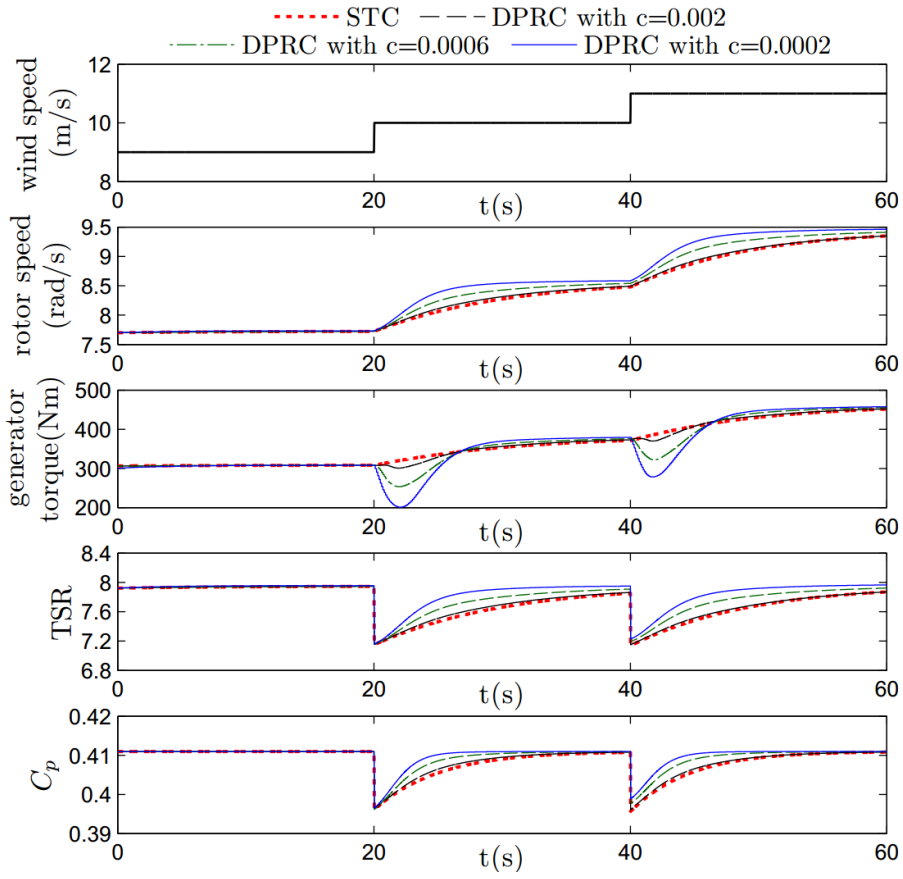

Figure 3.5: Step response analysis of the STC and the DPRC controllers with different values of c.

The above analysis is conducted without considering model-plant mismatch. In real world operation, model uncertainties and estimation error would influence the controller performances. Since the control look-up tables of DPRC are derived using a simplified turbine model, the model-plant mismatch may undermine the optimality of this approach. For instance, the modeled power coefficient values may deviate from actual values of the plant due to aero-elastic response of the turbine blades or the stochastic non-uniform wind inflow [29]. To demonstrate the impact of power coefficient estimation error on the controller performance, a deviated power coefficient curve is considered and it takes the following formula:

$$\begin{cases} \dfrac{1}{\lambda_i} = \dfrac{1}{\lambda + 0.08\beta} - \dfrac{0.057}{1+\beta^3} \\ C_p(\beta,\lambda) = 0.57\left(\dfrac{116}{\lambda_i} - 0.4\beta - 5\right)e^{-\frac{21}{\lambda_i}} \end{cases} \tag{3.11}$$

Figure 3.6 shows the actual power coefficient curve and the estimated power coefficient curve that deviates from the actual one because of unpredicted errors. Due to this deviation, the obtained control look-up tables of DPRC may lose their optimality. In this study, the aforementioned deviation in the power coefficient curve leads to a 15% parameter estimation error for both the optimal TSR and the corresponding power coefficient values. Since the gain of STC is inversely proportional to the cubic of the optimal TSR and proportional to the power coefficient at this point, the resulting feedback gain of STC has an 87% deviation from the optimal value ($K = 1.87K_{opt}$). Hence, the estimation error in power coefficient curve has a considerable influence on both STC and DPRC. Figure 3.7 provides a step response analysis of STC and DPRC considering the aforementioned model-plant mismatch. As shown in Figure 3.7, both controllers fail to track the optimal TSR when the power coefficient curve deviates from

its actual value. The estimation error of power coefficient has a smaller impact on DPRC than on STC in terms of tracking optimal TSR and maximizing power coefficient. It should be noted that even though the optimality of DPRC is lost due to the model-plant mismatch, the resulting control look-up tables still provide insights on the maximum wind energy that can be captured. This information can be used as a baseline to evaluate other optimal control strategies.

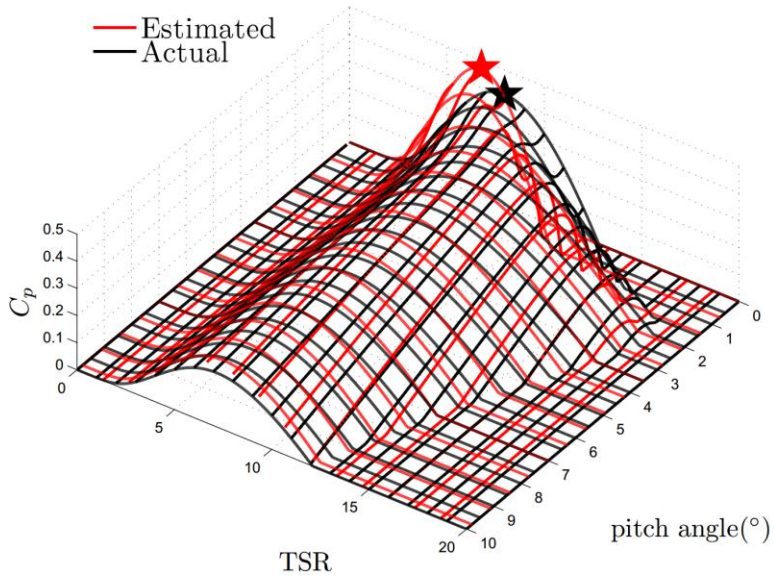

Figure 3.6: Comparison of actual power coefficient curve and estimated power coefficient curve.

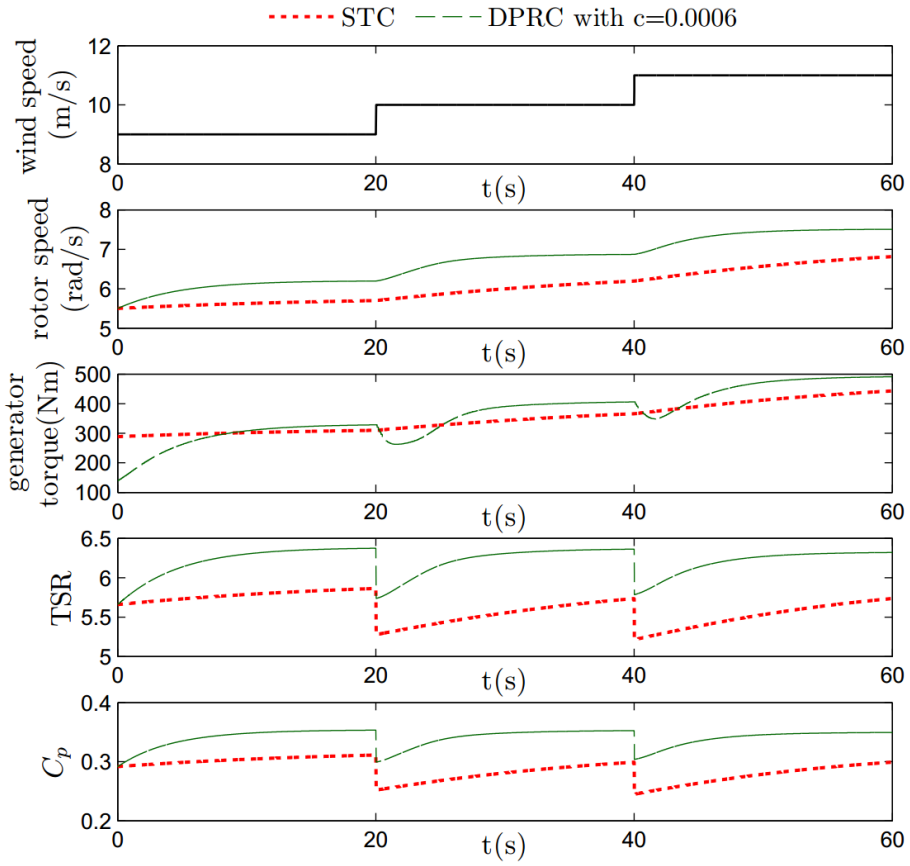

Figure 3.7: Step response analysis of the STC and DPRC controller with model-plant mismatch.

3.4 GAIN MODIFIED OPTIMAL TORQUE CONTROL

In order to improve the controller robustness against model uncertainties, a gain modified optimal torque controller (GMOTC) is proposed as an alternative to the DPRC. This controller aims to improve the tracking performance of the optimal TSR in the presence of model-plant mismatch. Unlike the STC with a fixed feedback control gain that is obtained from an ideal turbine model, the feedback control gain of the GMOTC is adapted in real-time. Difference between the measured TSR and its reference value is used to modify the feedback gain. An adaptive algorithm is then applied to search for the

optimal reference TSR in real time. As a result, the GMOTC achieves robustness against model uncertainties, while the STC fails to do so. The proposed GMOTC control law, defined as the internal PI control, is as follows:

$$\begin{cases} T_{g,cmd} = [K_1 + K_2(\lambda - \lambda^*) + K_3 \int (\lambda - \lambda^*) dt]\omega^2 \\ \beta_{cmd} = K_p(\beta^*(\lambda) - \beta) + K_i \int (\beta^*(\lambda) - \beta) dt \end{cases}. \tag{3.12}$$

where $K_1 = \frac{\pi}{64 G_r} \rho_{air} {D_r}^5 \frac{C_p(\beta^*(\lambda^*), \lambda^*)}{{\lambda^*}^3}$, λ^* denotes the reference TSR, and $\beta^*(\lambda^*)$ denotes the reference pitch angle as a function of TSR. $K_p$and K_i are the proportional and integral gains of pitch control, respectively. K_2 and K_3 are the internal proportional and integral gains of generator torque control. Their selection will be specified in the following sections.

a. Convergence to the Reference TSR

The wind turbine system is nonlinear as described by (3.1) - (3.2). The convergence to its equilibrium state is not guaranteed when applying the feedback control law expressed by (3.12). The controller's convergence to the reference TSR will be first discussed in this section. Combining (3.1) and (3.12), the system dynamics are obtained as:

$$\begin{cases} J_d \dot{\omega} + b\omega = M\omega^2 \quad with \\ M = \frac{\pi \rho_{air} {D_r}^5}{64} \left(\frac{C_p(\beta, \lambda)}{\lambda^3} - \frac{C_p^*}{{\lambda^*}^3} \right) - G_r K_2 (\lambda - \lambda^*) \end{cases}. \tag{3.13}$$

where C_p^* refers to $C_p(\beta^*(\lambda^*), \lambda^*)$. Substituting ω with $2\lambda V_w / D_r$, (3.13) can be rewritten as:

$$\dot{\lambda} = \frac{2V_w}{J_d D_r} M\lambda^2 - \frac{b}{J_d}\lambda. \tag{3.14}$$

Since the value of b/J_d is small and can be neglected in this analysis, the system can then be expressed as:

$$f = \begin{bmatrix} \dot{\lambda} \\ \dot{\beta} \end{bmatrix} = \begin{bmatrix} \frac{2V_w}{J_r D_r} M\lambda^2 \\ K_p(\beta^*(\lambda) - \beta) \end{bmatrix}. \tag{3.15}$$

Figure 3.8 shows the power coefficient for different TSR and the corresponding cubic function of TSR. As shown in this figure, when $\lambda < \lambda^*$, the solid line is higher than the dashed line which indicates $C_p(\beta^*(\lambda), \lambda) > \frac{C_p^*}{\lambda^{*3}}\lambda^3$. When $\lambda > \lambda^*$, the solid line is lower than the dash line which indicates $C_p(\beta^*(\lambda), \lambda) < \frac{C_p^*}{\lambda^{*3}}\lambda^3$. Therefore, the following inequality always holds:

$$\left(\frac{C_p(\beta^*(\lambda), \lambda)}{\lambda^3} - \frac{C_p^*}{\lambda^{*3}}\right)(\lambda - \lambda^*) < 0 \quad \forall \lambda \neq \lambda^*. \tag{3.16}$$

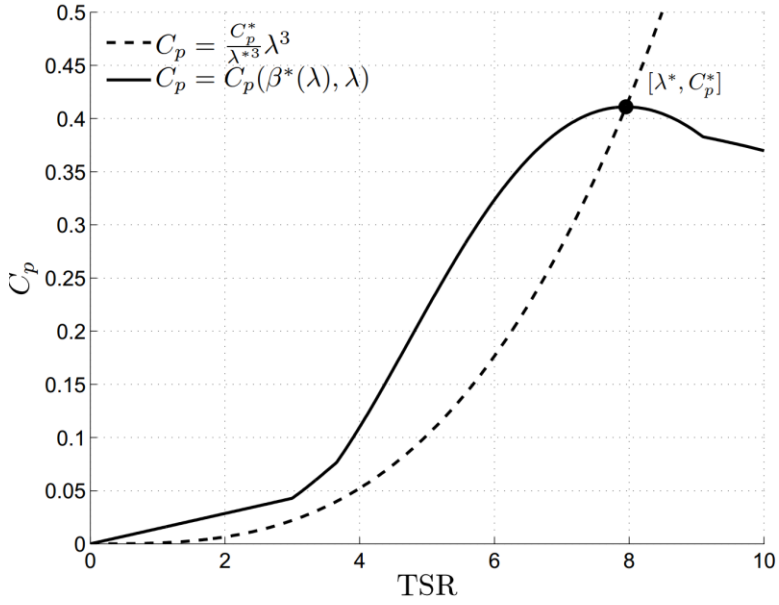

Figure 3.8: Power coefficient curve with respect to TSR and the corresponding cubic function of TSR.

The equilibrium points of the system can be obtained at $f = 0$. So, both $\lambda = 0$ and $\lambda = \lambda^*$ meet the equilibrium requirement. However, $\lambda = 0$ indicates that the turbine is stationary. So, we only focus on the other equilibrium point $[\beta^*(\lambda^*),\ \lambda^*]$.

b. Performance Tuning

After proving the system's convergence to the reference TSR, tuning of the controller gains K_2 and K_3 in (3.12) are discussed here. First, the impact of the proportional control gain K_2 on the system performance is illustrated as follows. The Jacobian matrix of the system is given by:

$$J(\beta,\lambda) = \begin{bmatrix} \frac{2V_w\lambda^2}{J_d D_r}\left[\frac{\partial M}{\partial \lambda} + \frac{2M}{\lambda}\right] & \frac{2V_w\lambda^2}{J_d D_r}\frac{\partial M}{\partial \beta} \\ K_p \frac{d\beta^*(\lambda)}{d\lambda} & -K_p \end{bmatrix}. \tag{3.17}$$

Note that we have $d\beta^*(\lambda)/d\lambda = M = 0$ at the equilibrium point. Thus, the Jacobian matrix around the equilibrium point can be derived as:

$$\begin{cases} J^* = \begin{bmatrix} -K & \frac{2V_w\lambda^2}{J_d D_r}\frac{\partial M}{\partial \beta} \\ 0 & -K_p \end{bmatrix} \quad with \\ K = \frac{2V_w{\lambda^*}^2}{J_d D_r}\left[\frac{\pi\rho_{air}{D_r}^5}{64{\lambda^*}^3}\left(\frac{3{C_p}^*}{\lambda^*} - \left.\frac{\partial C_p}{\partial \lambda}\right|_{C_p = C_p^*}\right) + G_r K_2\right] \end{cases}. \tag{3.18}$$

The eigenvalues of J^* are $-K$ and $-K_p$. By exploiting the properties of the point-wise eigenvalues, we can apply an extension of the pole-placement approach developed for linear systems. Since K_p is much larger than K, the system dynamics is dominated by the magnitude of K and can be tuned through varying the controller parameter K_2. The integral gain K_3 is used to compensate for steady state error. Based on the required system performance, K_2 and K_3 can be selected to achieve the desired system dynamic

behavior. An example of system performance with $K_2 = 2$ and $K_3 = 0.2$ is shown in Figure 3.9. Compared to STC, GMOTC shows a faster response and therefore better tracking of reference TSR. As a result, the achieved power coefficient and the captured energy are increased. However, the disadvantage of GMOTC is that the torque variations increase. A trade-off analysis between tracking reference TSR and reducing torque variations is necessary when implementing GMOTC.

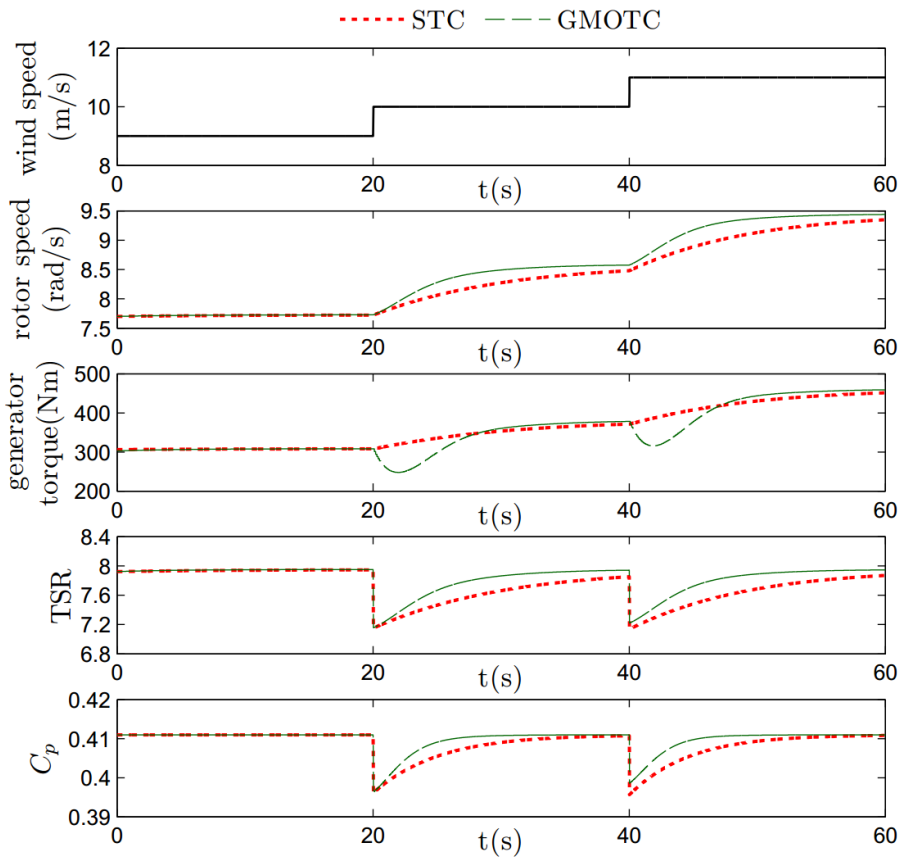

Figure 3.9: Step response analysis of the GMOTC and STC controllers.

c. Adaptive Approach

The above internal PI controller enables a fast convergence to the reference TSR, λ^*. However, λ^* is estimated based on an ideal wind turbine model, and may deviate from the actual optimal value due to modeling errors as shown in Figure 3.6. In order to improve the robustness against model uncertainties, it is necessary to adapt λ^* to its optimal value in real-time. Many optimization methods including HCS, adaptive gain scheduling etc. have been developed to search for the optimal operating point [29]–[31]. However, as mentioned in the introduction, most of them take a long time to converge and are not effective when the wind speed is volatile. In this section, a new adaptive method is introduced. This new algorithm examines whether λ has converged to its reference value over a certain time horizon, T, based on the following condition:

$$|\lambda_{avg} - \lambda^*| < \delta, \tag{3.19}$$

where λ_{avg} refers to the average TSR in T and δ is a small positive constant to test the convergence of λ. If the condition is not met, the algorithm proceeds without updating λ^*. Otherwise, the adaptive method is applied as follows:

$$\begin{cases} \lambda^*(k+1) = \lambda^*(k) + \Delta\lambda^*(k) \\ \Delta\lambda^*(k) = s * sign\big(\Delta C_{p,avg}\big) sign\big(\Delta\lambda^*(k-1)\big) \\ s = \alpha\big|\Delta C_{p,avg}\big| \\ \Delta C_{p,avg} = C_{p,avg}(k) - C_{p,avg}(k-1) \end{cases}, \tag{3.20}$$

where α is an influence factor of the step size s. A lower-bound on the step size s_{min} is selected in order to prevent slow adaptation rate. An upper-bound s_{max} is also defined so that the wind turbine would not be significantly influenced by a sudden disturbance or a measurement error. $C_{p,avg}$ refers to the average power coefficient in T. By neglecting the rotor damping in (3.1), we have:

$$C_{p,avg} = \frac{0.5J_d(\omega_f^2 - \omega_0^2) + G_r \int_{t_0}^{t_f} (T_g \omega)\, dt}{\frac{\pi \rho_{air} D_r^2}{8} \int_{t_0}^{t_f} V_w^3\, dt}, \tag{3.21}$$

where t_0 and t_f denote the start and end time of period T. ω_0 and ω_f are the rotor speed at t_0 and t_f, respectively.

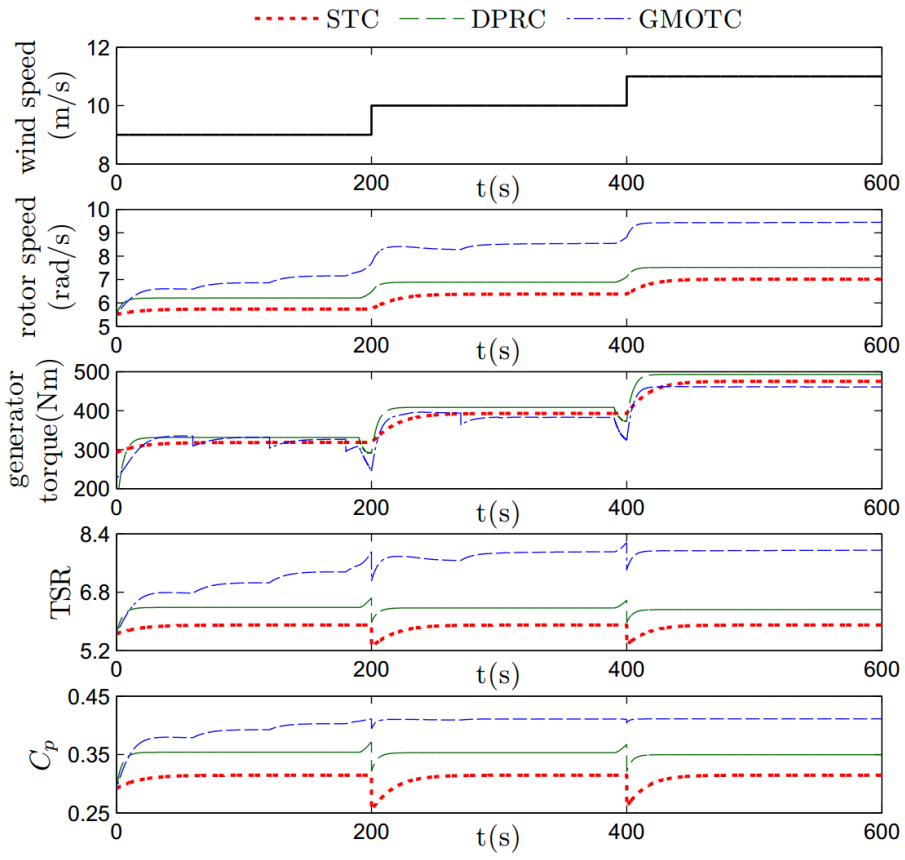

Figure 3.10: Step response analysis of the STC, DPRC and GMOTC controllers with model-plant mismatch.

An example of the adaptive control with $T = 30\ s$, $\alpha = 50$, $s_{min} = 0.01$, and $s_{max} = 0.3$ is used to illustrate the methodology. The power coefficient estimation error

as shown in Figure 3.6 is considered here. The closed-loop system step responses of the STC, DPRC, and GMOTC controllers are compared in Figure 3.10. Among the three controllers, STC and DPRC fail to track the optimal TSR because the look-up tables for DPRC and feedback control gain for STC are derived based on an inaccurate turbine model. The proposed GMOTC, on the other hand, converges to the optimal TSR with the adaptive searching algorithm. The result indicates that combining the internal PI technique with the adaptive approach enables the wind turbine to achieve its optimal operation in the presence of model-plant mismatch.

3.5 LIDAR AUGMENTED CONTROL

An accurate measurement of wind speed is important for the proposed controller. A better performance can be obtained by using the average previewed wind speed of few seconds ahead instead of the instantaneous wind speed measurement. Fortunately, such previewed wind measurement is now available due to the recent advancement in LIDAR technology. LIDAR augmented control has been discussed in details in [19], [24], [26], [41], [47], [88] and proved to be useful in improving energy capture in partial load operation. The preview time of LIDAR system is related to the focal distance and the wind speed. In this section, the focal distance of LIDAR is chosen to be 80 m and the average wind speed is 8 m/s. So, the preview time is set to be 10 s ahead of the measurement taken from the wind turbine hub. A typical wind profile downloaded from National Renewable Energy Laboratory (NREL) is used to compare LIDAR with other techniques of wind speed estimation. The result is shown in Figure 3.11, where the blue solid line refers to LIDAR measurement and the red dashed line represents the instantaneous measurement with a standard Kalman filter for averaging effect. It can be

seen that LIDAR provides a previewed wind speed that is 10 s ahead of the instantaneous method.

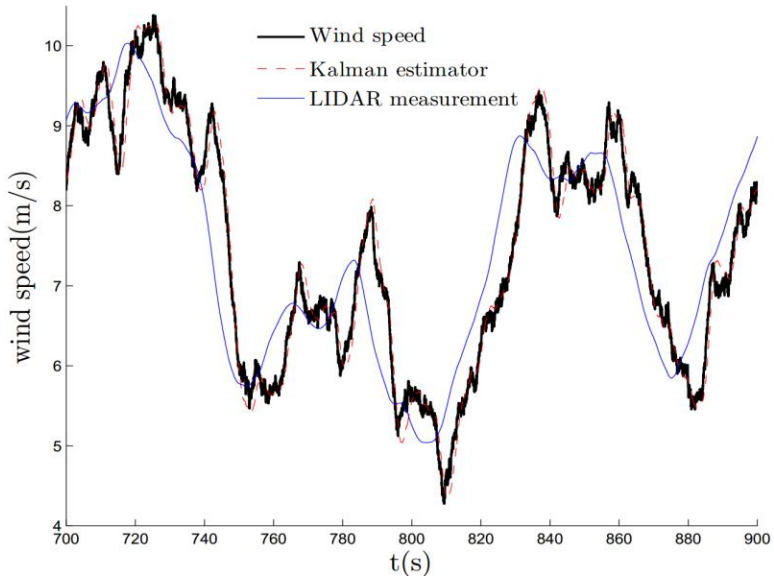

Figure 3.11: Zoom-in plot of the wind profile from 700s to 900s and the corresponding measurements from traditional Kalman estimator and LIDAR.

3.6 SIMULATION RESULTS

Simulations are conducted in MATLAB-Simulink environment to demonstrate the effectiveness of the proposed controllers. Even though the controllers are developed based on simple one-mass model, a high-fidelity model is adopted for simulation purpose. We will demonstrate the effectiveness of the proposed controller not only on the one-mass model but also on the high-fidelity model, which is more representative of the turbine dynamics. A 20 minutes wind profile generated from NREL Turbsim [89] is used for simulation. The maximum changing rates of pitch angle and generator torque are set to be 4 deg/s and 200 Nm/s. Also, the pitch angle and generator torque are limited within the range of [0, 20] degrees and 800 Nm, respectively. The pitch actuator model is

selected to have the form of a first order low pass filter with a corner frequency of 20 rad/s as used in [86]. Both cases of with and without model-plant mismatch are evaluated. The performances of STC, DPRC, LIDAR-augmented DPRC (LIDAR+DPRC), GMOTC and LIDAR-augmented GMOTC (LIDAR+GMOT) are compared to that of the off-line DP.

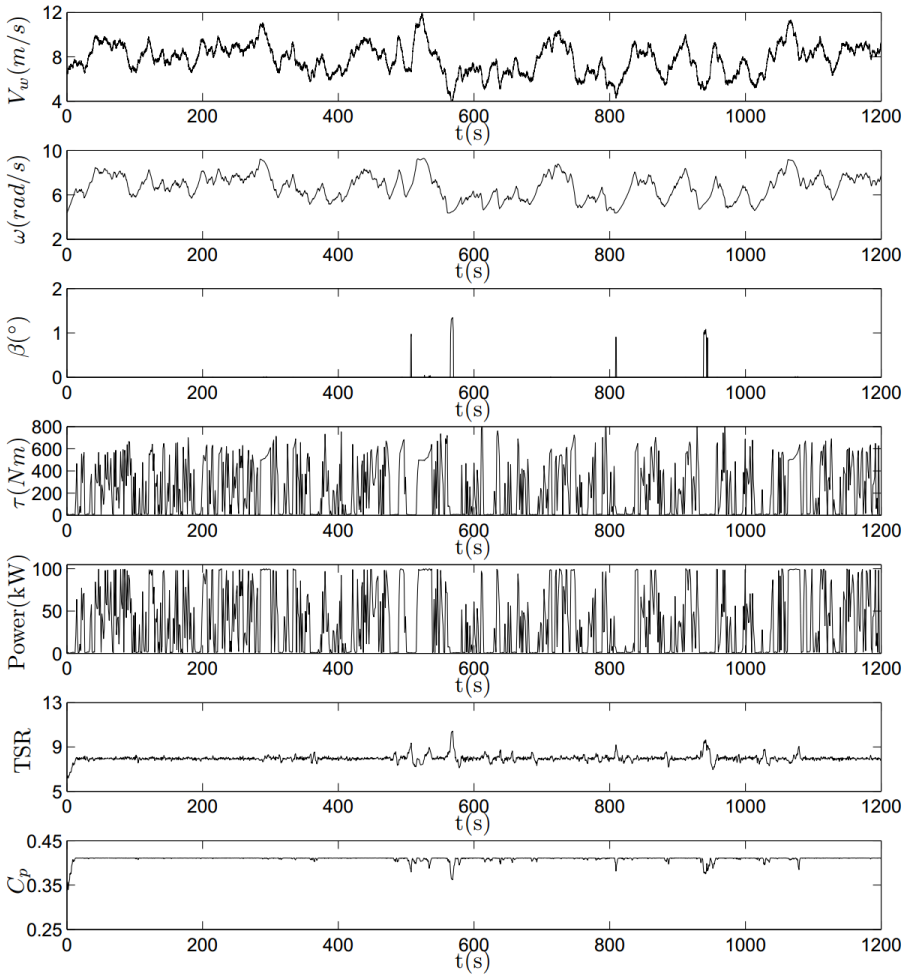

Figure 3.12: Results of the off-line dynamic programming optimization for a given wind profile.

The results of DP off-line optimization are shown in Figure 3.12 where the top plot is the wind speed profile. The subsequent plots provide the DP optimization results of rotor speed ω, pitch angle β, generator torque τ, generator power, TSR and turbine power coefficient C_p. Figure 3.12 reveals that by varying β and τ, an optimal C_p, and thus the maximum wind energy capture, can be achieved during this period. The maximum captured wind energy is calculated to be $4.3697\times10^7\,J$, which is the benchmark value for real-time control design. Figure 3.12 also shows that DP generates extremely large torque variance, which should be avoided in real-time control to maintain the turbine structural integrity and prolong its life.

The performance comparison of the STC, DPRC and LIDAR+DPRC controllers without considering model-plant mismatch is shown in Figure 3.13. The red dashed line in TSR plot denotes the optimal TSR value. Compared to the STC, the DPRC can track the optimal TSR better and thus is more efficient in energy harvesting. The DPRC captures 1.44% more energy than the STC for the given wind profile. However, since the DPRC is sensitive to wind speed fluctuation, more torque variance is generated due to fluctuating wind inflow. LIDAR technology is used to mitigate the influence of wind speed fluctuation by generating smoother wind speed measurements. As a result, the torque variance is reduced by 23.06% and the energy capture is further increased by 0.54% compared to DPRC using traditional wind speed estimator. Therefore, LIDAR+DPRC controller shows better performances than the original DPRC.

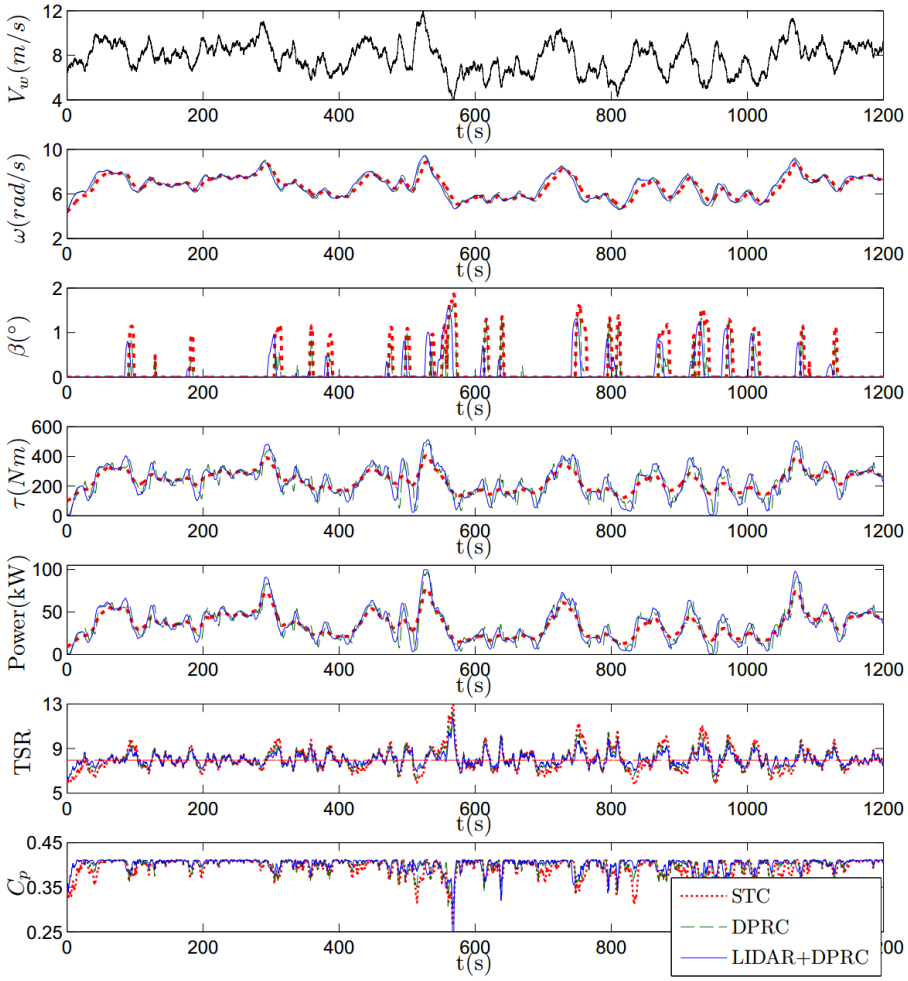

Figure 3.13: Performance comparison of the STC, DPRC and LIDAR-augmented DPRC controllers without considering model-plant mismatch.

Figure 3.14 compares the performances of the STC, GMOTC, and LIDAR+GMOTC controllers without having the model-mismatch. The GMOTC also has a faster response and more torque variance than the STC. With LIDAR measurement, the controller can reduce the torque variance and increase the energy capture at the same time. The above simulation results are summarized in Table 3.2. The effectiveness of each controller is evaluated based on the energy capture, energy capture percentage, and torque changing rate. The energy capture percentage is defined as the ratio between the

captured wind energy and the benchmark captured energy resulting from the off-line DP optimization. The torque changing rate refers to the average torque variance per second. From Table 3.2, one can see that the DPRC and GMOTC capture more wind energy with higher torque variance than the STC. Furthermore, adding LIDAR to both DPRC and GMOTC reduces the torque variance.

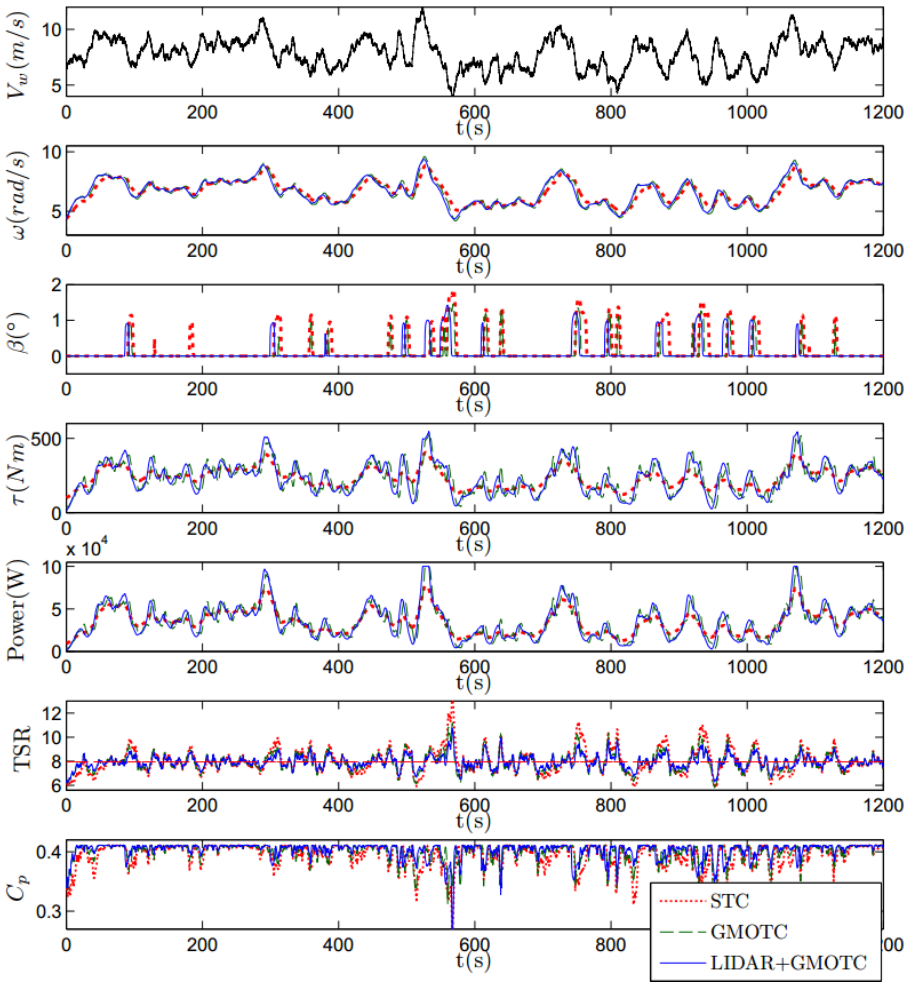

Figure 3.14: Performance comparison of the STC, GMOTC and LIDAR-augmented GMOTC controllers without considering model-plant mismatch.

Evaluation Parameters	Energy capture	Energy capture percentage	Torque changing rate(Nm/sec)
STC	4.2197	96.57	4.2809
DPRC	4.283	98.02	4.095
DPRC+LIDAR	4.3069	98.56	10.8447
GMOTC	4.2807	97.96	15.1055
GMOTC+LIDAR	4.3059	98.54	11.0209
Offline DP	4.3697	100	160.563

Table 3.2: Summarized simulation results without considering model-plant mismatch.

The above simulations assume no model-plant mismatch. In real world operation, however, model uncertainties, such as the estimation error in power coefficient, could impact the controller effectiveness. Next, we will quantify the impact of model-plant mismatch on the controller performances by considering an estimation error in turbine power coefficient as shown in Figure 3.6. In this study, LIDAR is used to provide a 10s wind speed preview for the controllers. The performance comparison of the STC, LIDAR+DPRC and LIDAR+GMOTC controllers with model-plant mismatch is shown in Figure 3.15. Simulation results reveal that the STC performance significantly deteriorates due to the power coefficient estimation error since the resulting generator torque feedback gain deviates 87% from its optimal value. The captured energy reduces to $2.8349\times10^{7}J$, which is only 67.18% of the energy captured using the STC with an optimal generator torque feedback gain. For the LIDAR+DPRC, the model-plant mismatch also causes it to lose optimality since the control look-up tables for DPRC are derived from the optimal power coefficient curve. In this case, the captured energy of LIDAR+DPRC reduces to $3.7214\times10^{7}J$, which shows a 13.59% energy loss compared to the LIDAR+DPRC with optimal look-up tables.

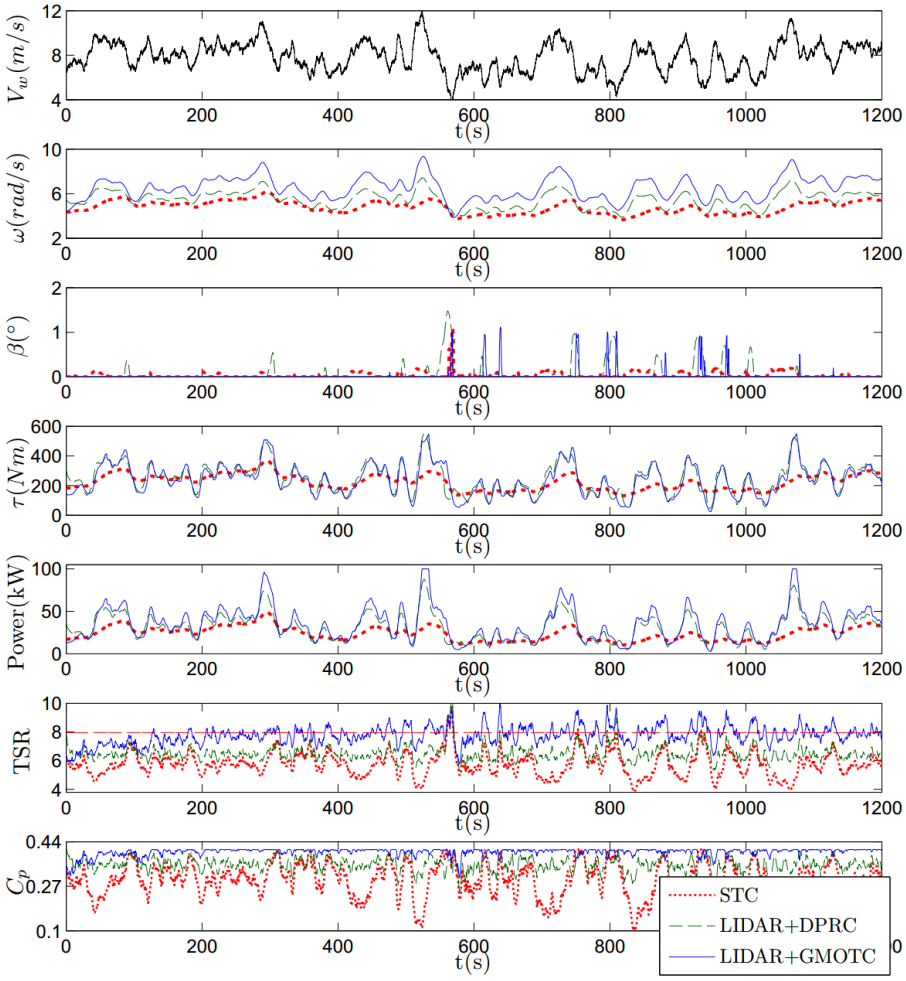

Figure 3.15: Performance comparison of the STC, DPRC and GMOTC controllers with model-plant mismatch.

On the other hand, the LIDAR+GMOTC allows the reference TSR to approach the optimal TSR in real-time by an adaptive algorithm. With the proposed internal PI technique, the controller can then converge to the optimal TSR under model-plant mismatch. Therefore, the turbine system will operate around the optimal TSR with optimized energy efficiency. Based on the same wind profile used in Table 3.2 analysis, the LIDAR+GMOTC captures wind energy of $4.2867\times10^{7}J$ which is only 0.45% less than that captured by the LIDAR+GMOTC based on accurate power coefficient values.

Therefore, the developed LIDAR-augmented GMOTC controller can quickly and robustly converge to the optimal operating point under model uncertainties.

3.7 SUMMARY

In this chapter, an online optimal control framework for a wind turbine is presented to maximize wind energy capture. Based on an off-line dynamic programming (DP) analysis, a DP-based real-time controller (DPRC) is developed. Specifically, the DPRC uses torque and pitch control look-up tables resulting from the off-line DP analysis. Simulation results show that the DPRC has a faster response to wind speed variation compared to the standard torque controller (STC). However, DPRC may lose optimality considering model-plant mismatch. In order to improve the controller robustness against model uncertainties, a gain modified optimal torque controller (GMOTC) is proposed as an alternative to the DPRC. The GMOTC drives the reference TSR to its optimal value by an adaptive searching algorithm and applies the internal PI technique to rapidly track this reference TSR. Compared to the DRPC, the GMOTC demonstrates similar performance in terms of accelerating turbine response to wind speed variation, and much improved robustness against model uncertainties. Minimizing the turbine torque variation is another important aspect of control design. Using the DPRC and GMOTC can dramatically narrow the gap of torque variation between the DP and STC, further reduction can be achieved by integrating LIDAR technology with the proposed control algorithm. Simulation results show that the LIDAR-augmented GMOTC enables the wind turbine to quickly and robustly converge to its optimal operating point without significantly increasing turbine torque variations.

Chapter 4: *Control Designs for Fatigue Loading Mitigation and Speed Regulation*

The available wind power increases as the wind speed and swept area increase. Wind speed increases as the hub height of a wind turbine increase. The swept area increases as the lengths of blades increase. As the sizes of modern wind turbines grow, the dynamic load acting on wind turbine structure also grows. The maintenance cost for a large wind turbine can be huge. To reduce the maintenance costs associated with wind turbine operation, development of control methodologies that mitigate the turbine fatigue loading is desired. In this chapter, control designs for fatigue loading mitigation are discussed. During partial load operation of a wind turbine, a new adaptive gain modified optimal torque controller (AGMOTC) is presented to mitigate fatigue loading in addition to energy maximization. A fatigue mitigation method is designed to reduce the impact of exacerbated tower bending moments due to the resonance effect. Simulation results show that the AGMOTC has improved efficiency and robustness in wind energy capture, better robustness against modeling uncertainties and reduced tower fatigue loading as compared to the traditional control technique. During full load operation of a wind turbine, a $\mathcal{H}_2$-norm minimization technique has been developed to optimize the gains of a Proportional-Integral blade pitch controller. Additionally, the controller is independent of wind speed measurement and hence it is very robust for practical applications. Using the $\mathcal{H}_2$-optimized blade pitch controller, the speed regulation performance is enhanced with reduced drivetrain fatigue loads.

Some portions of this chapter have appeared previously in the following publication:
Z. Ma, M. L. Shaltout, and D. Chen, "An Adaptive Wind Turbine Controller Considering Both the System Performance and Fatigue Loading," J. Dyn. Syst. Meas. Control, vol. 137, no. 11, p. 111007, 2015. (The author of this dissertation contributed to algorithm development, simulation and analysis)

Section 4.1 presents the modeling parameters of an NREL 5 MW wind turbine. The control designs for AGMOTC with fatigue mitigation technique and the $\mathcal{H}_2$ gain-scheduled blade pitch angle controller are detailed in Sections 4.2 and 4.3, respectively. Section 4.4 shows the simulation results of the proposed controllers. Finally, a summary is given in Section 4.5.

4.1 WIND TURBINE MODELING PARAMETERS

An NREL 5 MW wind turbine model [60] is used to demonstrate the effectiveness of the proposed controllers. The parameters of the system are shown in Table 4.1. For the purpose of control design and analysis, the equations of a one-mass wind turbine model as shown in (3.1) is used. The knowledge of the wind speed is essential for the proposed controller. Since the wind inflow is non-uniformly distributed over the rotor disc, the effective wind speed (EWS) over the rotor plane is used to calculate the effective TSR. The EWS, which represents the average value of the spatial wind field over the rotor plane, can be estimated using the method described in [90]. First, the rotor speed and aerodynamic torque are estimated based on state and input observers. These two variables and the measured pitch angle are then used to calculate the EWS by inversing a static aerodynamic turbine model.

Parameter	Magnitude
Generator rated power	5 MW
Rotor diameter	125.88 m
Hub height	90 m
Gear ratio	97
Rotor inertia	3.5444×10^{7} kg · m^2

Table 4.1: Continued next page.

Generator inertia	$534.116\ \text{kg} \cdot \text{m}^2$
Drivetrain inertia	$3.8759\times10^7\ \text{kg} \cdot \text{m}^2$
Air density	$1.225\ \text{kg/m}^3$
Tower equivalent mass	$4.38\times10^5\ \text{kg}$
Tower equivalent damping	$6421\ \text{N} \cdot \text{s/m}$
Tower equivalent stiffness	$1.846\times10^6\ \text{N/m}$
Optimal tip speed ratio	7.6
Optimal blade pitch angle	$0°$
Maximum power coefficient	0.4868
Cut-in wind speed	$3\ \text{m/s}$
Cut-out wind speed	$25\ \text{m/s}$
Rated wind speed	$11.4\ \text{m/s}$

Table 4.1: NREL 5 MW wind turbine model parameters.

The power coefficient C_p is a nonlinear function of the blade pitch angle and tip speed ratio, as shown in Figure 4.1. Here, the C_p surface is obtained using the WT_Perf program [91] developed by NREL for performance predictions of wind turbines based on the blade element momentum theory. The pentagram on the surface shows the simulation-derived optimal operating point where $\lambda^{opt} = 7.6$, $\beta^{opt} = 0°$ and $C_p^{opt} = 0.4868$. Generally, the blade pitch angle can be kept around β^{opt} during partial load operation. Additionally, the thrust force F_t acting on the rotor disc is given by (2.8), where C_t, the thrust coefficient, is a nonlinear function of the blade pitch angle and tip speed ratio, and is obtained using [91], as shown in Figure 4.2. The thrust coefficient C_t monotonically increases with the increase of TSR when the pitch angle is set to $0°$. Thus, the thrust force will continuously increase with the TSR and wind speed. The dynamics

of the thrust force could cause fatigue loads on the turbine structure, and should be attenuated by control design.

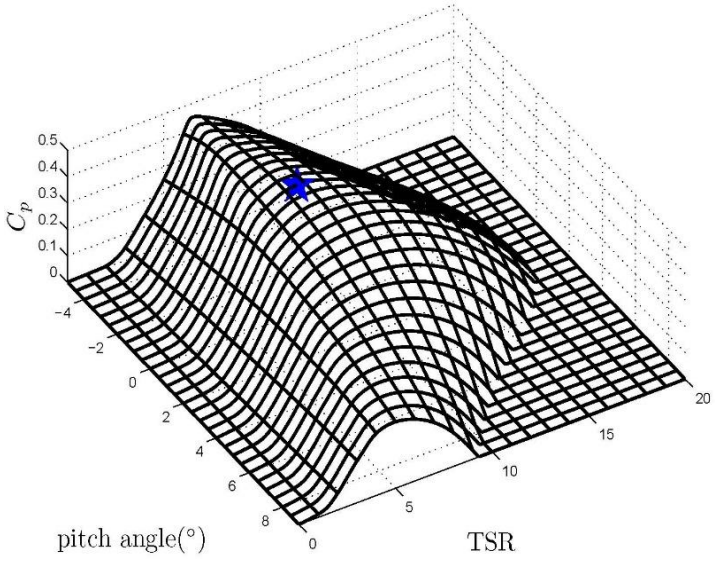

Figure 4.1: Power coefficient versus TSR and blade pitch angle for an NREL 5 MW wind turbine.

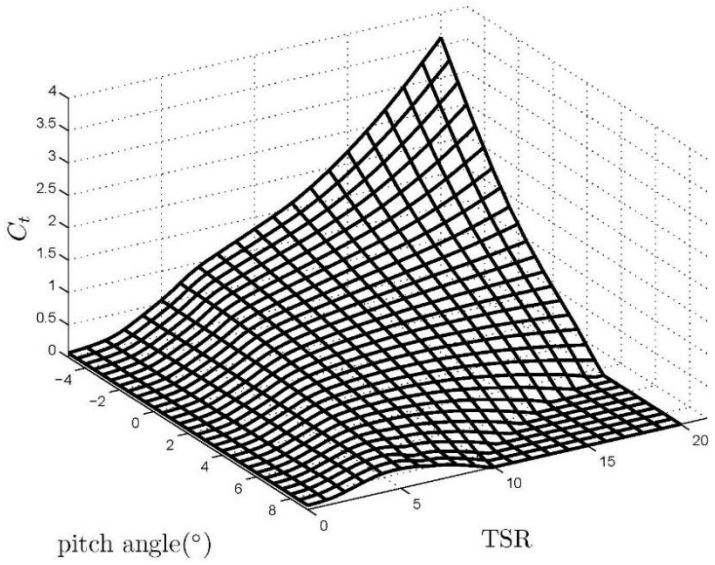

Figure 4.2: Thrust coefficient versus TSR and blade pitch angle for an NREL 5 MW wind turbine.

4.2 Adaptive Gain Modified Optimal Controller with Fatigue Mitigation Technique for Wind Turbine Partial Load Operation

The baseline controller for partial load operation, also known as standard torque controller (STC), controls the generator torque proportionally to the square of rotor speed. The STC is incapable of handling model uncertainty and attenuating fatigue loading. In order to overcome the limitations of STC, an adaptive gain modified optimal torque controller (AGMOTC) is proposed to enhance both the tracking performance of the optimal TSR and mitigating fatigue. Wind speed measurements are required for this controller. Hence, AGMOTC is preferable over STC when good wind speed measurement is available but an accurate wind turbine model is unavailable. The block diagram of the proposed AGMOTC controller is shown in Figure 4.3.

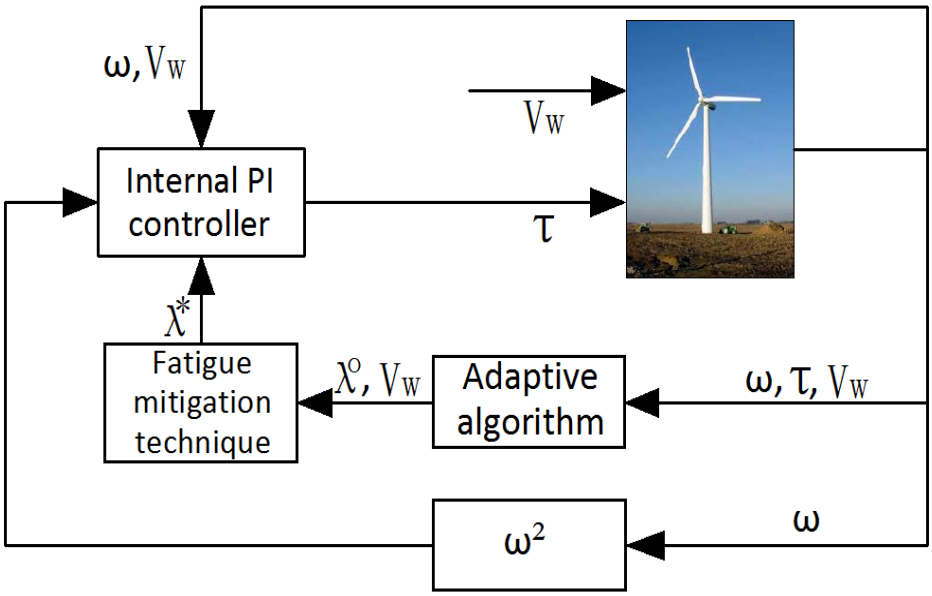

Figure 4.3: A simplified block diagram of a wind turbine system with the AGMOTC controller.

The proposed control law is as follows:

$$T_{g,cmd} = [K_{stc} + G_p(\lambda - \lambda^*) + G_i \int (\lambda - \lambda^*) dt]\omega^2, \quad (4.1)$$

where G_P and G_i are the internal Proportional-Integral (PI) gains. This internal PI technique is applied to accelerate the convergence of the effective TSR to its reference value. An adaptive approach to robustly search for the optimal reference TSR is also developed. A fatigue mitigation technique is then incorporated to avoid the tower resonance. The selections of internal PI gains are based on pole-placement approach as shown in Section 3.4. An empirical value for G_p can be obtained as $1\times10^{-5}D_r^5/G_r$. An empirical value for G_i can be obtained as 0.1 G_p. λ and ω are the measured tip speed ratio and rotor speed, respectively.

For a wind turbine system, there are two dominant bending moments acting on the base of turbine tower. With respect to the rotor plane, there is an out-of-plane moment, called the fore-aft moment, as well as an in-plane moment, called the side-to-side moment. Rotor thrust loads are the main cause for the tower fore-aft moments (TFAM), while rotor torque fluctuations are the main cause for the tower side-to-side moments (TSSM). Similarly, the wind turbine blades are subjected to two bending moments, which predominantly act on the root of the blades. One is an out-of-plane moment called the blade flapwise moment (BFM), while the other is an in-plane moment called the blade edgewise moment (BEM). The major causes of the BFM and BEM are the rotor thrust loads and the gravitational loads of blade self-weight, respectively.

In large wind turbines, the wind speed profile varies across the rotor disc, resulting in an asymmetric load on the blades [38]. This load is called a 1P component in the blade loads, as it repeats once per revolution of the rotor. Depending on the number of blades defined as N, the wind turbine tower will be subjected to N multiples of the 1P load per revolution. For instance, a 3-bladed rotor will transmit a 3P load component to

the turbine tower. The natural frequency for the first tower-bending modes of NREL 5 MW wind turbine can be obtained using the NREL BModes Code, and was found to be around 0.32 Hz [92]. The tower is mainly affected by the 3P component of the applied load on the rotor disc. Thus, a rotor speed near 6.4 rpm, or 0.1067 Hz (1P), will cause a 3P load to be transmitted to the tower at a frequency coinciding with its natural frequency. This will cause severe fatigue loading conditions for the tower, and thus should be avoided. To avoid the resonant operating zone, the reference TSR is designed as:

$$\lambda^* = \begin{cases} \lambda^o & (\frac{2\lambda^* V_w}{D_r} > \omega_{min}) \\ \frac{\omega_{min} D_r}{2V_w} & (\frac{2\lambda^* V_w}{D_r} \leq \omega_{min}) \end{cases} \tag{4.2}$$

where ω_{min} is the designed lowest rotor speed. Since the proposed controller can robustly converge to the reference TSR, the rotor speed is guaranteed to be higher than ω_{min} as time proceeds. However, a larger value of ω_{min} may negatively influence the tracking performance of the optimal TSR, and thus undermine the energy capture as well. The value of ω_{min} is designed to avoid critical rotor speed that can cause tower resonance. Using tower parameters as shown in (2.7), natural frequency of the tower can be derived as $\sqrt{K_{twr}/M_{twr}}$. In order to keep the frequency of induced force away from tower natural frequency, an empirical ω_{min} to avoid NP load can be determined as:

$$\omega_{min} = \frac{1.3\sqrt{K_{twr}/M_{twr}}}{N}. \tag{4.3}$$

The proposed fatigue mitigation technique mainly focuses on avoiding the resonance between the tower's natural frequency and the 3P load component. As a result, the proposed fatigue mitigation technique is expected to have a noteworthy influence on

the TSSM and TFAM mitigation. It should be noted that integrating this fatigue mitigation technique into the proposed control algorithm is inherently simple as compared to existing control algorithms. For instance, in the case of the STC, adding a constraint on the rotor speed to avoid exciting the tower's natural frequency requires major change of the control design. While for the proposed AGMOTC, the constraint can be added through setting a lower limit of ω_{min} in (4.2). Additionally, the highly computational cost of other controllers such as nonlinear model predictive control [47] has impeded their application in real time. λ^o in (4.2) denotes the optimal reference TSR that is determined on-line using an adaptive approach slightly different from that has been described in Section 3.4. Every T seconds, the algorithm calculates the average TSR (λ_{avg}) and the standard deviation of TSR (λ_{sd}) during this time period. Also, the average power coefficient during this period is estimated as:

$$C_{p,avg} = \frac{1}{T}\int_{t_0}^{t_f} \frac{\omega[\dot{\omega}J_d + T_g G_r]}{\frac{\pi}{8}\rho_{air} D_r^2 V_w^3}\, dt \tag{4.4}$$

where t_0 and t_f denote the start and end times of the period. Then, λ_{avg}, $1/\lambda_{sd}$ and $C_{p,avg}$ are recorded in sets Λ_1, Λ_2 and C, respectively. Let $X_{n\times 1} = \{x_1, \dots, x_n\}$ denotes the largest subset of Λ_1, such that $|x_i - \lambda^o| < \delta$ is satisfied $\forall x_i \in X_{n\times 1}$. $W_{n\times 1} = \{w_1, \dots, w_n\}$ and $Y_{n\times 1} = \{y_1, \dots, y_n\}$ denote subsets of Λ_2 and C that correspond to $X_{n\times 1}$. If $n < N$ where N is the smallest required size, the adaptive algorithm proceeds without updating λ^o. Otherwise, an adaptive approach based on a locally weighted linear regression method is applied as follows:

$$\begin{cases} \lambda^o(k+1) = \lambda^o(k) + s \cdot sign\left[\sum_{i=1}^{n} w_i(x_i - \overline{X})(y_i - \overline{Y})\right] \\ s = \alpha \left| \dfrac{\sum_{i=1}^{n} w_i(x_i - \overline{X})(y_i - \overline{Y})}{\sum_{i=1}^{n} w_i(x_i - \overline{X})^2} \right| \\ s_{min} \le s \le s_{max} \end{cases}, \quad (4.5)$$

where $\overline{X}$ and $\overline{Y}$ refer to the mean value of X and Y, respectively. α is an influence factor of the step size s A lower-bound step size s_{min} is selected to prevent the adaptation rate from slowing too severely. The step size is also limited by an upper-bound, s_{max} to minimize the effect of sudden disturbances or measurement errors on the wind turbine. This adaptive technique allows the controller to robustly converge to the optimal operation of a wind turbine system.

The AGMOTC as expressed in (4.1), has 4 major parameters, namely, the STC gain (K_{stc}), internal PI gains (G_p, G_i) and reference TSR (λ^*). K_{stc} is the same control gain as in STC. G_p and G_i are tuned for gain scheduling to accelerate the controller's convergence to λ^*. As shown in (4.2) - (4.5), a fatigue mitigation technique and an adaptive searching algorithm is applied to λ^* to mitigate tower loads, reject system uncertainties as well as compensate for the estimation error of K_{stc}. The proposed controller will enable a fast and robust convergence to the optimal TSR.

4.3 $\mathcal{H}_2$ Gain-scheduled Pitch Controller During Full Load Operation

During wind turbine full load operation, the power output is maintained at the rated power of generator. Blade pitch are controlled to adjust the rotor speed around its rated value. The baseline controller as shown in (2.13) applies a gain scheduled pitch control to minimize the deviation between the rotor speed and its rated value under varying wind speed. Unfortunately, the simple gain-scheduling law cannot retain

consistent response characteristics across all of Region 3 [60]. Also, a systematic gain scheduling approach for general wind turbine Region 3 control is desired. In this section, an $\boldsymbol{\mathcal{H}_2}$ gain scheduling approach is developed to optimize the proportional/integral gains of controller. The control design is based on a one-mass turbine model state equation as shown in (2.3). The friction coefficient is ignored for control design. At each wind speed, there exists an equilibrium pitch angle such that the aerodynamic power and generator power are both equal to the rated power. After applying a first order Tylor expansion to (2.3), a perturbed turbine dynamic equation can be obtained as:

$$J_d\Delta\dot{\omega} = \frac{P_{rated}}{\omega_{rated}} + \frac{\partial T_{aero}}{\partial \beta}\Delta\beta + \frac{\partial T_{aero}}{\partial \omega}\Delta\omega + \frac{\partial T_{aero}}{\partial V_w}\Delta V_w - (\frac{P_{rated}}{\omega_{rated}} - \frac{P_{rated}}{\omega_{rated}^2}\Delta\omega) \tag{4.6}$$

where $J_d = J_r + G_r^2 J_g$ is the drivetrain inertia. Since $\frac{\partial T_{aero}}{\partial \omega}\Delta\omega$ is very insignificant compared to other two terms, (4.6) can be rewritten as:

$$J_d\Delta\dot{\omega} - \frac{\partial T_{aero}}{\partial \beta}\beta_{cmd} - \frac{P_{rated}}{\omega_{rated}^2}\Delta\omega = \frac{\partial T_{aero}}{\partial V_w}\Delta V_w - \frac{\partial T_{aero}}{\partial \beta}\beta_{eq} \tag{4.7}$$

where β_{eq} refers to the equilibrium pitch angle. Assuming $d = \frac{\partial T_{aero}}{\partial V_w}\Delta V_w - \frac{\partial T_{aero}}{\partial \beta}\beta_{eq}$ to be a Gaussian disturbance caused by wind speed variation and substituting β_{cmd} with (2.13), the controlled drive-train dynamic equation can be obtained as:

$$J_d\Delta\dot{\omega} + (-\frac{\partial T_{aero}}{\partial \beta}K_p - \frac{P_{rated}}{\omega_{rated}^2})\Delta\omega + (-\frac{\partial T_{aero}}{\partial \beta}K_i)\int \Delta\omega dt = d \tag{4.8}$$

where $\frac{\partial T_{aero}}{\partial \beta} = \frac{\pi}{8\omega_{rated}}\rho_{air}D_r^2 V_w^3 \frac{\partial C_p}{\partial \beta}$ can be calculated for each equilibrium pitch angle.

An optimal pitch controller should reduce the deviation of rotor speed from its rated value without causing large pitch angle changing rate. Based on controlled drivetrain dynamic equation in (4.8), the transfer function from wind disturbance to rotor speed deviation can be obtained as:

$$\frac{\Delta\omega(s)}{d(s)} = \frac{s/J_d}{s^2 + k_1 s + k_2}, \tag{4.9}$$

where

$$\begin{cases} k_1 = (-\dfrac{\partial T_{aero}}{\partial \beta} K_p - \dfrac{P_{rated}}{\omega_{rated}^2})/J_d \\ k_2 = -\dfrac{\partial T_{aero}}{\partial \beta} K_i/J_d \end{cases} \tag{4.10}$$

The transfer function from wind disturbance to pitch rate can be obtained as:

$$\frac{s\beta(s)}{d(s)} = \frac{1}{-\dfrac{\partial T_{aero}}{\partial \beta}} \frac{s[(k_1 + \dfrac{P_{rated}}{\omega_{rated}^2 J_d})s + k_2]}{s^2 + k_1 s + k_2} \tag{4.11}$$

In order to reduce both rotor speed deviation and pitch rate under wind speed variation, the $\mathcal{H}_2$ norm of the transfer functions in (4.9) and (4.11) should be minimized. Considering the trade-off between minimizing rotor speed deviation and pitch rate, a cost function is determined as:

$$J = W \left\| \frac{\Delta\omega(s)}{d(s)} \right\|_{\mathcal{H}_2}^2 + \left\| \frac{s\beta(s)}{d(s)} \right\|_{\mathcal{H}_2}^2 \tag{4.12}$$

where W indicates the relative importance of minimizing rotor speed deviation with respect to minimizing pitch rate. It can be obtained as $\dot{\beta}_{max}^2/\Delta\omega_{max}^2$, where $\Delta\omega_{max}$ and $\dot{\beta}_{max}$ are the maximum allowed rotor speed deviation and pitch rate respectively. After computing the $\mathcal{H}_2$ norms by a well-known state-space approach, the cost function can be rewritten as:

$$J = \frac{W}{2{J_d}^2 k_1} + \frac{1}{(\frac{\partial T_{aero}}{\partial \beta})^2} \frac{k_2(k_1 + \frac{P_{rated}}{\omega_{rated}^2 J_d})^2 + [k_2 - k_1(k_1 + \frac{P_{rated}}{\omega_{rated}^2 J_d})]^2}{2k_1} \tag{4.13}$$

J can be minimized by solving $\frac{\partial J}{\partial k_1} = \frac{\partial J}{\partial k_2} = 0$. As a result, k_1, k_2 are derived as:

$$\begin{cases} [9k_1^2 - 2\frac{P_{rated}}{\omega_{rated}^2 J_d} k_1 + (\frac{P_{rated}}{\omega_{rated}^2 J_d})^2](k_1 + \frac{P_{rated}}{\omega_{rated}^2 J_d})^2 = 4W(\frac{\partial T_{aero}}{\partial \beta})^2 / J_d^2 \\ k_2 = \frac{1}{2}[k_1^2 - (\frac{P_{rated}}{\omega_{rated}^2 J_d})^2] \end{cases} \tag{4.14}$$

According to (4.10), the proportional and integral gains K_p and K_i are in the form of:

$$\begin{cases} K_p(\beta) = (k_1 + \frac{P_{rated}}{\omega_{rated}^2 J_d}) J_d / (-\frac{\partial T_{aero}}{\partial \beta}) \\ K_i(\beta) = k_2 J_d / (-\frac{\partial T_{aero}}{\partial \beta}) \end{cases} \tag{4.15}$$

Since, the scheduled gain is obtained as an analytical form, it is computationally efficient for real-time applications. Also, it should be noted that the gain-scheduling approach is independent from wind speed measurements, which makes this approach robust and reliable for practical applications.

4.4 SIMULATION RESULTS

While the control designs are based on a one-mass wind turbine model, the high-fidelity wind turbine model provided by the NREL FAST Code [82] is used as the plant for simulation. The following degrees of freedom are enabled in the high-fidelity model: drivetrain mode, generator mode, first and second tower side-to-side modes, first and second tower fore-aft modes, first and second blade flapwise modes and first blade edgewise mode. The NREL TurbSim Code [89] is used to generate full-field wind profiles with the required mean wind speed and turbulence intensity. The proposed

controllers are tested under different wind conditions (i.e. wind classes). The wind speed ranges for different wind classes at a 50 m hub height were obtained from [93], and were adapted to a height of 90 m using vertical extrapolation based on the 1/7 power law [94].

a. Control Performance of AGMOTC during Partial Load Operation

To investigate the effectiveness of the controller design on rejecting model uncertainties and mitigating fatigue loads, the proposed AGMOTC is compared to the STC method. The turbine fatigue was evaluated by the damage equivalent load (DEL), which is a single number to quantitatively indicate the damage caused by fatigue loadings acting on a wind turbine [38], [41], [43], [44]. In this study, the DELs were obtained using a rainflow-counting algorithm with the NREL MLife Code [95]. We compare the controller performance with respect to energy capture, tower side-to-side moment (TSSM) DEL, tower fore-aft moment (TFAM) DEL, blade edgewise moment (BEM) DEL and blade flapwise moment (BFM) DEL. Wind profiles with an average wind speed corresponding to wind classes 2 to 5 plus 25% turbulence intensity are used for simulations of wind turbine partial load operation. The simulation results of both cases, with and without prediction errors of the optimal torque control gain K_{stc}, are presented to show the controller robustness.

A performance comparison between the STC and AGMOTC on energy capture is shown in Figure 4.4. A wind speed profile for wind class 4 is selected as an example and shown in the top subplot of Figure 4.4. The mean wind speed of the selected wind profile is around 8 m/s, which is typical for partial load operation. Since the wind inflow is non-uniformly distributed, the rotor effective wind speed profile is shown here. The subsequent subplots compare the rotor speed ω, rotor torque τ_r, generator torque τ, TSR and generator power, respectively. Compared to the STC controller, the TSR of the

AGMOTC oscillates around 8, which is higher than the theoretical optimal value of 7.6. This is due to that the optimal TSR is shifted by a non-uniform distribution of wind inflow and blade deflections. This finding has been verified by [27], where the true optimal TSR is slightly higher than the simulation-derived value obtained using the un-deflected rotor blades. As shown in Figure 4.4, the AGMOTC controller captures 0.44% more wind energy than the STC does.

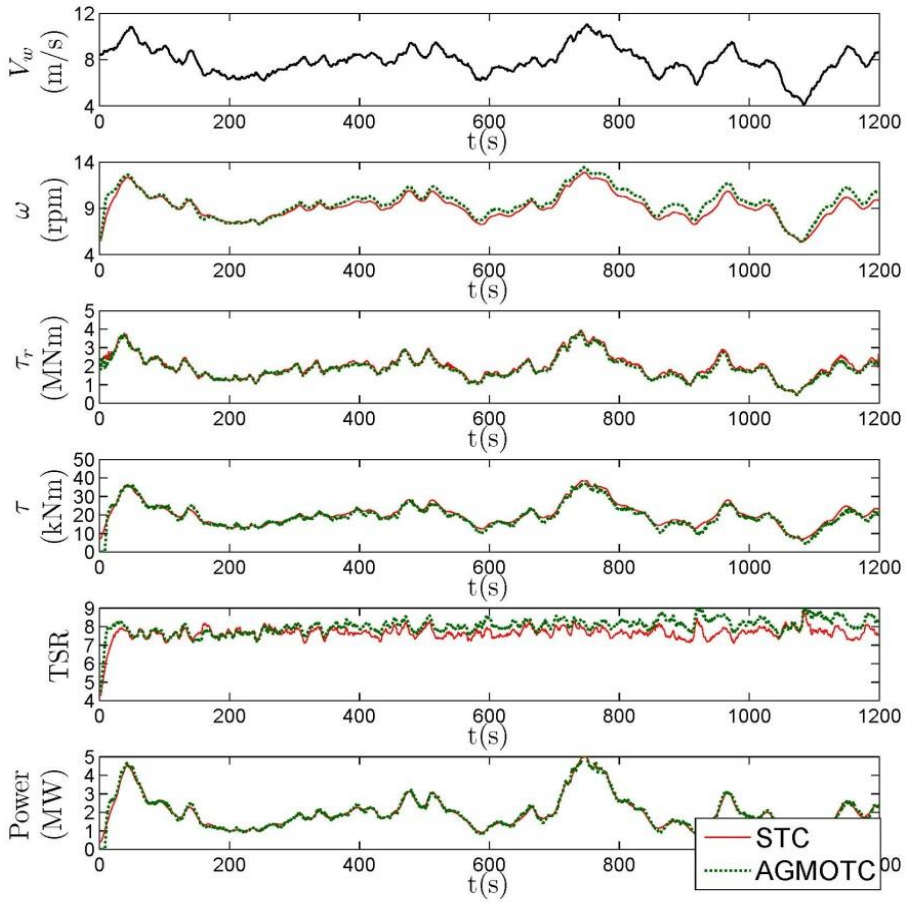

Figure 4.4: Performance comparison between the STC and AGMOTC without considering prediction error in K_{stc} for wind class 4.

A fatigue loading comparison between the STC and AGMOTC that does not consider the prediction error of K_{stc} is shown in Figure 4.5, which includes the simulation results of TSSM, TFAM, BEM, and BFM. Figure 4.4 indicates that the drop in the rotor torque profile of AGMOTC controller leads to a decrease in the average TSSM by 5.5%. On the other hand, using the AGMOTC causes higher TSR, hence increased rotor thrust load. As a result, the average TFAM and BFM are increased by 3.26% and 3.19%, respectively. There is a tradeoff among these DELs. It should be noted that the BEM is mainly affected by the gravitational loads, and negligibly affected by the proposed controller.

In real world operation, however, the unpredictable system uncertainties and estimation errors in power coefficient surface may lead to an inaccurate prediction of K_{stc}. In [28], the experiments on Controls Advanced Research Turbine (CART) showed that the simulation-derived prediction of K_{stc} was almost 2 times the turbine's true optimal torque control gain. To show the robustness of the proposed controller, it is necessary to compare the performance of both controllers considering the prediction error of K_{stc}.

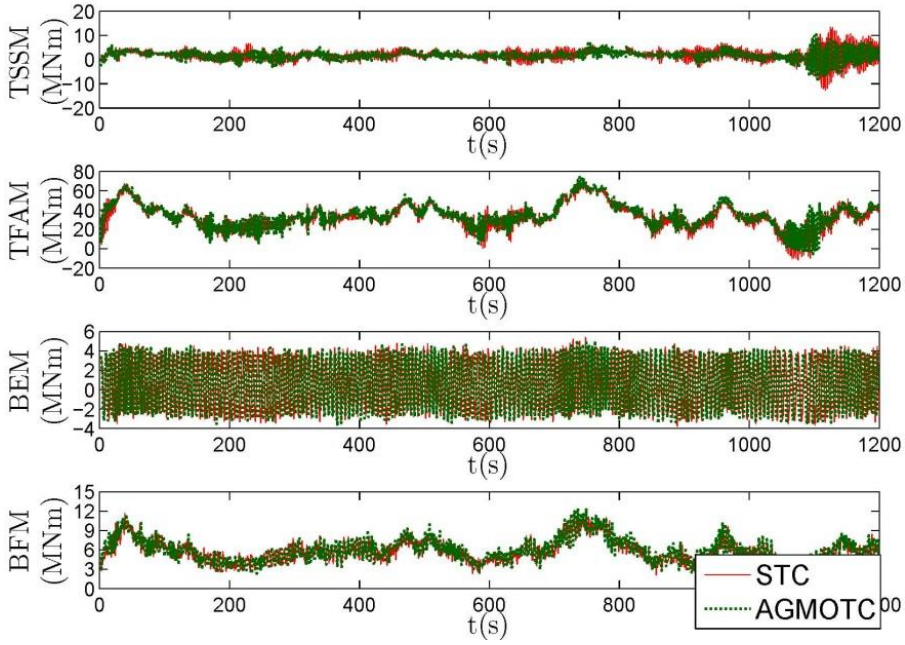

Figure 4.5: Fatigue loading comparison between the STC and AGMOTC without considering prediction error in K_{stc} for wind class 4.

In the following simulations, we adopt the prediction error of the K_{stc} used in [28]. Consequently, a 15% estimation error of the initial reference TSR (i.e. $\lambda^* = 0.85\lambda^{opt}$) was inversely calculated to test the robustness of proposed adaptive algorithm in searching for the optimal TSR. Using the same wind input as that in Figure 4.4, Figure 4.6 and Figure 4.7 compare the performance of STC and AGMOTC controllers. The AGMOTC captures 8.78% more wind energy than the STC. The lower rotor torque of the AGMOTC leads to an 11.07% decrease in the average TSSM. The higher TSR of the AGMOTC, hence the rotor thrust load, causes the average TFAM and BFM to increase by 16.8% and 17.2%, respectively.

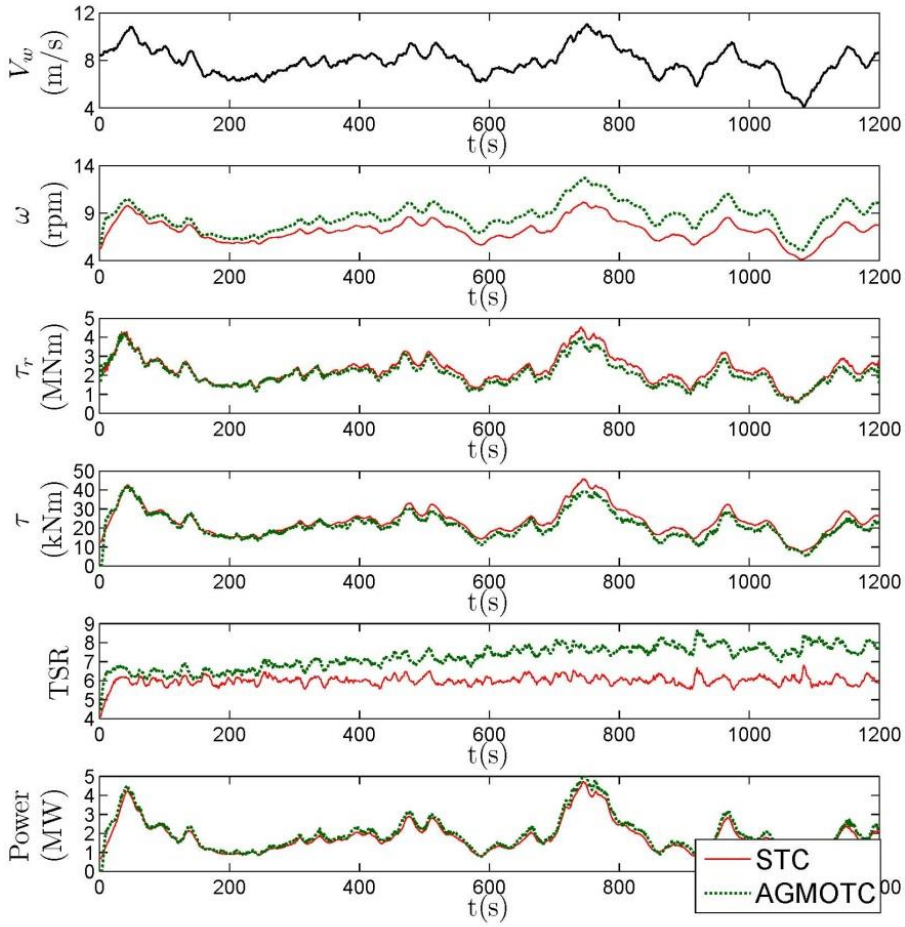

Figure 4.6: Performance comparison between the STC and AGMOTC considering prediction error in K_{stc} for wind class 4.

The TSR subplot in Figure 4.6 clearly shows the effect of the K_{stc} prediction error on the optimal TSR tracking for the STC as compared to the AGMOTC. Due to the large prediction error of the optimal K_{stc}, the TSR of STC significantly deviates from the optimal value. As opposed to the STC, the AGMOTC with an internal PI technique and an adaptive algorithm schedules the control gain, and allows the TSR to converge to its optimal value. As a result, the AGMOTC captures about 7.5% more wind energy

compared to the STC when the K_{stc} prediction error is considered. For turbine fatigue mitigation, the AGMOTC shows improvement on TSSM compared to the STC.

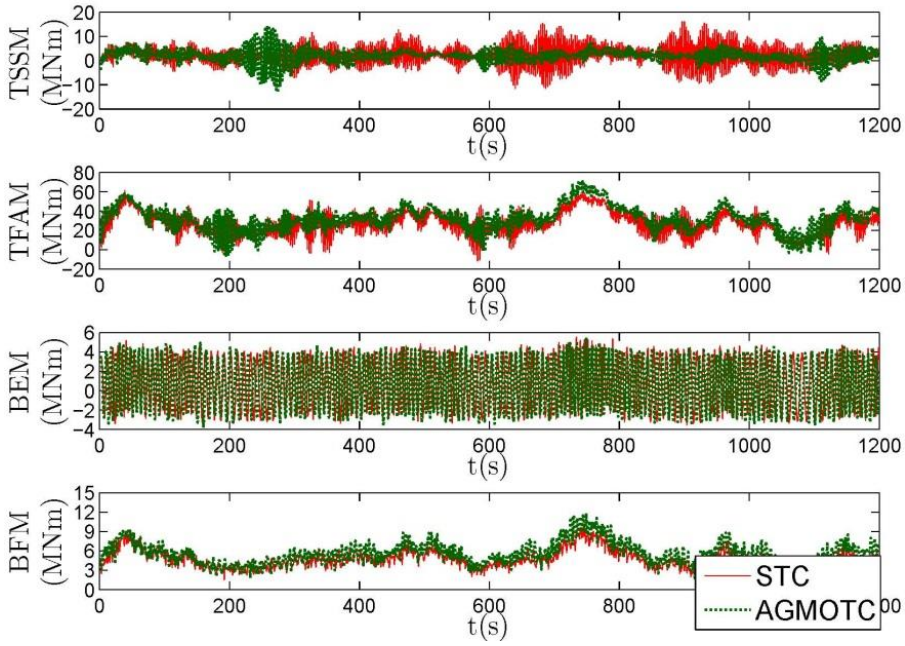

Figure 4.7: Fatigue loading comparison between the STC and AGMOTC considering prediction error in K_{stc} for wind class 4.

In order to further reduce the fatigue loading on the wind turbine, especially the resonance effect, a technique was proposed in Section 4.2, where the value of ω_{min} in (4.2) is set at 8.5 rpm to avoid the 6.4 rpm critical rotor speed. Figure 4.8 shows the impact of the fatigue mitigation technique on the rotor speed, generator power, and TSSM profiles. A significant reduction on tower fatigue loading can be detected. The top subplot of Figure 4.8 shows the rotor speed for the fatigue mitigated AGMOTC, denoted as AGMOTC*, is controlled to be higher than ω_{min} (i.e. 8.5 rpm), thereby avoiding the critical speed at 6.4 rpm. As a result, the AGMOTC* controller successfully protects the wind turbine rotor from operating near the critical speed. The FFT analysis result of

TSSM, shown in Figure 4.9, also reveals that there is a substantial drop in the peak load at the resonance frequency when using AGMOTC*. The decrease in the fatigue loading will increase the useful life of the turbine tower. It should be noted that the mitigation of the fatigue loads is achieved at the expense of the wind energy capture. With this fatigue mitigation technique, the energy capture of AGMOTC* is slightly reduced by 0.11% compared with that of AGMOTC, due to the non-optimal operation of the wind turbine. Since the resonance only happens when the rotor speed is lower than ω_{min} (i.e. 8.5 rpm), which corresponding to low wind speeds, only small amount of energy capture is sacrificed.

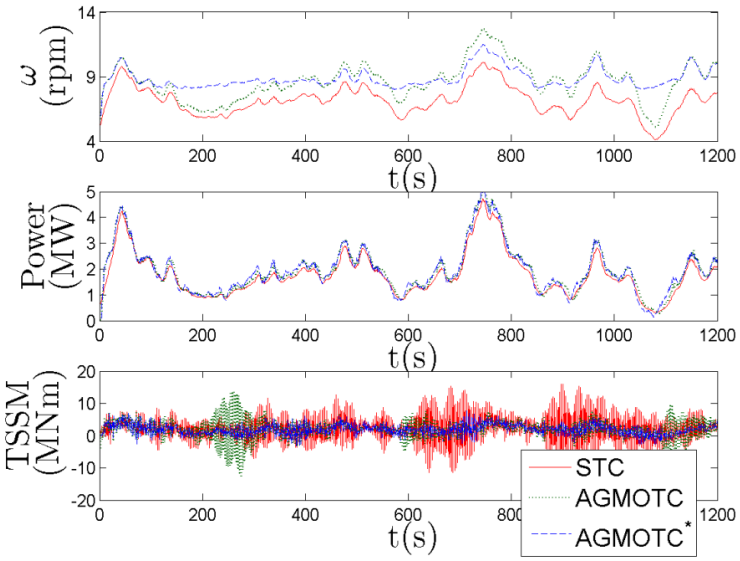

Figure 4.8: The effect of fatigue mitigation approach on the rotor speed, generator power, and TSSM for wind class 4.

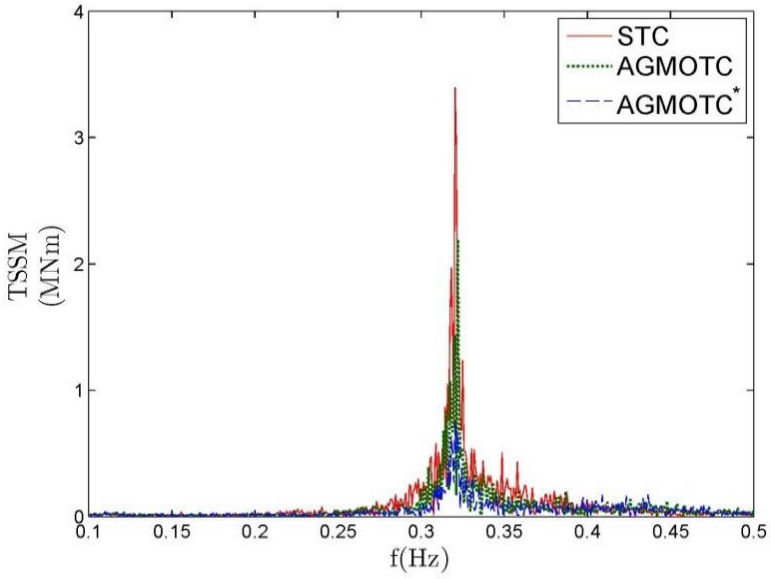

Figure 4.9: The effect of fatigue mitigation approach on the FFT of the TSSM for wind class.

In order to generalize the findings of the proposed ATMOTC* to a broad range of wind profiles, simulations were conducted under different wind conditions that represent wind classes 2 to 5. The simulation results with and without considering the prediction error of K_{stc} are summarized in Table 4.2 and Table 4.3, respectively. As shown in Table 4.2, an average energy improvement of 0.3% over the STC system is achievable using AGMOTC when the prediction error of K_{stc} is not considered. The improvement indicates that the AGMOTC with the internal PI technique can converge to the reference TSR faster and therefore can capture more energy, as compared to the STC. Table 4.3 shows that, when the prediction error of K_{stc} is considered, an average energy improvement of around 9% is obtained using AGMOTC as compared to STC. By integrating the adaptive optimal TSR searching algorithm, AGMOTC shows much better robustness over STC under system uncertainties.

Table 4.2 and Table 4.3 also show that implementing a fatigue mitigation technique leads to a considerable mitigation of the TSSM and TFAM and a slight sacrifice in the energy capture, because the tower resonance is avoided by applying a rotor speed limit control. The turbine rotor speed is controlled to be higher than the critical speed. Therefore, the tower fatigue loading can be significantly mitigated, and the rise of the TSR (i.e. higher thrust loads) remains the only cause of increased tower and blade fatigue loadings. In the case of zero prediction error in the control gain K_{stc}, compared to the STC, the proposed AGMOTC* tends to operate at a slightly higher TSR (as shown in Figure 4.4), thus a slight increase in the blade fatigue loadings. This cannot be said when there is a prediction error in the control gain.

With the prediction error in gain K_{stc}, the STC fails to track the optimal TSR, as shown in Figure 4.6. On the other hand, the proposed AGMOTC robustly tracks the optimal TSR, thus keeping the TSR profile nearly unchanged after introducing the gain prediction error. As the TSR significantly dropped in case of the STC, the blade fatigue loading also dropped substantially as compared to that of the proposed controller. It is worth mentioning that the proposed controller in this case did not cause additional blade loads, however it nearly sustained the same load levels acting on the blades as the previous case. Further blade fatigue mitigation can be achieved by using other control techniques, such as the individual pitch control; however, this will cause substantial energy loss in the partial load region and also beyond the scope of this work.

Wind Class	Controller	Energy capture ($\times 10^9\ J$)	TSSM DEL (MNm)	TFAM DEL (MNm)
2	STC	1.3564	17.1009	36.4635
	AGMOTC	1.3576(+0.09%)	9.6236(-43.72%)	35.2815(-3.24%)
	AGMOTC*	1.3533(-0.23%)	3.9966(-76.63%)	25.9191(-28.92%)
3	STC	1.8889	8.5989	35.5208
	AGMOTC	1.8953(+0.34%)	9.3248(+8.44%)	36.4752(+2.69%)
	AGMOTC*	1.8891(+0.01%)	5.4188(-36.98%)	34.8217(-1.97%)
4	STC	2.3889	15.4645	42.2431
	AGMOTC	2.3995(+0.44%)	11.5855(-20.08%)	42.1293(-0.27%)
	AGMOTC*	2.3987(+0.41%)	4.4899(-70.7%)	37.985(-10.08%)
5	STC	2.8112	14.4508	42.3735
	AGMOTC	2.8191(+0.28%)	5.4797(-62.08%)	39.1695(-7.56%)
	AGMOTC*	2.8183(+0.25%)	4.2262(-70.75%)	38.0147(-10.29%)

Table 4.2: Simulation results of the AGMOTC and the AGMOTC with fatigue mitigation technique (AGMOTC*) compared to the STC without considering prediction error of K_{STC} for wind classes 2 to 5.

Wind Class	Controller	Energy capture ($\times 10^9\ J$)	TSSM DEL (MNm)	TFAM DEL (MNm)
2	STC	1.2276	18.5069	33.7819
	AGMOTC	1.3416 (+9.29%)	15.7158 (-15.08%)	38.2090 (+13.1%)
	AGMOTC*	1.3420 (+9.32%)	4.3754 (-76.36%)	24.4069 (-27.75%)
3	STC	1.7080	21.4461	38.5424
	AGMOTC	1.8614 (+8.98%)	11.2945 (-47.34%)	36.8503 (-4.39%)
	AGMOTC*	1.8589 (+8.83%)	5.6768 (-73.53%)	29.7016 (-22.94%)
4	STC	2.1606	17.9493	41.2687
	AGMOTC	2.3502 (+8.78%)	16.2513 (-9.46%)	40.5681 (-1.69%)
	AGMOTC*	2.3476 (+8.66%)	6.6215 (-63.11%)	36.4885 (-11.58%)
5	STC	2.5734	17.1464	34.9662
	AGMOTC	2.7876 (+8.32%)	10.5041 (-38.74%)	40.3711 (+15.46%)
	AGMOTC*	2.7657 (+7.47%)	5.3927 (-68.55%)	34.569 (-1.14%)

Table 4.3: Simulation results of the AGMOTC and the AGMOTC with fatigue mitigation technique (AGMOTC*) compared to the STC considering prediction error of K_{STC} for wind classes 2 to 5.

b. Control Performance of $\mathcal{H}_2$ Gain-scheduled Pitch Controller during Full Load Operation

The control performance of the proposed H_2 gain-scheduled pitch controller is evaluated in this section. Figure 4.10 and Figure 4.11 show the scheduled proportional and integral gains with $\dot{\beta}_{max} = 8°/\,\mathrm{s}$ and different maximum allowed rotor speed deviations $\Delta\omega_{max}$ for the NREL 5 MW wind turbine. As a result of $\mathcal{H}_2$ optimization, the proportional gain decreases with the blade pitch angle while the integral gain increases with the blade pitch angle. The step responses of the controllers are compared in Figure 4.12, where the four subplots represent the wind speed, rotor speed, generator torque and blade pitch angle, respectively. The faster response of rotor speed against wind disturbance is at the expense of faster pitch rate. The tradeoff can be conveniently taken into account by adjusting maximum allowed rotor speed deviation. With the only tuning parameter of $\Delta\omega_{max}$, the control design can be easily and robustly adopted for a different wind turbine.

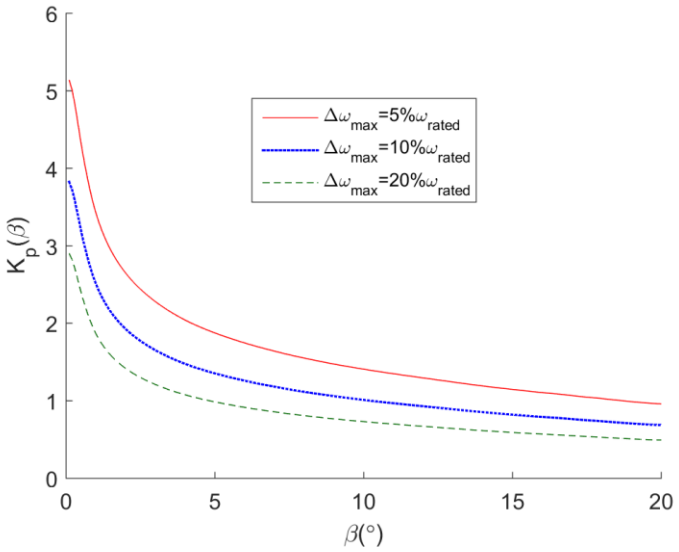

Figure 4.10: $\mathcal{H}_2$ scheduled proportional gain with different maximum allowed rotor speed deviations for the NREL 5 MW wind turbine.

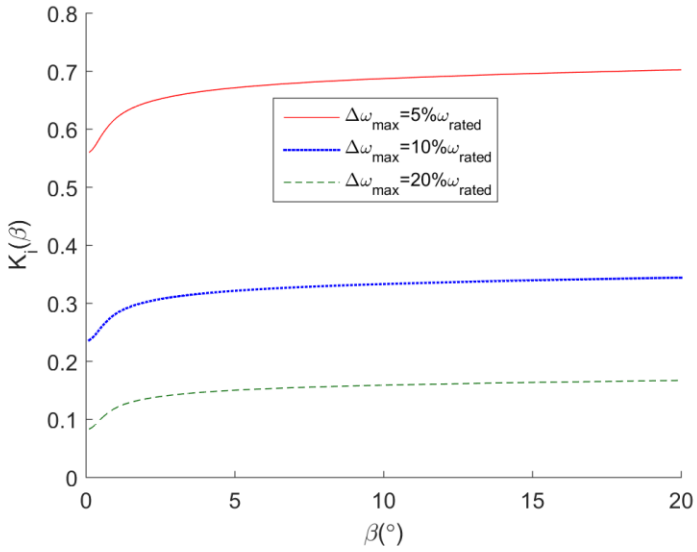

Figure 4.11: $\mathcal{H}_2$ scheduled integral gain with different maximum allowed rotor speed deviations for NREL 5 MW wind turbine.

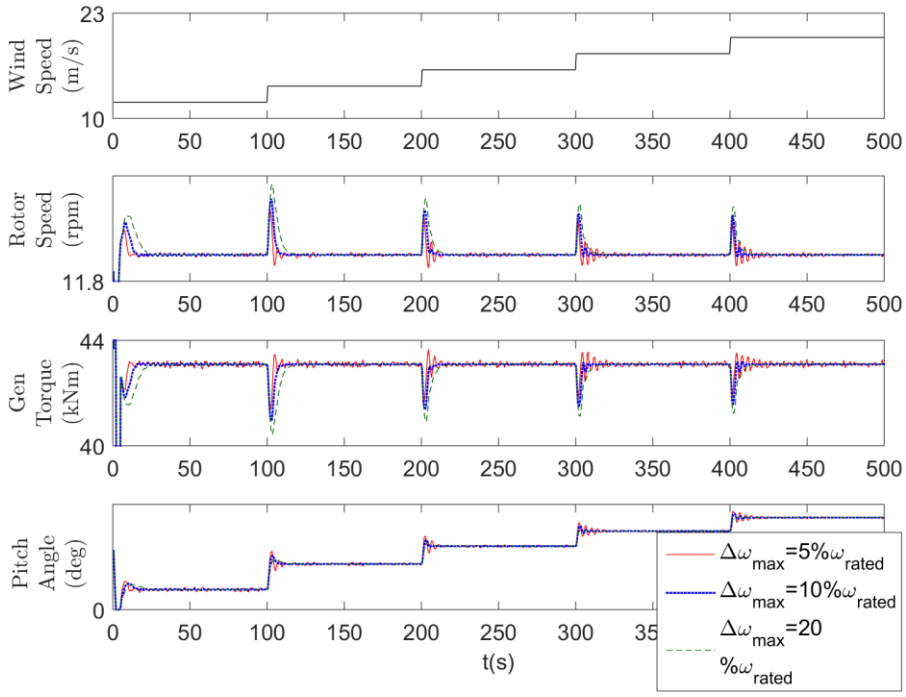

Figure 4.12: Comparison of $\mathcal{H}_2$ scheduled pitch controllers with different maximum allowed rotor speed deviations for NREL 5 MW wind turbine.

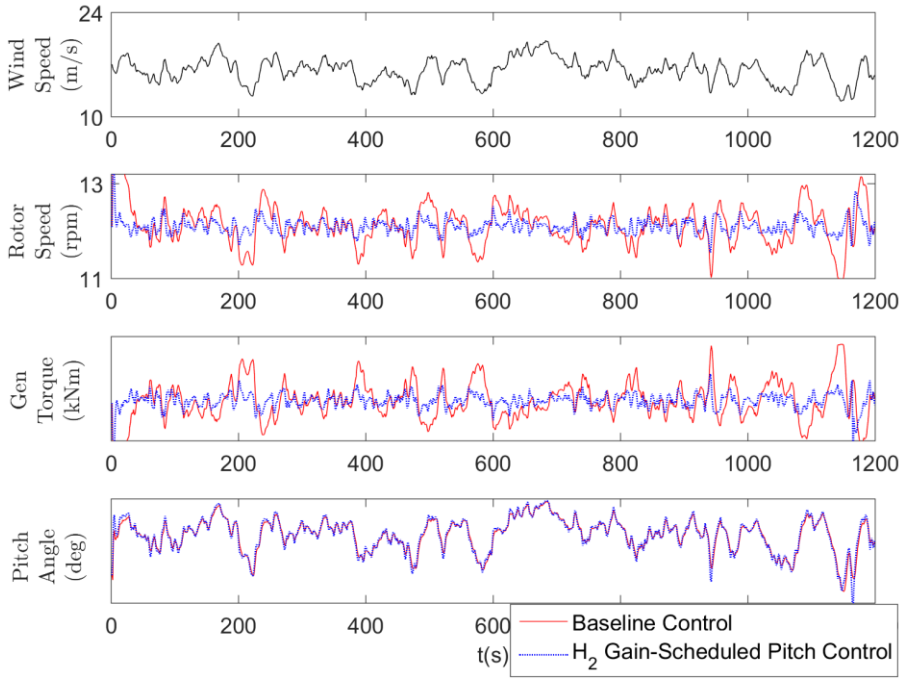

Figure 4.13: Comparison of baseline controller and $\mathcal{H}_2$ gain-scheduled pitch controller in terms of speed regulation during wind turbine full load operation.

To investigate the effectiveness of the controller design on speed regulation, the proposed $\mathcal{H}_2$ gain-scheduled pitch controller is compared to the baseline controller during full load operation. Since a wind turbine only operates in full load when the wind speed is above the rated value (11.4 m/s for NREL 5 MW wind turbine), a wind profile with an average wind speed corresponding to wind class 7 plus 25% turbulence intensity is used. The simulation results are shown in Figure 4.13 where the four subplots represent the wind speed, rotor speed, generator torque and blade pitch angle, respectively. By using the $\mathcal{H}_2$ gain-scheduled pitch controller, the standard deviation of rotor speed decreases from 0.45 rpm to 0.18 rpm by 60%. The generator torque oscillation is also reduced as rotor speed oscillation reduces. With less oscillations and over-speeding, the lifespan of generator is prolonged. Additionally, using the new control design results in a

17% reduction in drivetrain fatigue loading. The above improvement is achieved at the expense of a slightly increased pitch rate of 4%.

4.5 SUMMARY

In this chapter, control designs considering fatigue loading mitigation and speed regulation are presented. A new adaptive gain modified optimal torque controller (AGMOTC) is presented for wind turbine operation in the partial load region. A gain scheduling technique with an internal PI control is applied. The local eigenvalue of the controller around the equilibrium operating point is modified, and the controller response is accelerated. This leads to better tracking performance of the turbine reference TSR, and better energy capture when the wind speed varies significantly. An adaptive technique is also applied to search for the optimal reference TSR that enables the controller to converge to its optimal operating point under system uncertainties. The AGMOTC is further enhanced by applying rotor speed limit control to mitigate the tower fatigue. Simulation results show that the AGMOTC incorporated with the fatigue mitigation technique enables the wind turbine to rapidly and robustly converge to its optimal operating point with improved energy capture and reduced tower fatigue loading. Additionally, an $\mathcal{H}_2$ gain-scheduled pitch controller during wind turbine full load operation is proposed for optimizing speed regulation performance. The optimal gains are obtained by minimizing the $\mathcal{H}_2$-norms of the closed loop transfer functions from the wind disturbance to the rotor speed variations and pitch rate. Using the proposed control design effectively reduces the oscillations of rotor speed around its rated value with marginal increase in pitch rate.

Chapter 5: *Power Dispatch of an Integrated Wind Turbine and Battery System*

Historically, wind power is non-dispatchable due to its intermittence and unpredictability. In this chapter, control designs have been developed to overcome the wind intermittency. A normalized and standardized autoregressive moving average model (ARMA) is presented for short-term probabilistic wind speed prediction. With this information, battery energy storage systems (BESS) is integrated with wind turbines to mitigate wind intermittence and make wind power dispatchable as traditional power sources. Two phases of optimizations are proposed, namely, power scheduling and real-time control that allows an integrated wind turbine and BESS to provide the grid with consistent power within each dispatch interval. In the power scheduling phase, the desired battery state of charge (SOC) under each wind speed is first determined by conducting an offline probabilistic analysis on historical wind data. With this information, a computationally efficient one-step ahead model predictive approach is developed for scheduling the integrated system power output for the next dispatch interval. In the real-time control phase, novel control algorithms are developed to make the actual system power output match the scheduled target. A wind turbine active power controller is proposed to track the reference power set point obtained by a steady state optimization approach. By combining an internal integral torque control and a gain-scheduled pitch control, the proposed active power controller can operate around a desired tip speed ratio without an accurate knowledge of turbine power coefficient curve.

Some portions of this chapter have appeared previously in the following publications:

1. Z. Ma, M. L. Shaltout, and D. Chen, "Optimal Power Dispatch and Control of an Integrated Wind Turbine and Battery System," J. Dyn. Syst. Meas. Control, Mar. 2017. (The author of this dissertation contributed to algorithm development, simulation and analysis)
2. Z. Ma and D. Chen, "Optimal power dispatch and control of a wind turbine and battery hybrid system," in American Control Conference (ACC), 2015, 2015, pp. 3052–3057. (The author of this dissertation contributed to algorithm development, simulation and analysis)

Compared to the conventional power scheduling and real-time controller, implementing the new methodology significantly reduces the ramp rate, generator torque changing rate, battery charging rate and the power output deviation from the scheduled target. BESS with various capacities and different wind profiles are considered to demonstrate the effectiveness of the proposed algorithms on battery sizing.

Section 5.1 presents wind speed predictive models. The integrated wind turbine and battery system is illustrated in Section 5.2. Subsequently, a novel power scheduling and real-time controller for scheduled power tracking of the integrated system are detailed in Sections 5.3 and 5.4, respectively. Section 5.5 shows the simulation results of the proposed methodology. Finally, a summary is given in Section 5.6.

5.1 WIND SPEED PREDICTIVE MODELING

Wind speed prediction is crucial for wind power dispatch. However, the highly variable and non-stationary nature of wind speed makes it hard to be accurately forecasted. In this study, several wind speed forecasting approaches are presented and compared. Autoregressive and Moving Average (ARMA) model is employed to dig out the inherent characteristics of the wind speed variations. Since ARMA model works best for normally distributed data, the Weibull distributed wind speed is normalized by minimizing the skewness of time series. Also, the daily seasonality and non-stationarity is removed by standardizing the original wind speed time series. The transformation and standardization process leads to an adequate ARMA model with lower order and smaller prediction errors. The effectiveness of the ARMA model-based prediction is demonstrated using the wind speed time series from Bull Creek Wind Farm in Borden, Texas. This time series includes 30-min sampled wind speed and wind farm power output data from March 1st to June 28th, 2006. As shown in Figure 5.1, the time series are

divided into two parts. The data for the first 120 days are used as training samples while the last 30 days are for testing purpose.

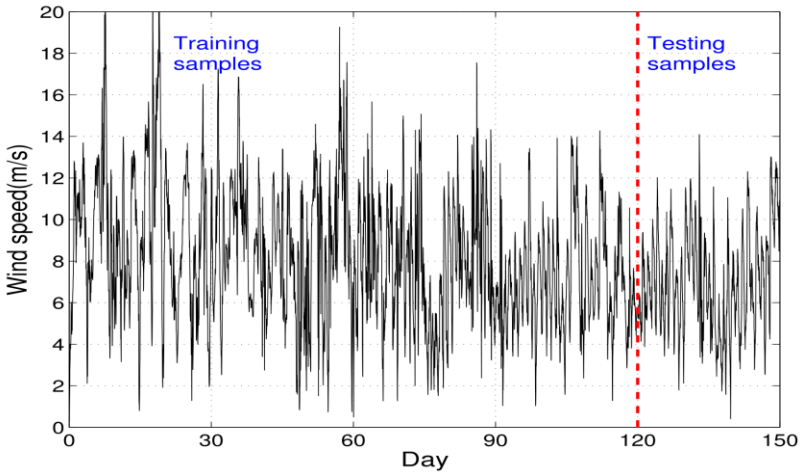

Figure 5.1: Wind data from March 1st to June 28th, 2006 from Bull Creek Wind Farm in Borden, Texas.

a. Persistence Method

Persistence method is commonly used for predicting wind speed. The method is taken as the baseline for comparison. The model assumes the best prediction is the current observation. So, the corresponding k-step ahead prediction at time t is given by:

$$\hat{X}_t(k) = X_t \tag{5.1}$$

where X_t is the time series value at time t. This method is computationally costless. It shows acceptable prediction accuracy for short-term prediction but large deviations for long-term cases.

b. Direct ARMA Modeling Based on Wind Speed Time Series

Autoregressive and Moving Average (ARMA) modeling is a linear stochastic modeling approach which combines the autoregressive and moving average process. The equation for an ARMA(n, m) model is as follows:

$$X_t - \phi_1 X_{t-1} - \cdots - \phi_n X_{t-n} = a_t - \theta_1 a_{t-1} - \cdots - \theta_m a_{t-m} \tag{5.2}$$

where $\phi_i (i = 1,2,\ldots n)$ and $\theta_j (j = 1,2,\ldots m)$ are the autoregressive and moving average parameters of the model, respectively. a_t is modeled as normal white noise with zero mean and a variance of σ_a^2 (i.e. $a_t \sim NID(0, \sigma_a^2)$). An ARMA(2n, 2n-1) engineering testing strategy is used to find the adequate model for the training samples of wind speed time series [96]. Using this strategy, an ARMA(13,12) model is found to be adequate. Figure 5.2 shows that the autocorrelations of the residuals are almost within the 95% confidence bounds, which indicates the adequacy of the fitted model. As shown in Figure 5.3, there is a pair of complex conjugate autoregressive roots, $1.0002e^{\pm 2\pi j/48.03}$, that are very close to the unit circle. The two roots indicate a periodicity of 48 which corresponds to a daily periodicity for a 30-min sampled time series. Figure 5.4 shows the results for 30-minute, 1-hour, 2-hour, 3-hour, 5-hour, 10-hour ahead predictions of the fitted model.

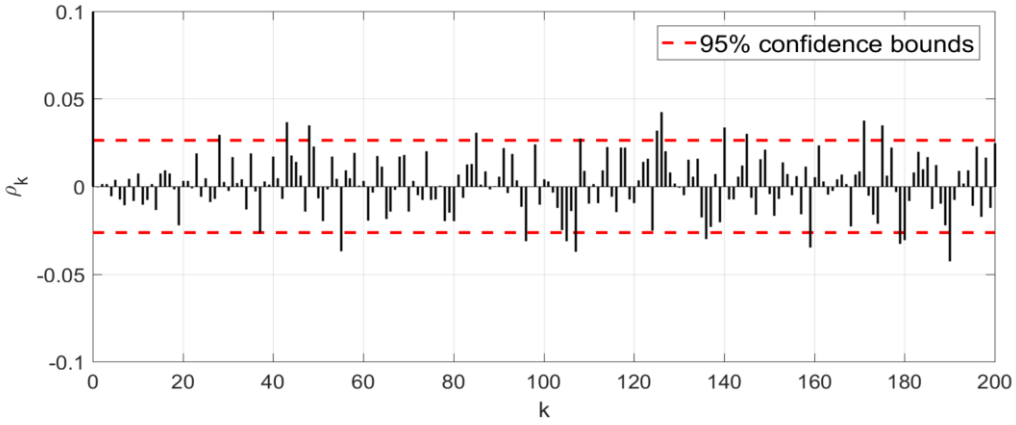

Figure 5.2: Autocorrelation test of ARMA(13,12) model.

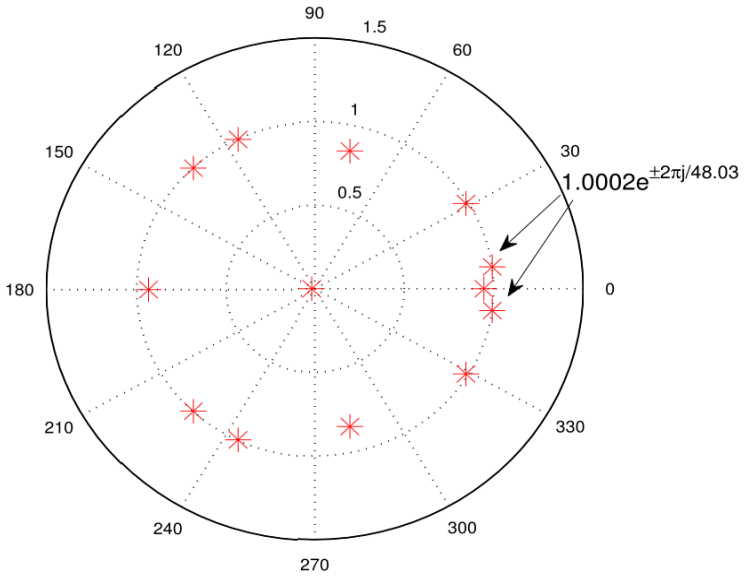

Figure 5.3: Autoregressive roots of ARMA(13,12) model.

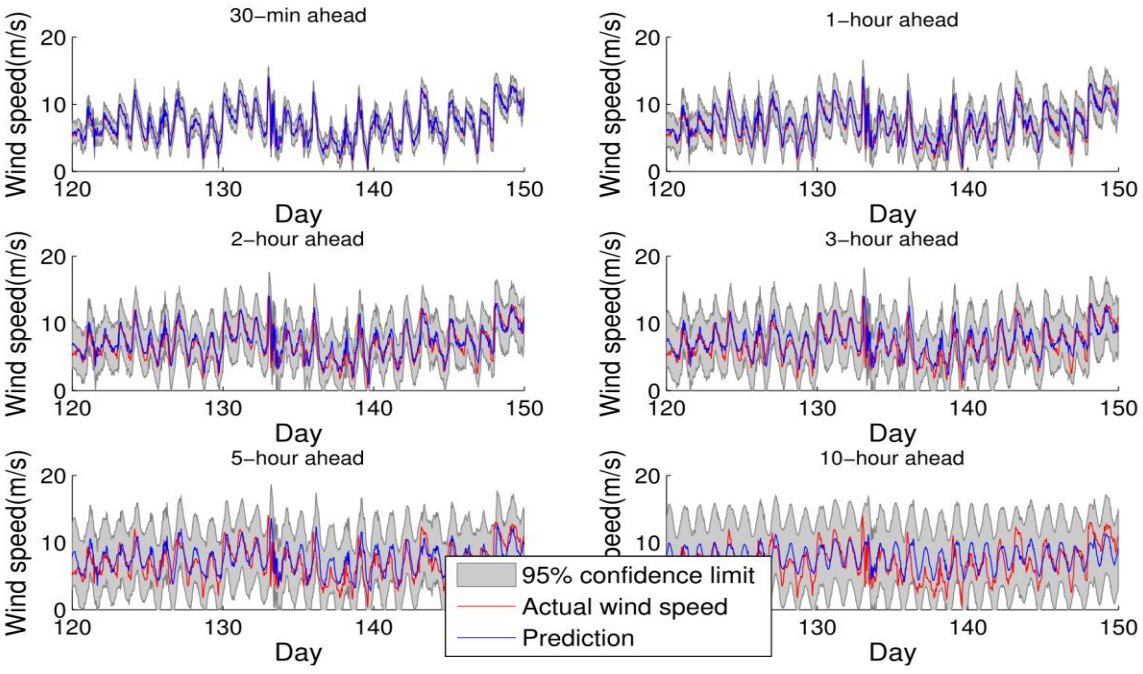

Figure 5.4: Wind speed prediction results of direct ARMA modeling.

c. Normalization and Standardization of Wind Speed Time Series

In ARMA theories, the residuals are assumed to be normally distributed. Although most natural phenomena, to certain extent, can be taken as normal process, the wind speed distribution is proved to be more of a Weibull distribution instead of Normal distribution. In order to take fully advantage of ARMA technology, there is a need to normalize the wind speed time series before modeling. The probability density function of Weibull distribution is as follows:

$$P(V) = \frac{K}{C}(\frac{V}{C})^{K-1}e^{-(\frac{V}{C})^K} \tag{5.3}$$

where K is the dimensionless form factor; C is a scale parameter; V refers to the wind speed. Several methods are proposed to determine the shape and scale parameters of the Weibull distribution function [97]. In this section, a maximum likelihood approach is adopted and the fitted parameters for the training wind speed samples are $C = 9.2252$, $K = 2.7515$. It can be shown that a Weibull distribution with a form factor K near 3.6 is close to Normal distribution [98]. A more accurate statistic way for normalizing data is to remove the skewness of the time series [99]. Each observation is raised to the power of x, $Y_t = X_t^x$. The value of x is calculated by minimizing the skewness defined as [100]:

$$S = \frac{\sum_{t=1}^{N}[(Y_t - \overline{Y_t})/\sigma(Y_t)\,]^3}{N}, \tag{5.4}$$

where N is the sample size; Y_t is the normalized wind speed time series; $\overline{Y_t}$ and $\sigma(Y_t)$ represent the mean value and the standard deviation of Y_t, respectively. To obtain the solution of x, Brent's method is applied with an initial guess $x_0 = K/3.6 = 0.7643$ where K is the form factor of Weibull distribution as above. Thus, x is found to be 0.7419 for the training wind speed time series. In addition, in order to de-trend the diurnal periodicity in wind speed time series, Y_t is standardized as follows:

$$\begin{cases} Z_{t+nk} = \dfrac{Y_{t+nk} - \mu(t)}{\sigma(t)} \\ \mu(t) = \dfrac{\sum_{k=1}^{d} Y_{t+nk}}{d} \\ \sigma(t) = \sqrt{\dfrac{\sum_{k=1}^{d} [Y_{t+nk} - \mu(t)]^2}{d}} \end{cases} \begin{pmatrix} 1 \le t \le n \\ 1 \le k \le d \end{pmatrix}, \tag{5.5}$$

where Z_t is the normalized and standardized wind speed time series. d and n are the number of days considered and the number of 30-min intervals per day, respectively. After applying the standardization approach, the non-stationarity due to diurnal trend is removed. An engineering F-testing strategy is applied to Z_t to find an adequate ARMA(6,1) model [96]. As shown in Figure 5.5, the autocorrelations are almost within the 95% confidence bounds and thus the fitted model is adequate. Figure 5.6 shows that the roots close to the unit circle have been successfully removed. Therefore, more stable prediction results can be obtained from the new model. The prediction of Z_t follows a normal distribution whose variance can be obtained using the Green's function coefficients of the obtained model [96]. By transforming the normal distribution back using (5.4) and (5.5), a skewed distribution of wind speed forecast can be achieved as $f(w_f)$ based on historical wind speed data. Figure 5.7 shows the results for 30-minute, 1-hour, 2-hour, 3-hour, 5-hour, 10-hour ahead predictions from the fitted model.

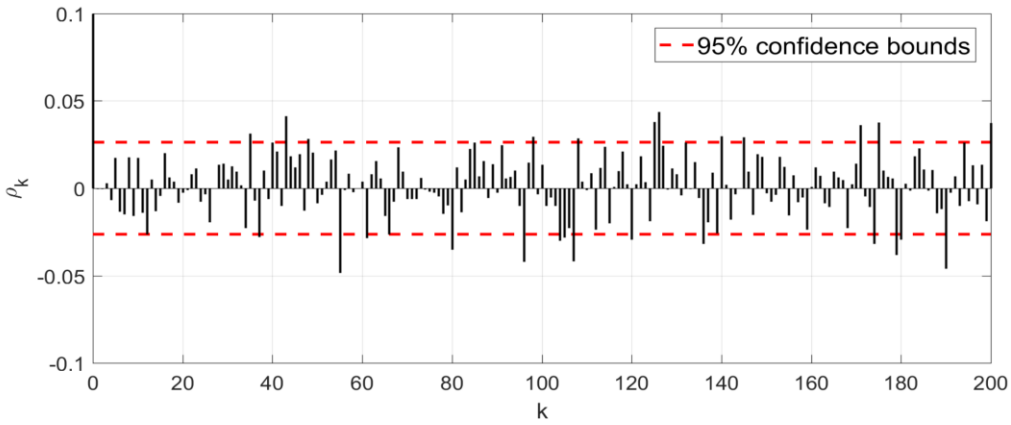

Figure 5.5: Autocorrelation test of ARMA(6,1) model.

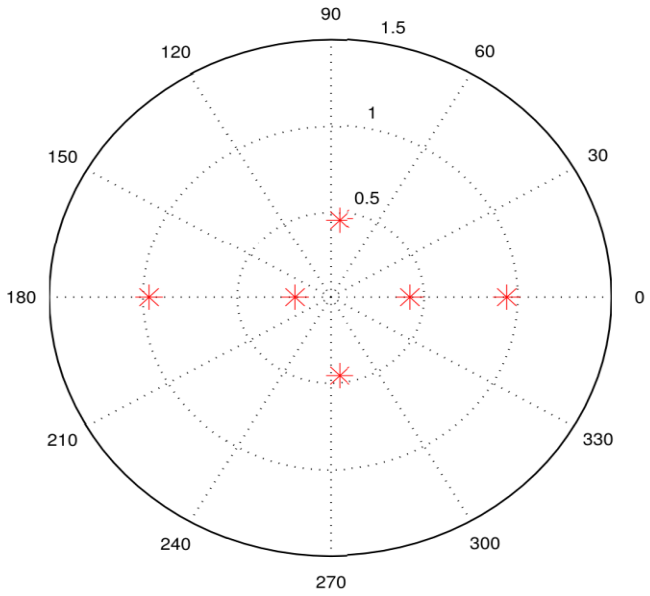

Figure 5.6: Autoregressive roots of ARMA(6,1) model.

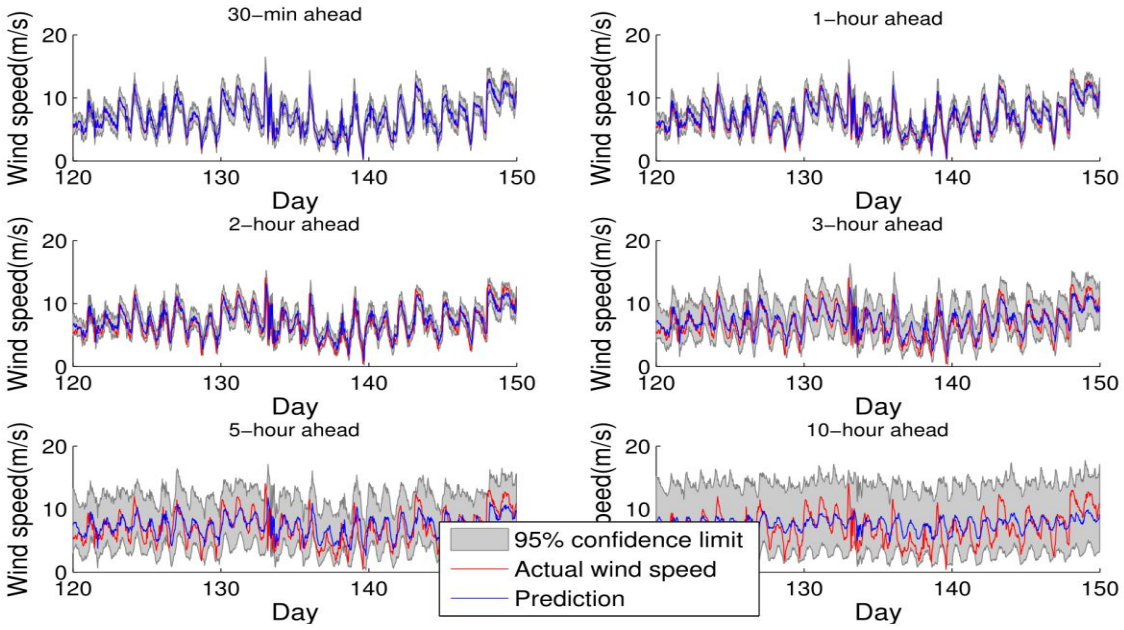

Figure 5.7: Wind speed prediction results of the normalized and standardized ARMA modeling.

d. Comparison of Wind Speed Prediction Methods

The errors of different wind speed prediction methods are compared in Table 5.1. The ARMA modeling approach shows a 10% improvement over the persistence method for 30-min ahead wind speed prediction. The improvement becomes more obvious as the predicted time increases and reaches up to 40% for 10-hour ahead prediction. By applying transformation and standardization to the original wind speed time series, both the order of the fitted ARMA model and the prediction variance are decreased. The prediction accuracy is further improved by around 2%. With least complexity and highest accuracy, the normalized and standardized ARMA modeling is most preferred among all methods.

RMSE (m/s)	Persistence Method	Direct ARMA Modeling	Normalized and Standardized ARMA modeling
30-min ahead prediction	0.5488	0.4924	0.4867
1-hour ahead prediction	0.9162	0.8316	0.8181
2-hour ahead prediction	1.4099	1.2163	1.1228
3-hour ahead prediction	1.8062	1.4783	1.4285
5-hour ahead prediction	2.4615	1.8873	1.7645
10-hour ahead prediction	3.3838	2.1451	2.0187

Table 5.1: Comparison of different wind prediction methods.

5.2 MODELING OF INTEGRATED WIND TURBINE AND BATTERY SYSTEM

A battery model is introduced in this section to describe the BESS. Assuming the energy loss associated with battery charging and discharging is negligible, a simplified Coulomb-counting model can be defined as：

$$\dot{SOC} = P_{batt}/Q, \tag{5.6}$$

where P_{batt} and Q refer to the battery charging power and capacity, respectively. In this study, the maximum charge or discharge rate is set at 1C (e.g. for a 1MWh BESS $|P_{batt}| \leq$1MW). High charge or discharge rates could lead to cracking or crystal growth that negatively affects the internal impedance of the cell, thus reduce the battery capacity [101]. Also, the depth of discharge may reduce the useful life of the battery and drive the BESS into an uncontrollable level. To avoid such undesirable operation, the range of SOC is limited between 20% and 80%.

The BESS model is integrated with an NREL 5 MW wind turbine model as shown in Section 4.1. The integrated system is illustrated in Figure 5.8. It is assumed that

the power dispatch occurs every 30 minutes. Based on the wind speed forecast, the power output is scheduled and reported to the grid operator 5 minutes before the next 30min period starts. A real-time controller is then applied to track the scheduled power output within each 30 minutes. The manipulated variables of the system include the wind turbine generator torque, pitch angle and battery charging/discharging power.

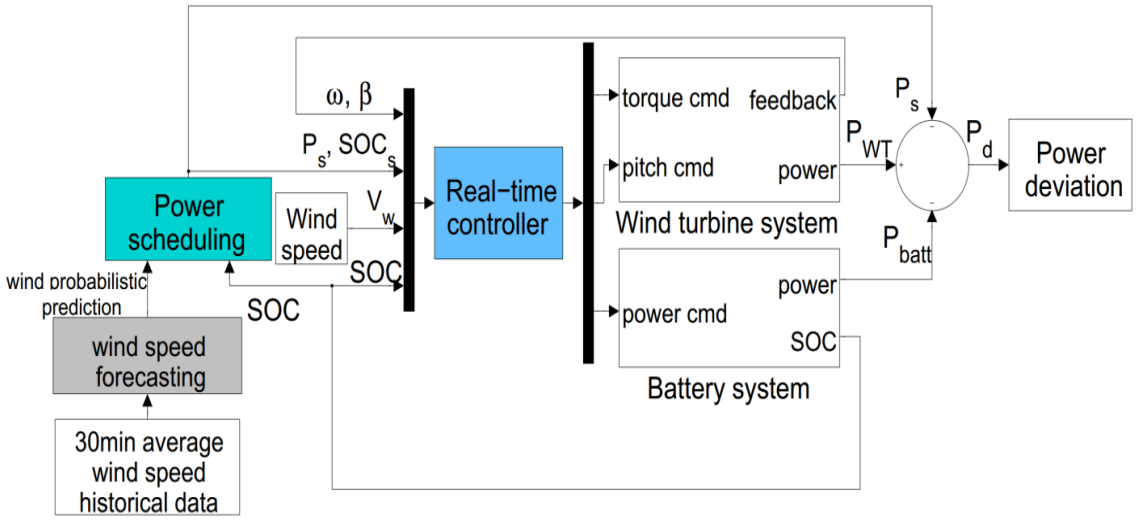

Figure 5.8: Integrated wind turbine and battery system.

The actual wind speed data is obtained from Western Wind Resources Dataset [102]. Seven typical wind sites are listed in Table 5.2, which corresponds to different wind classes. Each data point represents the average wind speed over each 10min. The wind speed prediction is obtained using the normalized and standardized ARMA modeling approach in Section 5.1. For each wind site, a wind speed time series from May 1^{st} to June 30^{th}, 2005 is chosen to train the ARMA model [103]. This trained ARMA model is then used for average wind speed prediction of 30 min-ahead from July 1^{st} to July 2^{nd}, 2005. Figure 5.9 and Figure 5.10 give an example for wind site 102, where

Figure 5.9 shows the historical wind speed and Figure 5.10 compares the actual wind speed with the 30 min-ahead probabilistic wind speed prediction. The predicted wind speed probability distribution will be used in the power scheduling phase.

Wind class	Site ID	Annual mean wind speed (m/s)
1	902	4.92
2	11958	6.35
3	1313	7.25
4	17	7.89
5	102	8.48
6	13717	9.15
7	12796	11.12

Table 5.2: Typical wind sites selected for study.

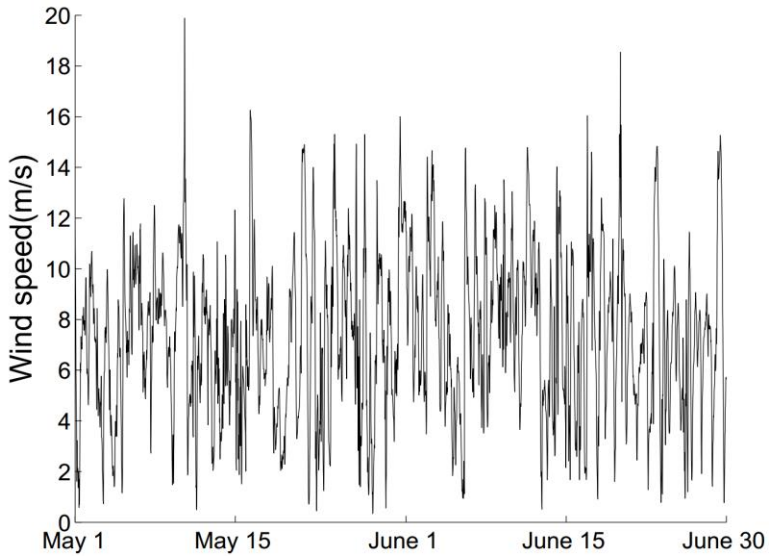

Figure 5.9: Historical wind speed data for Site 102.

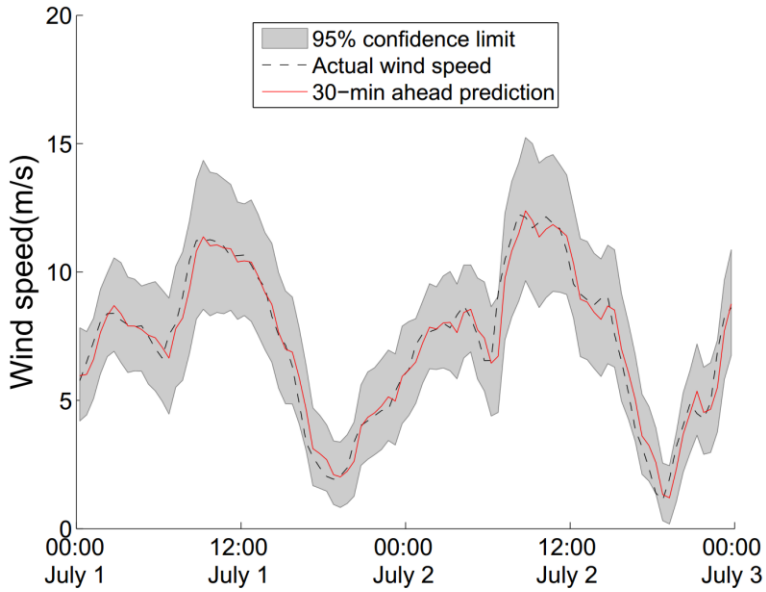

Figure 5.10: 30-min ahead wind speed forecast for Site 102.

5.3 POWER SCHEDULING

In this section, the formulation and disadvantages of traditional multi-step ahead scheduling optimization will be discussed. To overcome the disadvantages associated with traditional approach, a novel efficient one-step ahead optimization scheduling approach will be presented. This approach first determines the desired battery SOC at the end of next dispatch interval by a probabilistic analysis on historical data and then performs a one step ahead scheduling optimization to penalize any deviations from the desired battery SOC.

The cost function of an n-step model predictive optimization can be defined as:

$$J = V(x_n) + \sum_{k=1}^{n} L_k(x_k, u_k), \tag{5.7}$$

where

$$\begin{cases} x = [P_s \quad SOC]^T \\ u = [\Delta P_s \quad \bar{P}_{batt}]^T \\ L_k(x_k, u_k) = -C_1\left(P_{s,k} + \bar{P}_{batt,k}\right) \\ +C_2 \int_a^b \left[P_{s,k} + \bar{P}_{batt,k} - p\left(w_{f,k}\right)\right]^+ f\left(w_{f,k}\right) dw_{f,k} \\ +C_3\left|\Delta P_{s,k}\right| + C_4\left|\bar{P}_{batt,k}/Q\right| \\ V(x_n) = C_5|SOC_n - 0.5| \end{cases} \tag{5.8}$$

subject to:

$$\begin{cases} P_{s,k+1} = P_{s,k} + \Delta P_{s,k} \\ SOC_{k+1} = SOC_k + \bar{P}_{batt,k}\Delta T/Q \\ 0 \le P_s \le P_{s,max} \\ SOC_{min} \le SOC \le SOC_{max} \\ |\Delta P_s| \le \Delta P_{s,max} \\ |\bar{P}_{batt}| \le \bar{P}_{batt.max} \end{cases} \tag{5.9}$$

where P_s and $\bar{P}_{batt}$ are the scheduled power and average battery power, respectively; $[x]^+ = x$ if $x > 0$, $[x]^+ = 0$ if $x <= 0$; $p(w_f)$ refers to the nonlinear mapping from the predicted 30-min average wind speed w_f to the predicted 30-min average turbine power as shown in Figure 5.11. It is obtained by assuming negligible instantaneous wind speed turbulence within each 30 minutes; $f(w_f)$ denotes the probability density function of w_f; ΔT denotes the length of the dispatch interval; C_1, C_2, C_3, C_4 and C_5 are weighting factors that penalize the energy capture, power underproduction, ramp rate, battery charge rate, and the deviation of final SOC from its mid-level, respectively. These weighting factors may vary with varying electricity price and grid trading policies. The energy capture is obtained as the sum of power output to the grid and power stored in the battery. To avoid improper integral with infinite upper or lower limits, the expected value of power underproduction is estimated by integration over the 95% confidence interval of prediction.

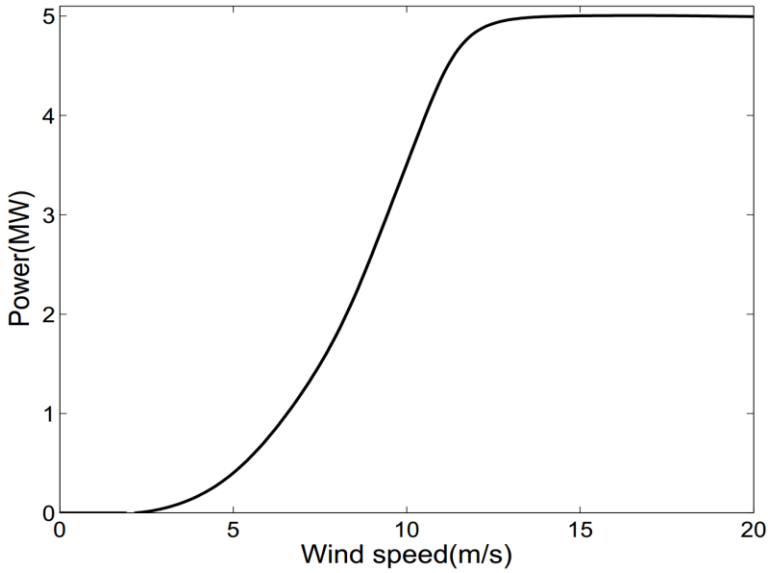

Figure 5.11: 30-min average power versus wind speed curve for the NREL 5 MW wind turbine.

Since the cost function and constraints are nonlinear, optimization over multiple steps is generally computationally expensive. Also, the effectiveness of model predictive optimization heavily relies on the accuracy of wind speed prediction. The confidence intervals of predictions become wider the further we look into the future. Hence, its effectiveness may be undermined by inaccurate long-term multiple step-ahead wind speed predictions. To avoid these issues, the proposed methodology uses a single step-ahead wind speed prediction along with offline analysis of historical wind speed and power data to obtain the scheduled power output. A schematic plot for the proposed power scheduling approach is shown in Figure 5.12. Unlike the traditional model predictive scheduling approaches that perform optimization over multiple dispatch intervals ahead and restores the SOC to its mid-level at the final step, the proposed approach first determines the desired SOC at the end of next dispatch interval by a

probabilistic analysis on historical data and then a one step-ahead scheduling optimization is developed to penalize any deviations from the desired SOC.

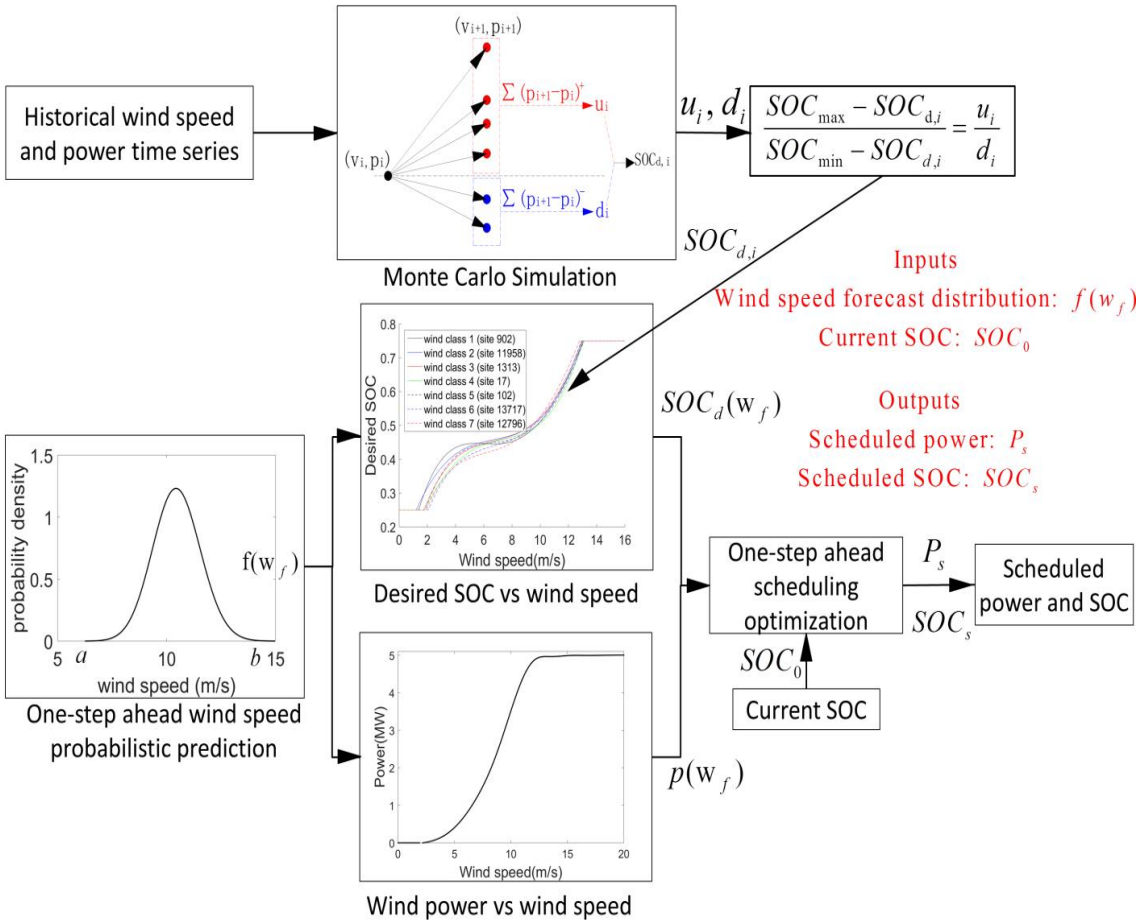

Figure 5.12: Schematic plot of proposed power scheduling approach.

a. Desired Battery SOC

The desired SOC is obtained based on the probability of future wind power variation. If the wind power is likely to increase, then the SOC should be maintained at a lower level so that the battery will have enough capacity to store extra energy and hence smooth the power output. On the other hand, a higher SOC level is preferred when the wind power tends to decrease so that the stored energy could be released to compensate

for the power shortage. In this study, it is found that the 30min average of power variation is highly related to the 30min average of wind speed. Figure 5.13 illustrates how the desired SOC is determined. The arrow directions indicate the wind power going up or down. For the case shown in Figure 5.13, there is a higher probability of power going up than going down. Such probability is identified and quantified through Monte Carlo simulation over one year of historical wind speed data from the wind site. During each 30min interval over the entire year, an average wind speed and generated wind power are recorded in sets W and P, respectively. Let W_k and P_k denote the k^{th} element of W and P, respectively. A power variation that corresponds to W_k is defined as $V_k = P_{k+1} - P_k$. For each wind speed v_i from 0 to 16 m/s with an increment of 0.5 m/s, an average power increase u_i, and decrease d_i, are the sum of all the positive and negative V_k that corresponds to $|W_k - v_i| < 0.25\ m/s$, respectively. Then, the desired SOC for v_i, $SOC_{d,i}$, is calculated as:

$$\frac{SOC_{max} - SOC_{d,i}}{SOC_{\min} - SOC_{d,i}} = \frac{u_i}{d_i} \tag{5.10}$$

The capacities for storing and releasing energy are proportional to the probability of generated wind power increase and decrease, respectively. The desired SOC can be developed as a continuous function of wind speed using all pairs of $(v_i, SOC_{d,i})$. Figure 5.14 shows the mapping from 30min average wind speed to the desired SOC for different wind sites. The similarity among these curves are due to that the probabilities of power increase for low wind speeds are generally high, and vice versa, regardless of wind sites and wind speed profiles.

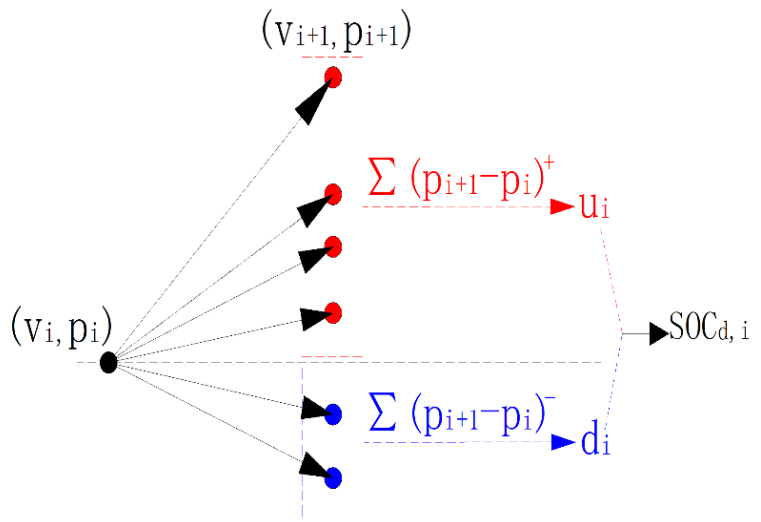

Figure 5.13: Illustration of determining desired SOC.

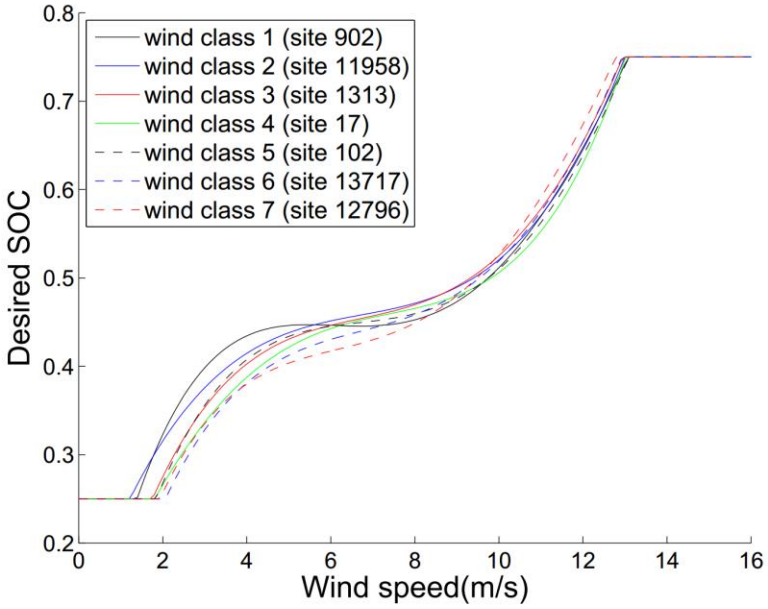

Figure 5.14: Desired SOC versus wind speed curves for different wind sites.

b. One-step Ahead Scheduling

After determining the desired SOC corresponding to each wind speed, a one-step ahead scheduling approach is proposed to optimize the power dispatch. The scheduling approach determines the scheduled power P_s during the next 30min dispatch interval, and the scheduled state of charge SOC_s at the end of the same 30min interval based on the initial SOC_0, and the 30min-ahead probabilistic wind speed prediction w_f. The cost function in (5.7)-(5.8) is modified as a one-step ahead cost function defined by:

$$\begin{aligned} J = &-C_1(P_s + \bar{P}_{batt}) + C_2 \int_a^b \left[P_s + \bar{P}_{batt} - p(w_f)\right]^+ f(w_f) dw_f \\ &+C_3|\Delta P_s| + C_4|\Delta \bar{P}_{batt}/Q| + C_5 \left|\mathrm{SOC_s} - \int_a^b SOC_d(w_f) f(w_f) dw_f\right| \end{aligned} \tag{5.11}$$

subject to (5.9).

where $SOC_d(w_f)$ is the corresponding desired SOC for a wind speed of w_f; C_1, C_2, C_3, C_4 and C_5 are determined based on [104] to be 1, 2, 0.1, 0.2 and 1, respectively. While the first four terms in (5.11) reduce the financial cost during the next dispatch interval, the last term minimizes the deviation from the desired SOC at the end of the same time interval. The proposed power scheduling approach, described by (5.9)-(5.11), determines a scheduled power output and a scheduled SOC for next dispatch interval.

5.4 REAL-TIME CONTROL FOR SCHEDULED POWER TRACKING

In this section, a real-time controller is designed to track the scheduled target determined in the power scheduling phase with improved system performances.

During real-time operation, the instantaneous wind condition varies within each 30 minutes. The BESS needs to be charged or discharged in order to compensate for the wind turbine power fluctuation and track the scheduled power output of the integrated system determined by (5.9)-(5.11). Using a standard wind turbine controller that

maximizes energy capture in below rated-speed region may result in undesirable battery charging or discharging. Furthermore, it may require BESS with a large capacity and charging rate limit to compensate for the varying wind power. To prevent undesirable battery operation and reduce the battery size, thus installation expense, it is necessary to actively control the generated wind power. The proposed real time control system is shown in Figure 5.15. First, a reference power set point is determined by a steady state optimization method considering the trade-off between battery performance optimization and energy capture maximization. Then, an active power controller for wind turbine is applied to track the set point in real time.

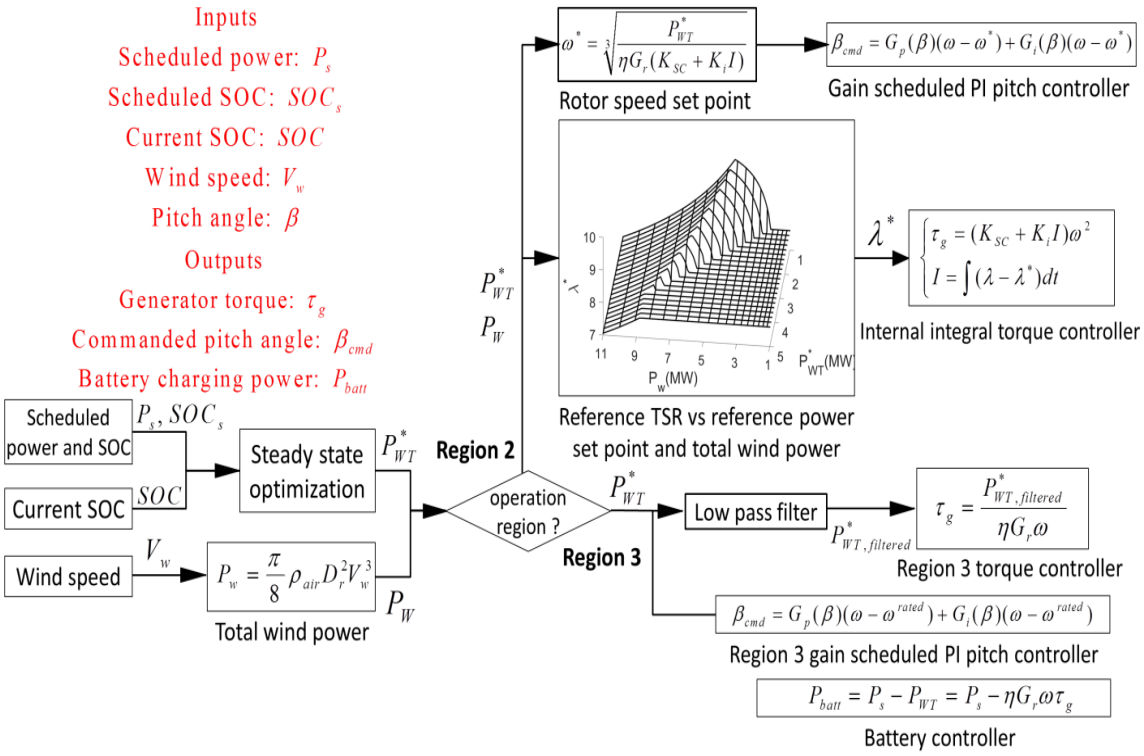

Figure 5.15: Schematic plot of proposed real time controller.

a. Reference Power Set Point for Wind Turbine

An optimal reference power set point for wind turbine is determined by considering the tradeoff between battery performance optimization and energy capture maximization. The battery performance can be evaluated using the following performance index:

$$J_{batt} = \int_{-\infty}^{\infty} k_1 \left(\frac{P_{batt}}{Q}\right)^2 + (1 - k_1)(SOC - SOC_s)^2 dt, \tag{5.12}$$

where k_1 is the weighting factor indicating the tradeoff between mitigating the charging/discharging rate and deviation of the SOC from its scheduled target. Based on the linear battery state space equation described by (5.6), the infinite-time quadratic performance index in (5.12) can be minimized by solving the Algebraic Riccati Equation. Hence, the optimal battery charging power is obtained as:

$$P_{batt}^* = Q\sqrt{\frac{1 - k_1}{k_1}}(SOC_s - SOC). \tag{5.13}$$

Considering the tradeoff between battery performance optimization and wind energy maximization, the reference power set point for wind turbine is determined by minimizing the following steady state performance index:

$$J_{WT} = k_2(P_{WT} - P_{batt}^* - P_s)^2 - (1 - k_2)P_{WT}, \tag{5.14}$$

where the first term penalizes the deviation of the steady state battery power from the value for optimal battery operation. The second term reflects the consideration of energy capture maximization. $k_2$is the weighting factor. By solving the quadratic steady state optimization in (5.14), the reference power set point for wind turbine is derived as:

$$P_{WT}^{*} = Q\sqrt{\frac{1-k_1}{k_1}}(SOC_s - SOC) + P_s + \frac{1-k_2}{2k_2}, \tag{5.15}$$

b. Active Power Controller

After determining the optimal reference power set point, a new active power controller is developed for accurately tracking the set point with improved wind turbine performances.

Firstly, the real-time control design for Region 2 operation is presented. In Region 2, a wind turbine is conventionally controlled to track the maximum power coefficient, C_p^{max}. Hence, the pitch angle is fixed at an optimal value and the generator torque is controlled to track the optimal TSR, λ^{opt}. However, in order to track the reference power set point, P_{WT}^{*} , a wind turbine should track a specific power coefficient, C_p^{*}, instead of the maximum power coefficient, C_p^{max}. C_p^{*} is calculated as:

$$C_p^{*} = \frac{P_{WT}^{*}}{P_w \eta}, \tag{5.16}$$

where η is the electrical efficiency of generator and P_w is the total wind power expressed as:

$$P_w = \frac{\pi}{8}\rho_{air} D_r^2 V_w^3, \tag{5.17}$$

where ρ_{air}, D_r and V_w refer to the air density, rotor diameter and effective wind speed, respectively. When C_p^{*} is larger than C_p^{max}, C_p^{*} is not achievable. In this case, the controller will track the optimal TSR, hence C_p^{max}, as a traditional Region 2 controller does [60]. When C_p^{*} is lower than C_p^{max}, the optimal control corresponds to multiple combinations of TSR and pitch angle. For instance, a contour line representing $C_p^{*} = 0.4$

is shown in Figure 5.16. The turbine may operate at different points on the contour line that correspond to different combinations of TSR and pitch angle.

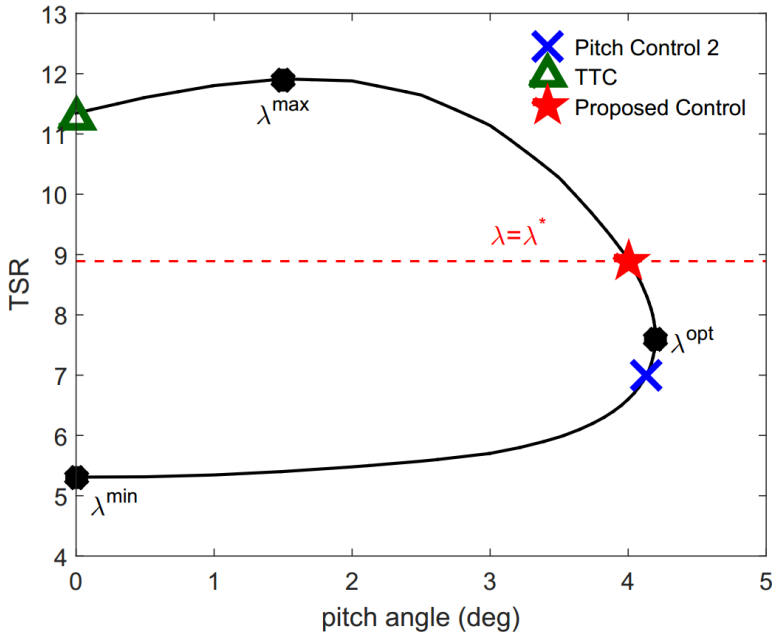

Figure 5.16: A contour line for $C_p^* = 0.4$ and designed operation points for different active power controllers.

Two active power controllers have been developed recently for Region 2 operation, namely, Pitch Control 2 [57] and TTC [59]. Figure 5.16 illustrates the designed operation points on the contour line for Pitch Control 2 and TTC. Pitch Control 2 applies the same generator torque control law as the standard controller [60] and uses a blade pitch controller for reference power set point tracking. As a result, this controller tends to work at a lower-than-optimal TSR with less stored kinetic energy and thus it is less capable of delivering consistent power output in the presence of wind shortage. Also, with a lower TSR, a wind turbine is less likely to reach the rated speed, where active power control is more efficient for constant speed operation. As opposed to Pitch Control

2, TTC fixes the pitch angle at its optimal value and controls the generator torque to operate at a higher TSR with more stored kinetic energy. However, TTC is more likely to switch between Region 2 and Region 3 as the actual wind power is oscillating around the reference power set point. This could lead to significant rotor speed and torque fluctuations. In addition, the torque feedback control gain of TTC is derived based on the C_p contour line from an ideal wind turbine model. In real application, non-uniform wind inflow or turbine structural degradation can cause the C_p contour line to deviate away from its ideal values. As a result, the torque feedback control gain of TTC would be inaccurate which undermines the tracking accuracy of reference power set point.

To determine a good operating region on the C_p contour line, the following factors are considered. A higher operating TSR is good for storing more kinetic energy. An operating TSR close to the optimal TSR is good for mitigating the rotor speed and torque fluctuation associated with switching. The controller of Pitch Control 2 can adjust the operating point to the actual contour line that may deviate from the ideal contour line due to model-plant mismatch. With these considerations, a new active power controller is proposed to drive the wind turbine to operate around a desirable reference TSR through controlling both the generator torque and pitch angle. An internal integral torque controller is adopted as follows [76], [78]:

$$\begin{cases} \tau_g = (K_{SC} + K_i I)\omega^2 \\ I = \int (\lambda - \lambda^*) dt \end{cases}, \tag{5.18}$$

where K_{SC} is the same torque feedback control gain as standard controller [60]; K_i and I denote the internal integral gain and the integral of deviation between the measured TSR, λ and the reference TSR, λ^*, respectively. λ^* is designed to be located between the optimal TSR and the maximum TSR as follows:

$$\lambda^* = c\lambda^{opt} + (1-c)\lambda^{max}, \tag{5.19}$$

where c is a weighting factor. λ^* is upper-bounded to keep the corresponding rotor speed under the rated value. Additionally, λ^* is calculated as a function of the reference power set point P_{WT}^* and total wind power P_w based on C_p contour lines. Its value can be obtained using a look-up table as shown in Figure 5.17. It should be noted that the desirable λ^* can be any point between λ^{opt} and λ^{max} with different weighting factors. Although λ^* may be inaccurate due to modeling error of C_p contour lines, the goal of this controller can be achieved as long as λ^* is between λ^{opt} and λ^{max}.

After the torque controller drives the wind turbine to operate in the desired TSR region, a pitch controller is applied to adjust the operating point to the contour line. The pitch angle is commanded using a gain-scheduled PI controller:

$$\beta = G_p(\beta)(\omega - \omega^*) + G_i(\beta)\int(\omega - \omega^*)dt, \tag{5.20}$$

where $G_p(\beta)$ and $G_i(\beta)$ are the same scheduled proportional and integral gains as in [60]. ω^* is a rotor speed set point that allows the wind turbine to track the reference power set point, and it can be obtained as:

$$\omega^* = \sqrt[3]{\frac{P_{WT}^*}{\eta G_r(K_{SC} + K_i I)}}, \tag{5.21}$$

When the wind turbine operates at ω^*, the following equality always holds,

$$\eta G_r \tau_g \omega^* = \eta G_r(K_{SC} + K_i I)(\omega^*)^3 = P_{WT}^*, \tag{5.22}$$

Therefore, regardless of model-plant mismatch, the generated wind turbine power will be adjusted to the reference power set point by the pitch controller.

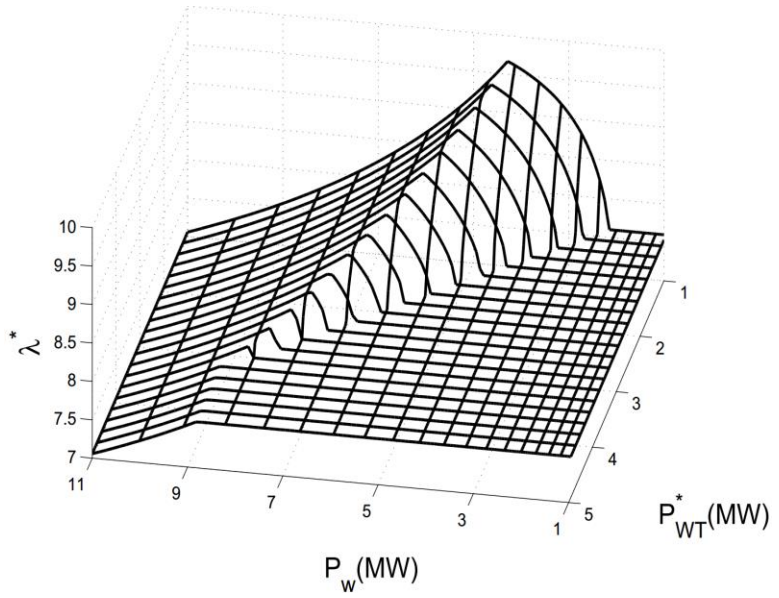

Figure 5.17: Look-up table for reference TSR when $c = 0.7$.

Secondly, a standard gain-scheduled pitch control for Region 3 is applied to maintain the turbine to operate at its rated speed. While applying the pitch control law, to follow the reference power set point, the generator torque is commanded as:

$$\tau_g = \frac{P^*_{WT,filtered}}{\eta G_r \omega}, \tag{5.23}$$

where $P^*_{WT,filtered}$ refers to the low-pass filtered reference power set point. The filtered reference power is used to prevent large torque variation induced by the sudden change of reference power set point. A standard discrete-time recursion equation is used for the filter [105]:

$$\begin{cases} P^*_{WT,filtered} = \alpha P^*_{WT,filtered,-1} + (1-\alpha) P^*_{WT} \\ \alpha = e^{-2\pi \Delta T f_c} \end{cases} \tag{5.24}$$

where α, ΔT, f_c are the low-pass filter coefficient, discrete time step and corner frequency, respectively. $P^*_{WT,filtered,-1}$ refers to the filtered value at previous time step.

Thirdly, for switching between Region 2 and 3, a transition Region 2.5 is implemented that linearly interpolates the generator torque commands for the two regions. In order to smooth the torque variation due to switching, I is set to be $\left(\frac{\tau_g}{\omega^2} - K_{SC}\right)/K_i$ when the turbine operates at the rated speed, and $P^*_{WT,filtered}$ is set to be $\eta\tau_g\omega G_r$ when the turbine operates below rated speed. Also, a linear transition Region 1.5 is defined as a start-up region for wind turbine operation. The generator speed range for each operational region is the same as that of the standard controller [60].

5.5 SIMULATION RESULTS

To demonstrate the effectiveness of the proposed scheduling and real-time control methodology, simulations are conducted in MATLAB/Simulink environment. The resolution of original wind speed data from Western Wind Resources Dataset is 10 minutes, which does not meet the requirement for real-time simulation. Therefore, the NREL Turbsim Code [89] is modified to convert the original data into 0.1 second-resolution wind profiles for each 10 minutes period.

a. Comparison of Power Scheduling Methods

The proposed power scheduling method is compared with the traditional heuristic scheduling and the multiple step-ahead model predictive optimization approach. A heuristic power scheduling method is obtained as [49]:

$$\begin{cases} P_s = 2\dfrac{SOC - SOC_{min}}{SOC_{max} - SOC_{\min}} P_f, \\ |\Delta P_s| \le \Delta P_{s,max} \end{cases} \tag{5.25}$$

where $SOC_{\min}$ and SOC_{max} are the minimum and maximum operational SOC, respectively; P_f denotes the expected value of forecasted wind power for the next dispatch period; $\Delta P_{s,max}$ is the maximum ramp rate allowed between two consecutive

scheduling periods. The heuristic algorithm schedules more power at a higher SOC in order to keep SOC at its mid-level. Unlike the proposed scheduling approach, the heuristic algorithm does not take into account other influential factors including energy waste, ramp rate, battery charging rate and power deviation. Hence, the resulting performance does not optimize the entire integrated system.

Considering the prediction error increases as we look further into the future and the prediction accuracy beyond 10 steps is too low to be used, the look-ahead steps of the traditional model predictive optimization is selected to be 10. Dynamic programming is used for solving the optimization problem defined in (5.7)-(5.9).

In order to solely demonstrate the effectiveness of different scheduling algorithms, the standard controller [60] is adopted for real-time control of wind turbines. It controls the generator torque to be proportional to the square of rotor speed in Region 2 and regulates the rotor speed at rated value using a scheduled PI pitch control in Region 3. The BESS is then used to compensate for the deviation between the scheduled power and generated wind power. The BESS is selected to have a capacity of 1MWh (20% of the hourly rated energy output of wind turbine) with a charging rate limit of 1C.

A detailed performance comparison among different scheduling approaches is shown in Figure 5.18. A wind speed profile from site 102, covering all operating regions of the wind turbine, is shown in the top subplot of Figure 5.18. Compared to the results with heuristic power scheduling, the amount of scheduled power output is increased by 1.5% using the proposed scheduling method. The average ramp rate of scheduled power output is decreased by 58% while the power deviation is also minimized. The power overproduction and underproduction are reduced by 79% and 37%, respectively. Moreover, the average charging rate of battery drops by 20%, resulting in extended battery health. Therefore, the proposed scheduling method outperforms the heuristic

approach with respect to energy capture, output power quality as well as battery performance.

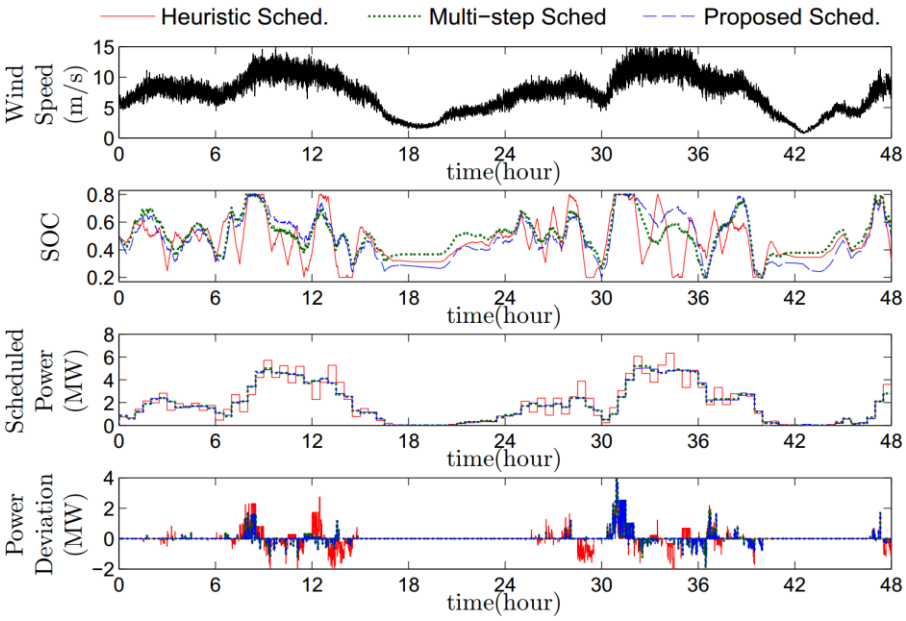

Figure 5.18: Performance comparison between various scheduling approaches with a 1 MWh BESS and standard real-time controller.

The traditional model predictive optimization shows comparable results as the proposed scheduling approach. Compared to the proposed scheduling approach, it slightly lowers the average battery charging rate by 3.8%. However, it results in a 0.4% lower energy capture, 3.5% higher ramp rate as well as a 1.4% and 2.1% higher power overproduction and underproduction. Additionally, it takes much longer computational time compared to the proposed scheduling approach. Therefore, the proposed approach reduces computational effort with comparable performance as the traditional model predictive optimization.

b. Comparison of Real-time Wind Turbine Active Power Controllers

In order for the integrated system to track the scheduled power output under instantaneous varying wind speed within each dispatch interval, an active power controller was developed for wind turbines to track a reference power set point. Simulations were conducted to compare the performances of the proposed controller with two popular active power controllers, namely, Pitch Control 2 [57] and TTC [59]. The Pitch Control 2 is a pitch-based controller for reference power set point tracking. It applies the same torque control as the standard controller. As opposed to Pitch Control 2, TTC fixes the pitch angle and controls generator torque during the below-rated speed operation. While the generator torque of TTC is also proportional to the square of generator speed, a different torque feedback control gain is adopted to track a higher-than-optimal tip speed ratio (TSR). Figure 5.19 shows comparisons of the rotor speed, generator torque, blade pitch angle, wind turbine power and rotor torque for various active power controllers. A wind profile of 10 minutes from site 102 is used. Also, the blade and tower bending moments with different controllers are shown in Figure 5.20, where the subplots compare the tower side-to-side moment (TSSM), tower fore-aft moment (TFAM), blade edge-wise moment (BEM) and blade flap-wise moment (BFM), respectively.

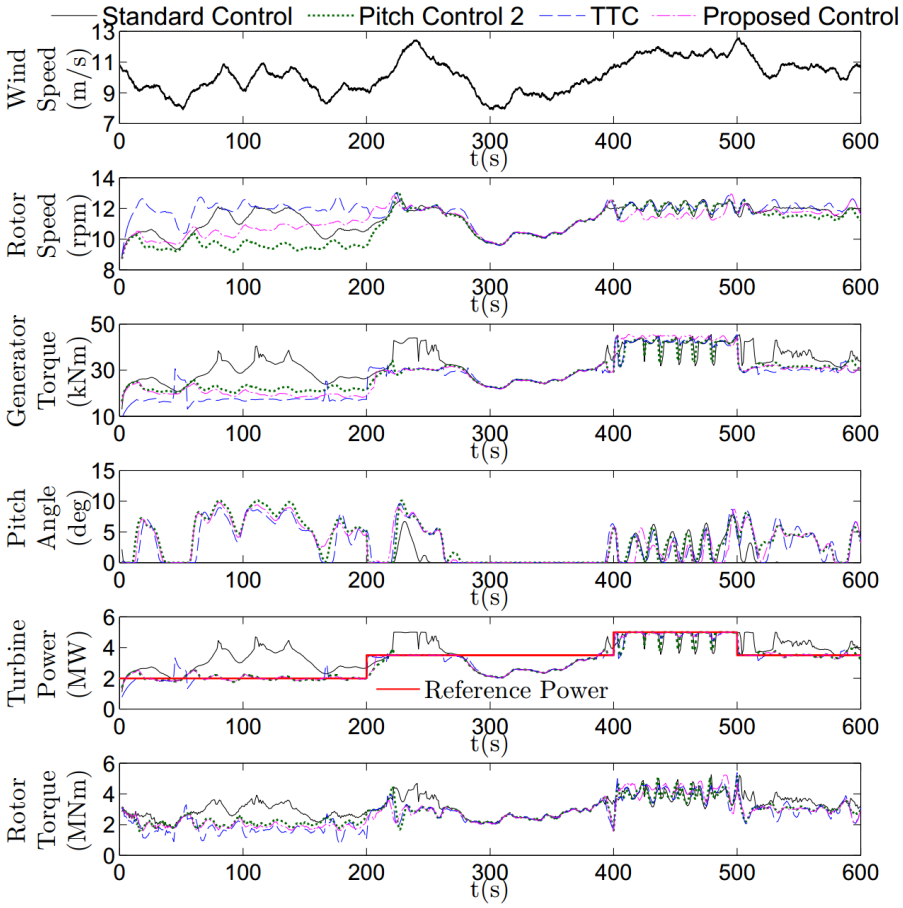

Figure 5.19: Performance comparison of active power controllers for reference power set point tracking.

As shown in Figure 5.19, from 300s to 400s, the three active power controllers perform similarly as the standard controller when the reference power set point is higher than the available wind power. Once the reference power set point is lower than the available wind power, all three active power controllers are able to track the set point. However, as shown from 400s to 500s, Pitch Control 2 suffers from significant torque fluctuations when the set point is close to the rated value. Also, Pitch Control 2 stores less kinetic energy in the rotor and responds slower to the variation of set point compared to the other two active power controllers. TTC generally tracks the reference power set

point well. However, as shown at the 50s, when the available wind power approaches the set point, the rotor speed, generator torque and rotor torque would experience a significant oscillation, negatively impacting the fatigue loads on the turbine structure. Compared to Pitch Control 2 and TTC, the proposed controller changes the rotor speed, generator torque and rotor torque less aggressively, hence reducing the fatigue loads acting on the turbine structure.

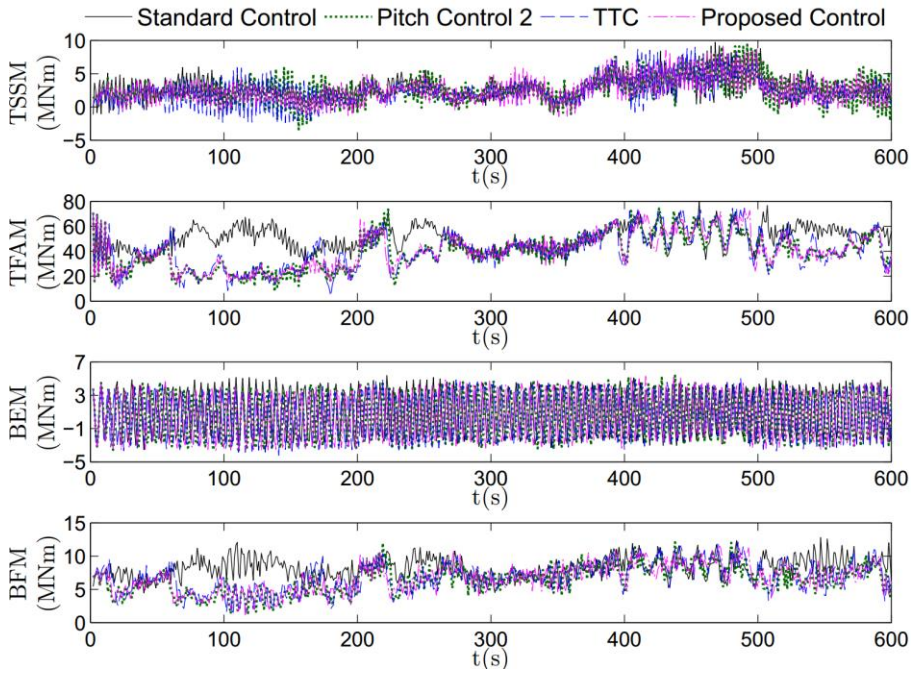

Figure 5.20: Fatigue loads comparison of active power controllers for reference power set point tracking.

The damage equivalent loads (DEL) induced on the turbine components can be calculated using the NREL Mlife Code [95] and used to represent the effect of such fatigue loads on the useful life of a wind turbine. The DELs under a standard controller [60] is considered as the baseline. A quantitative comparison of the three controllers with respect to the DELs is shown in Figure 5.21. Among the three active power controllers, the proposed

controller experiences the least tower and blade DELs due to its smoothed control behavior with less torque and rotor speed variations.

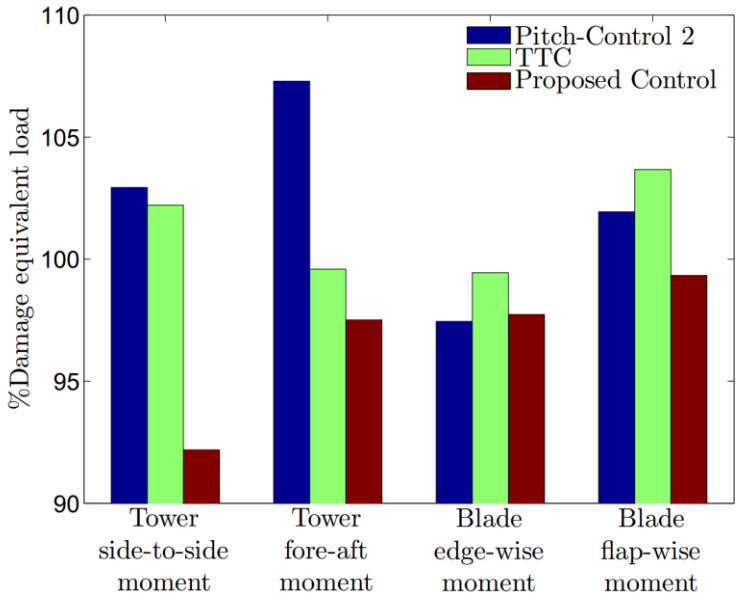

Figure 5.21: Induced damage equivalent loads (DEL) with various active power controllers compared to the baseline where the baseline DEL is obtained using standard controller.

c. Effect of the Combined Scheduling Approach and Real-Time Controller

The performances of combining the above scheduling approaches and real-time controllers are compared in Figure 5.22. There are three combinations, namely, heuristic scheduling and standard real-time control, proposed scheduling and standard real-time control, and proposed scheduling and proposed real-time control. The battery system and wind profile used in previous section are adopted here.

As shown in Figure 5.22, in addition to the improvements generated by the proposed scheduling approach over the heuristic approach, combining the proposed real-time controller and scheduling further reduces the power deviations. Our calculation indicates reductions of power overproduction and underproduction by 98% and 18%,

respectively. At the same time, the average generator torque changing rate and battery charge rate decrease by 46% and 7%, respectively. The above improvements with respect to reducing wind turbine torque variation, battery charge rate and power deviation are at the expense of a slight decrease of overall system energy output, which is roughly 0.6% in this case. Thus, the benefit from implementing the proposed controller is much more significant compared to the marginal energy sacrifice.

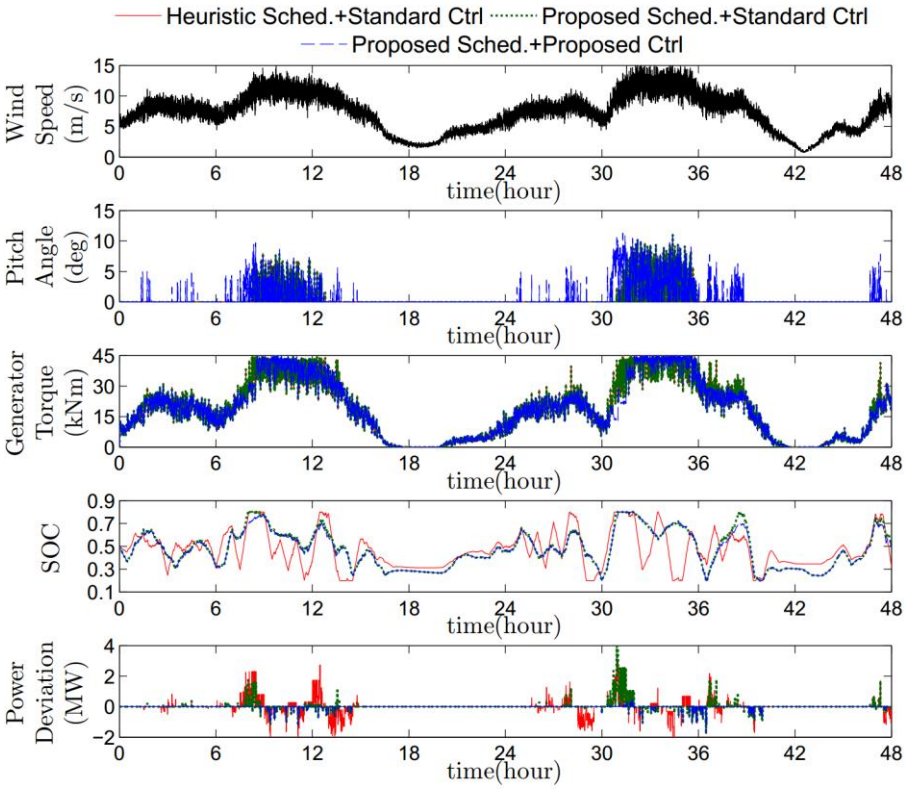

Figure 5.22: Performance comparison among various scheduling approaches and real-time controllers with a 1MWh BESS.

d. Generalized Results for Various Battery Sizes and Wind Sites

To evaluate the effectiveness of proposed methodology under different conditions, simulations were conducted using wind profiles from different wind sites and

batteries of different capacities. Seven wind sites corresponding to different wind classes were chosen in Section III. The selected battery sizes are 0.5MWh, 1MWh, 2MWh, 3MWh and 5MWh, which correspond to 10%, 20%, 40%, 60% and 100% of the wind turbine nameplate capacities, respectively. The performance with the heuristic scheduling method, the standard real-time controller and a 0.5MWh battery is considered as the baseline.

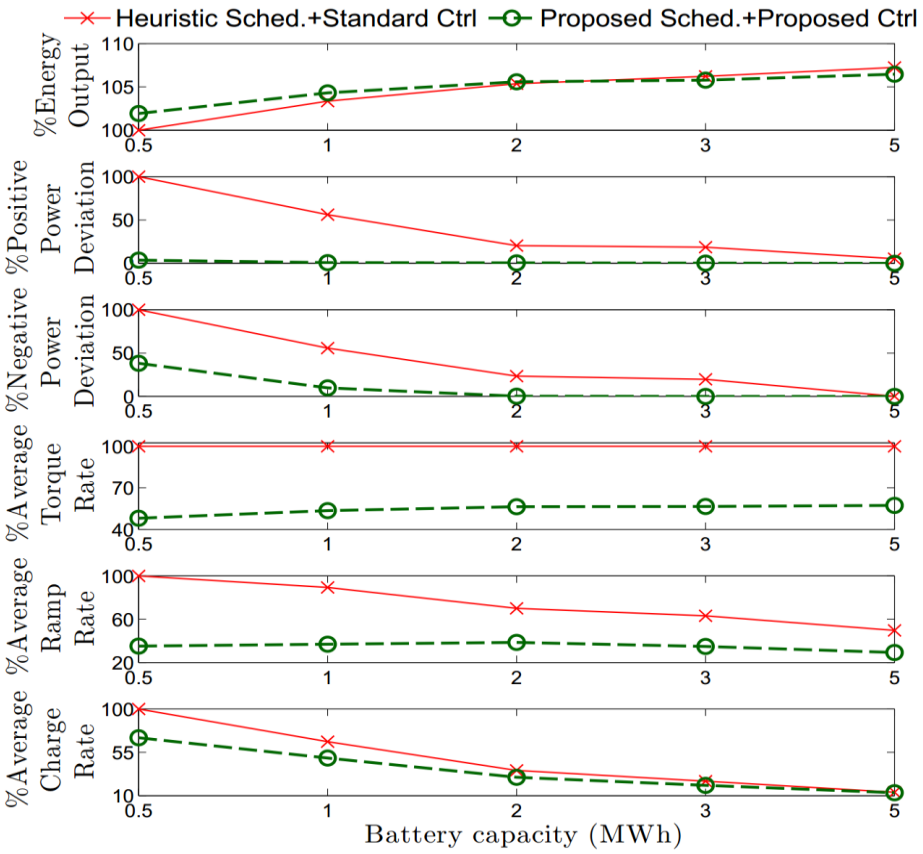

Figure 5.23: Generalized results with various scheduling approaches, real-time controllers and battery capacities compared to the baseline, where the baseline performance is obtained using heuristic scheduling method, the standard real-time controller and a 0.5MWh battery.

Figure 5.23 shows the performances of different combinations of scheduling approaches, real-time controllers and battery sizes are compared to the baseline with respect to the energy output, power deviation, generator torque rate, ramp rate and average battery charge rate. The average performances for 7 wind sites are considered. It can be seen that the proposed scheduling approach and the real-time controller outperforms the heuristic scheduling and standard real-time control in all aspects that include maximizing energy output, mitigating power deviation, ramp rate control, lowering turbine torque rate, and reducing average battery charge rate at the expense of a marginal drop of energy output. It is worth noting that the advantage of the proposed methodology is more obvious with batteries of smaller capacities. Therefore, the proposed methodology also has a benefit for minimizing battery sizes.

5.6 SUMMARY

A new power scheduling and real-time control approach has been proposed to improve the performance of an integrated wind turbine and battery system. A wind speed forecast with statistical significance has been integrated into the power scheduling approach to determine the scheduled power output of the entire system during the future 30 minutes interval and the scheduled battery SOC at the end of the same time interval. By introducing a desired SOC as a function of wind speed, the power scheduling approach performs optimization only for one step ahead. It reduces the computational expense and avoids using unreliable multiple-step ahead wind speed forecasts. Based on the scheduled power output and battery SOC, a reference power set point for wind turbine is determined by a steady state optimization considering both the wind turbine and battery performances. A new active power controller for wind turbine is then presented to track the reference power set point with smoothed torque and rotor speed

variations. Simulation results show that implementing the proposed methodology significantly improves the performances of the integrated wind turbine and battery system over conventional control design with respect to maximizing energy output, mitigating power deviation from the scheduled target, limiting ramp rate, minimizing battery charging rate and reducing fatigue loads. Various wind profiles and battery sizes are also considered to demonstrate the effectiveness of the proposed algorithms under broad applications. Additionally, the proposed methodology shows more significant improvements with battery system of smaller capacity. This finding will lead to potential reduction of battery capacity, thus the overall cost of wind energy. In our future work, a more realistic nonlinear battery model will be used to better represent battery efficiency and degradation behaviors. Also, varying energy price, battery installation cost and grid connections will be studied for more comprehensive analysis.

Chapter 6: *Wind Turbine Participation in Primary Frequency Control*

Traditionally, a wind turbine is controlled to maximize wind energy capture. As a result, the generated electrical power varies under volatile wind speeds, and it is a disturbance or negative load to the grid. Hence, the burden of frequency regulation on conventional power units increases as wind energy penetration increases. To resolve this issue, control methodologies that enable a wind turbine to support grid frequency are in high demand. In this chapter, wind turbine participation in primary frequency control is discussed. The wind turbine is controlled in conjunction with a diesel generator that implements droop control in a microgrid. Thanks to the fast response of power electronics, the wind turbine power output can be rapidly changed following a grid frequency deviation event. This means that the combined power output from the wind turbine and the diesel generator can provide immediate and consistent frequency support to the grid. The immediate injection or absorption of wind turbine power is achieved by slowing down or accelerating the turbine rotor. A novel generator torque controller is proposed for quickly tracking the commanded power output without causing turbine instability such as a complete shut-down or over-speeding. At the same time, it also guarantees maximizing energy capture during normal operation of a wind turbine when the grid frequency is close to its nominal value. A $\mathcal{H}_2$ gain-scheduled pitch controller is extended for regulating speed and tracking the commanded power during rated speed operation. Simulation results show that fast power injection or absorption from wind turbine enhances the grid frequency response by reducing the frequency deviation following a power imbalance event.

Section 6.1 introduces a microgrid model with wind turbine. Conventional droop control for primary frequency control is discussed in Section 6.2. Subsequently, a wind

turbine control strategy for frequency regulation is presented in Section 6.3. The effectiveness of the proposed control design is demonstrated with simulations in Section 6.4. Section 6.5 summarizes the contributions of this work.

6.1 Modeling of a Microgrid with Wind Turbine

In this study, a microgrid with a small-scale interconnection of distributed energy resources (DERs) and loads is considered. Microgrids can either operate in grid-connected mode, where they act as aggregate sources or sinks that respond to signals from the main grid, or in the islanded mode, where they operate independently of the main grid [106]. Compared to a large-scale grid, a microgrid is more sensitive to any given input or disturbance. This is particularly problematic for the incorporation of intermittent renewable DERs which may introduce detrimental swings in power quality. This issue is more pronounced for islanded microgrids in which distributed generators are entirely responsible for supplying the requisite power, without balancing inputs from the main grid. This study is focused on an islanded microgrid with wind energy generation as shown in Figure 6.1.

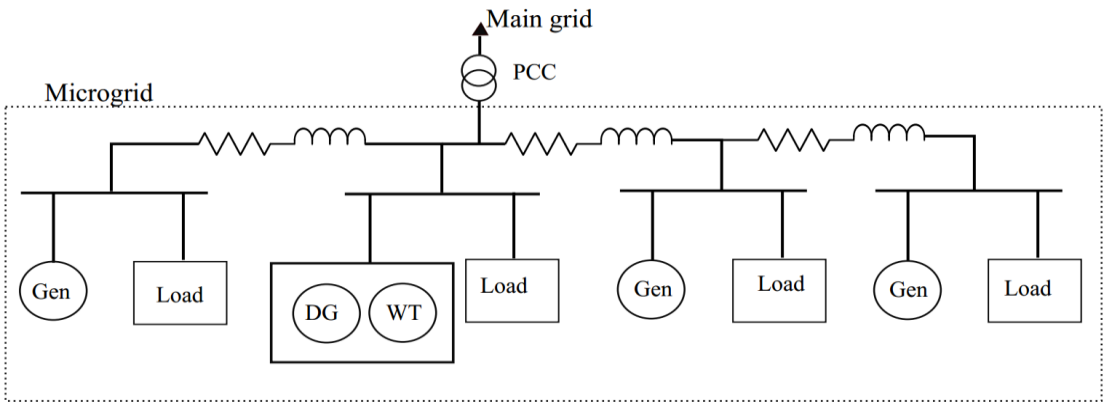

Figure 6.1: Illustration of an islanded microgrid with distributed generators, loads and wind energy.

The system can be treated as an interconnection of 4 subsystems, with each of the subsystems consisting of a distributed generator, a local RLC load, and a power line connecting to the adjacent subsystem. The second subsystem is different from the other subsystems in that it also contains a wind turbine generator. Figure 6.2 demonstrates the detailed structure of subsystem 2 with a wind turbine generator, diesel generator, static and dynamic loads.

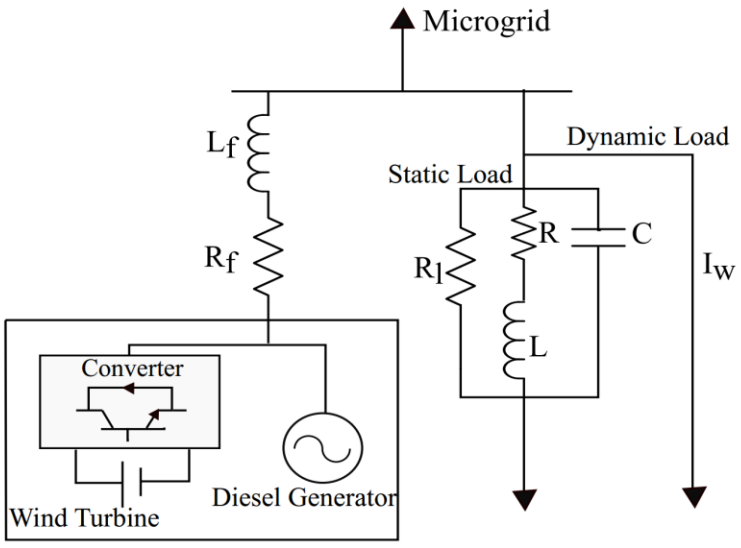

Figure 6.2: Structure of the second subsystem with wind turbine, diesel generator, static and dynamic loads.

An NREL 1.5 MW WindPact turbine [83] is considered in this study. Its modeling parameters are detailed in Table 6.1. The corresponding C_p and C_t characteristic surfaces are obtained using the WT_Perf program [91] developed by NREL for performance predictions of wind turbines based on the blade element momentum theory. The pentagram on the C_p surface shows the simulation-derived optimal operating point where the optimal TSR $\lambda^{opt} = 7.5$, the optimal pitch angle $\beta^{opt} = 2.8°$ and the corresponding optimal power coefficient $C_p^{opt} = 0.4928$. The wind turbine is coupled

with a doubly fed induction generator (DFIG), which allows variable-speed operation of a wind turbine. The stator winding is connected directly to the grid while the rotor winding is connected to a back-to-back voltage source converter. The diesel generator in subsystem 2 and the generators in subsystems 1, 3, 4 have the same full capacity of 8 MW.

Parameter	Magnitude
Generator rated power	1.5 MW
Rotor diameter	70 m
Hub height	84.2876 m
Gear ratio	87.965
Rotor inertia	2.9624×10^{6} kg · m^2
Generator inertia	53.036 kg · m^2
Drivetrain inertia	3.3728×10^{6} kg · m^2
Air density	1.225 kg/m^3
Tower equivalent mass	9.89×10^{4} kg
Tower equivalent damping	6605 N · s/m
Tower equivalent stiffness	6.439×10^{5} N/m
Optimal tip speed ratio	7.5
Optimal blade pitch angle	2.8°
Maximum power coefficient	0.4928
Cut-in wind speed	3 m/s
Cut-out wind speed	27.5 m/s
Rated wind speed	11.3 m/s

Table 6.1: NREL 1.5 MW WindPact turbine model parameters.

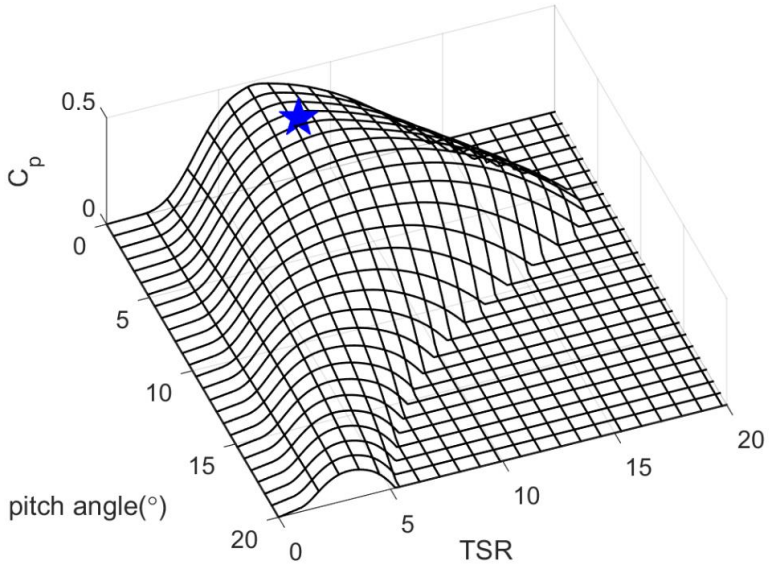

Figure 6.3: Power coefficient versus TSR and blade pitch angle for an NREL 1.5 MW WindPact turbine.

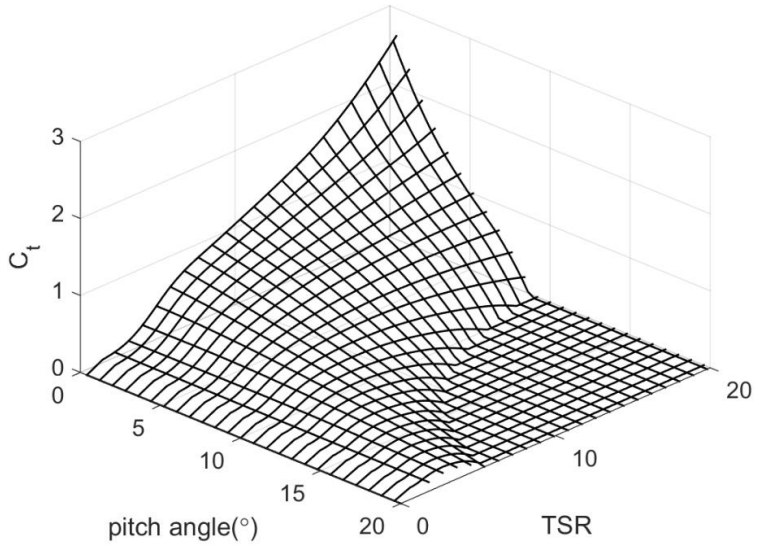

Figure 6.4: Thrust coefficient versus TSR and blade pitch angle for an NREL 1.5 MW WindPact turbine.

The frequency regulation of a microgrid can be classified as primary, secondary and tertiary control with different relevant timescales [107]. The focus of this paper is on primary frequency control, which is aimed at responding quickly to the system disturbances and maintaining grid stability. While the associated voltage stability problem must also be addressed, the intention of this work is to demonstrate the effectiveness of wind turbine active power control on the grid frequency regulation. The frequency stability of power systems can be degraded by power imbalances between power generation and demand. The dynamics of grid frequency can be determined by the following transfer function [74]:

$$\Delta f(s) = \frac{1}{2H_{sys}s + D_{sys}}\left(\sum_{k=1}^{n}\left(\Delta \mathrm{P}_{\mathrm{m,k}}(s) - \Delta P_{L,k}(s)\right) + \Delta \mathrm{P}_{\mathrm{WT}}(s)\right), \tag{6.1}$$

where Δf, $\Delta \mathrm{P}_{\mathrm{m}}$, ΔP_L and ΔP_{WT} refer to the deviations of the grid frequency, mechanical power of the conventional generator, load and wind turbine power from their nominal values. n is the number of subsystems with distributed energy resource and loads. H_{sys} and D_{sys} are the system inertia and damping, respectively. H_{sys} is determined by the total rotational inertia in the system while D_{sys} is influenced by the frequency-sensitive load change. For traditional generators, the mechanical power response can be described by a first-order lag transfer function:

$$\Delta P_m = \frac{1}{\tau_{gen}s + 1}\Delta \mathrm{P}_{\mathrm{m,cmd}}, \tag{6.2}$$

where τ_{gen} denotes the time constant of the generator. In this study, T_{gen} is assumed to be 4 seconds for all conventional generators (including the diesel generator). In contrast, wind turbine power can be ramped up quickly with converters. The power output of a

wind turbine can be adjusted by controlling the electromagnetic torque, which is directly dependent on the quadrature component of the rotor current [108]:

$$T_g = -\frac{L_m e_t}{L_s + L_m} i_{qr}, \tag{6.3}$$

where L_m, L_s and e_t are the magnetizing inductance, stator leakage inductance and the terminal voltage of DFIG, respectively. i_{qr} represents the quadrature component of the rotor current in $d-q$ frame, which can be adjusted to its reference value with a Proportional-Integral (PI) controller:

$$V_{qr}(s) = \left(K_{pq} + \frac{K_{iq}}{s}\right)\left(i_{qr,ref}(s) - i_{qr}(s)\right), \tag{6.4}$$

where K_{pq} and K_{iq} are the proportional and integral gains of PI controller. V_{qr} is the quadrature component of controllable rotor voltage. With the fast power electronics, the wind turbine can provide rapid power injection to stabilize the system frequency following a power imbalance. As this power injection can last just for a few seconds, conventional generators would eventually take care of the demand shift by changing their power generation to compensate for the power imbalance [109].

6.2 DROOP CONTROL

Droop control is the conventional control method suggested for primary frequency regulation due to its convenient implementation. This controller only requires local frequency and voltage measurements for adjusting the mechanical power of a generator. With minimal sensing data and grid topology, it can facilitate power sharing between generators. With only one tunable parameter of droop gain, this controller can be easily adjusted for different generators. While droop control can be used for both

frequency and voltage regulation, this study is focused on the former. By droop control, the commanded mechanical power of a generator is obtained as:

$$\Delta P_{m,cmd} = \delta_d \frac{\Delta f}{f_n} P_{rated}, \tag{6.5}$$

where

$$\begin{aligned} \Delta P_{m,cmd} &= P_{m,cmd} - P_{m,n} \\ \Delta f &= f_n - f \end{aligned}, \tag{6.6}$$

where $P_{rated}, f_n, P_{m,n}$ are the rated power of generator, nominal grid frequency and nominal power output of the generator, respectively. δ_d refers to the droop percentage, which is recommended to be 3%-5% [110]. Due to the slow response of conventional generators, the grid frequency may experience large deviations from its nominal value.

6.3 WIND TURBINE CONTROL STRATEGY FOR FREQUENCY REGULATION

In this section, a wind turbine control strategy is proposed to collaborate with a diesel generator for primary frequency control. Following a power imbalance event, the power of diesel generator changes to meet its droop controlled value. To rapidly provide power during the transient response of the diesel generator, the commanded wind turbine power output is set to:

$$P_{cmd} = \Delta P_{DG,cmd} - \Delta P_{DG} + P_{WT,n}, \tag{6.7}$$

where $\Delta P_{DG,cmd}, \Delta P_{DG}$ refer to the commanded power deviation and actual power deviation of the diesel generator. $P_{WT,n}$ is the nominal power output of the wind turbine. To quickly achieve the commanded power output without causing wind turbine instability, a new wind turbine control strategy is proposed.

During the below-rated speed operation of a wind turbine, the blade pitch angle is fixed at its optimal value. The generator torque control law is designed as:

$$T_{g,cmd} = \begin{cases} T_{energy} & |\Delta f| \le \Delta f_1 \\ \dfrac{|\Delta f| - \Delta f_1}{\Delta f_2 - \Delta f_1} T_{grid} + \dfrac{\Delta f_2 - |\Delta f|}{\Delta f_2 - \Delta f_1} T_{energy} & \Delta f_1 < |\Delta f| < \Delta f_2, \\ T_{grid} & |\Delta f| \ge \Delta f_2 \end{cases} \tag{6.8}$$

where Δf_1 and Δf_2 are the lower and upper thresholds of frequency deviation. With a frequency deviation below Δf_1, generator torque control law T_{energy} for energy maximization or deloaded power tracking is adopted. This guarantees that the wind energy capture is optimized during normal operation of a wind turbine when the grid frequency is around its nominal value. The energy optimized generator torque control law is as follows:

$$T_{energy} = \begin{cases} K_{stc}\omega^2 & \omega \le \sqrt[3]{P_{WT,n}/(G_r K_{stc})} \\ \dfrac{P_{WT,n}}{G_r \omega} & \text{else} \end{cases}. \tag{6.9}$$

The above energy optimized control law guarantees wind turbine convergence to optimal power point if the nominal wind turbine power output is equal to or higher than the available wind power. If the nominal wind turbine power output is lower than the available wind power, the former will be tracked. When the frequency deviation is larger than Δf_2, a frequency supporting generator torque control law is used instead:

$$T_{grid} = \begin{cases} K_{stc}\omega^2 & \omega \le \omega^* \\ \dfrac{\omega - \omega^*}{\omega^{opt} - \omega^*} \dfrac{P_{cmd}}{G_r \omega} + \dfrac{\omega^{opt} - \omega}{\omega^{opt} - \omega^*} K_{stc}\omega^2 & \omega^* < \omega < \omega^{\mathrm{opt}} \\ \dfrac{P_{cmd}}{G_r \omega} & \omega \ge \omega^{\mathrm{opt}} \end{cases}, \tag{6.10}$$

where ω^{opt} refers to the optimal rotor speed given a specific wind speed:

$$\omega^{opt} = \frac{2V_w\lambda^{opt}}{D_r}, \tag{6.11}$$

where V_w, D_r are the wind speed and rotor diameter, respectively. λ^{opt} denotes the optimal tip speed ratio, which is a fix value for a given wind turbine. When the rotor speed is above ω_{opt}, wind energy capture is increased by slowing down the turbine rotor; during this phase, the wind turbine power output is exactly the commanded value. The input wind power to the turbine system gradually approaches the output electrical power as the turbine speed decreases. This stabilizes the turbine speed. When the rotor speed falls below ω_{opt}, the captured wind power starts to drop. The output electrical energy must be reduced accordingly to avoid wind turbine instability, which itself can cause another frequency dip. In this study, $\omega^* = \min(0.9\omega^{opt}, 0.6\omega_{rated})$ is used as a threshold. When the turbine rotor speed falls below this threshold, generator torque control law for maximizing energy capture is used to restore the turbine speed.

Using the frequency supporting generator torque control law as in (6.10)-(6.11), there can be three different wind turbine operation scenarios for different commanded wind turbine power output, P_{cmd}. When $P_{cmd} > P_{wind}(\omega_{opt})$, wind turbine operates on the segments A-B-C-D as shown in Figure 6.5. The wind turbine can only temporarily produce the commanded power when operating on segment A-B. Once the wind turbine rotor speed falls below ω_{opt}, the turbine will eventually operate around an equilibrium point with a turbine rotor speed lower than ω_{opt} if wind speed and P_{cmd} remain unchanged. At this equilibrium point, the power output of wind turbine is less than the commanded value. When $P_{wind}(\omega_{opt}) > P_{cmd} > P_{wind}(\omega_{rated})$, the wind turbine will operate on the segments A-B-C-D as shown in Figure 6.6. The equilibrium point of turbine operation has a rotor speed between ω_{opt} and ω_{rated}. Hence, the wind turbine is

capable of tracking the commanded power output with only generator torque control while blade pitch angle is fixed at its optimal value. When $P_{cmd} < P_{wind}(\omega_{rated})$, wind turbine will operate on the segments A-B-C-D as shown in Figure 6.7. The wind turbine will eventually operate around the rated speed with the commanded power output. In this scenario, blade pitch controller is required for speed regulation and prevent over-speeding.

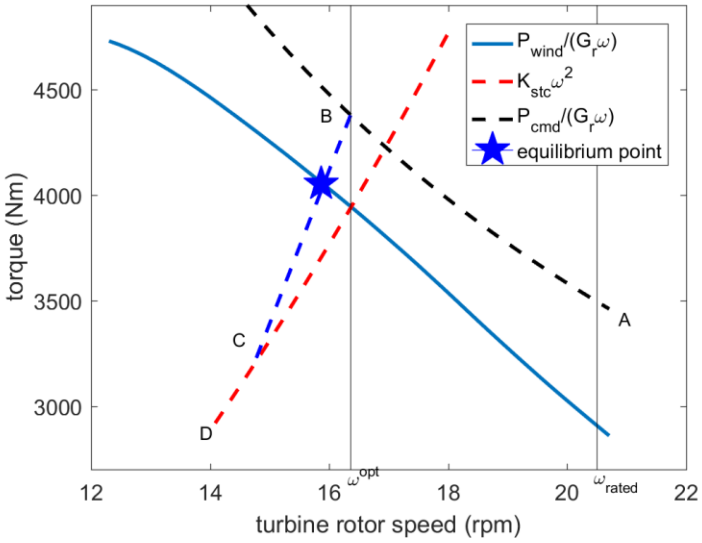

Figure 6.5: Illustration of grid supporting generator torque controller when $P_{cmd} \geq P_{wind}(\omega_{opt})$.

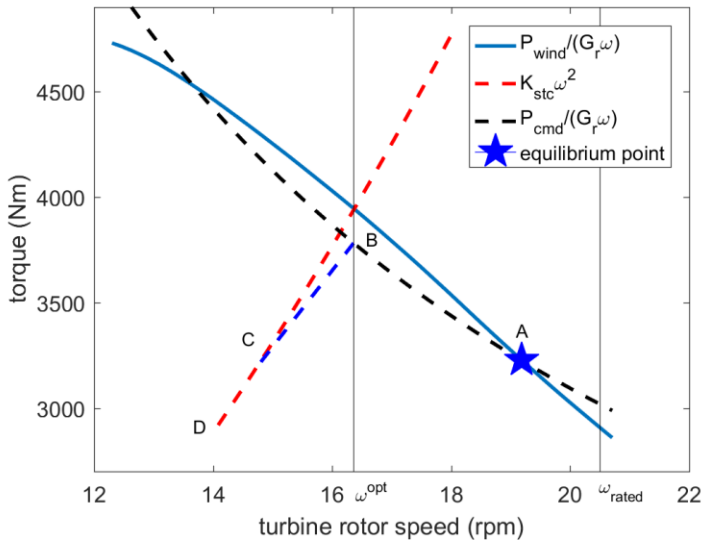

Figure 6.6: Illustration of grid supporting generator torque controller when $P_{wind}(\omega_{rated}) < P_{cmd} < P_{wind}(\omega_{opt})$.

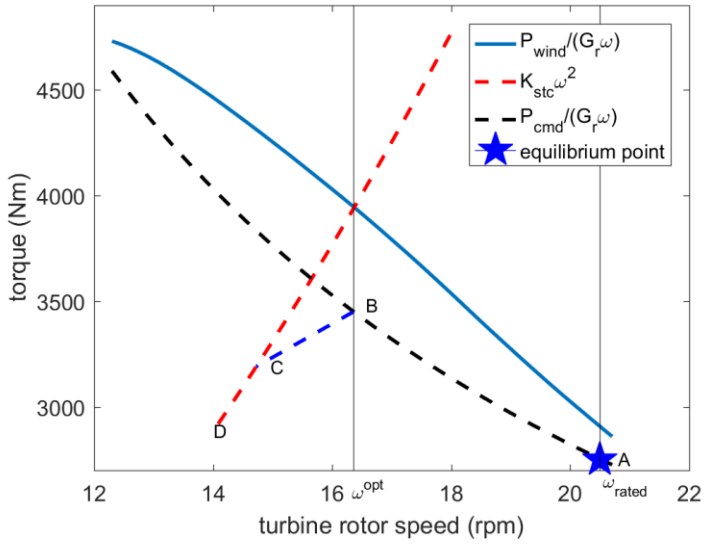

Figure 6.7: Illustration of grid supporting generator torque controller when $P_{cmd} \leq P_{wind}(\omega_{rated})$.

A blade pitch controller for tracking P_{cmd} during rated speed operation is extended from the $\boldsymbol{\mathcal{H}_2}$ gain-scheduled pitch controller described in Section 4.3. Following similar derivations from (4.6)-(4.15), a new $\boldsymbol{\mathcal{H}_2}$ gain-scheduled pitch controller can be obtained as:

$$\beta_{cmd} = K_p(\beta, P_{cmd})\Delta\omega + K_i(\beta, P_{cmd})\int \Delta\omega dt \tag{6.12}$$

where the proportional and integral gains K_p and K_i can be expressed as:

$$\begin{cases} K_p(\beta, P_{cmd}) = (k_1 + \dfrac{P_{cmd}}{\omega_{rated}^2 J_d})J_d/(-\dfrac{\partial T_{aero}}{\partial \beta}) \\ K_i(\beta, P_{cmd}) = k_2 J_d/(-\dfrac{\partial T_{aero}}{\partial \beta}) \end{cases} \tag{6.13}$$

where k_1 and k_2 are calculated by solving the following nonlinear equations:

$$\begin{cases} [9k_1^2 - 2\dfrac{P_{cmd}}{\omega_{rated}^2 J_d}k_1 + (\dfrac{P_{cmd}}{\omega_{rated}^2 J_d})^2](k_1 + \dfrac{P_{cmd}}{\omega_{rated}^2 J_d})^2 = 4W(\dfrac{\partial T_{aero}}{\partial \beta})^2/J_d^2 \\ k_2 = \dfrac{1}{2}[k_1^2 - (\dfrac{P_{cmd}}{\omega_{rated}^2 J_d})^2] \end{cases} \tag{6.14}$$

Different from the control design in Section 4.3, the proportional and integral gains of this controller are determined by both the blade pitch angle β and the commanded power output P_{cmd}. Both of these parameters are very easy to measure during real time operation. As shown in Figure 6.8 and Figure 6.9, the proportional and integral gains for the commanded power tracking pitch controller of NREL 1.5 MW WindPact turbine are obtained by the $\boldsymbol{\mathcal{H}_2}$ norm minimization technique.

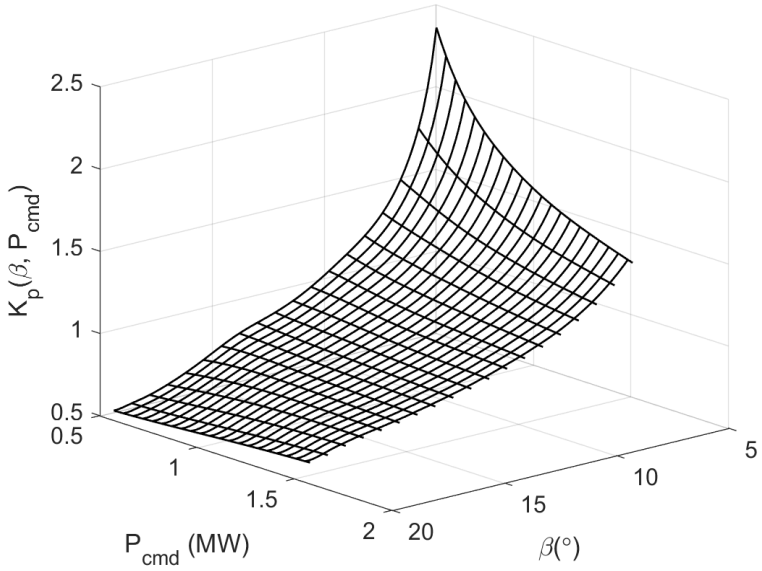

Figure 6.8: $\mathcal{H}_2$ scheduled proportional gain for the commanded power tracking pitch control of NREL 1.5 MW WindPact turbine.

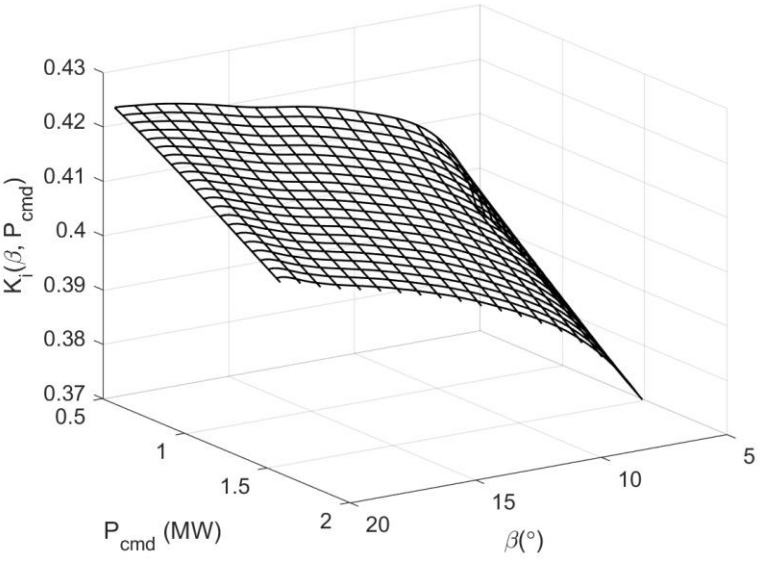

Figure 6.9: $\mathcal{H}_2$ scheduled integral gain for the commanded power tracking pitch control of NREL 1.5 MW WindPact turbine.

6.4 SIMULATION RESULTS

In this section, simulation is conducted to demonstrate the effectiveness of the proposed wind turbine controller for supporting grid frequency. Among the four subsystems of the microgrid as shown in Figure 6.1, wind turbine is located at subsystem 2 and it only has local information about the diesel generator power output and frequency. A power imbalance event is introduced by suddenly increasing or decreasing the dynamic load in subsystem 4. A 2% white noise (relative to the frequency deviation event) has been added to more effectively simulate real conditions. The high-fidelity wind turbine model provided by the NREL FAST Code [82] is used as the wind turbine simulation model integrated with a microgrid model built in MATLAB-Simulink. The NREL TurbSim Code [89] is used to generate short range wind profiles with a resolution of 0.002 second.

a. Under-frequency Event

A wind profile with mean value around 8 m/s is used in this study. At 1 second, a sudden load increase in subsystem 4 triggers an under-frequency event, which causes the grid frequency to fall below its nominal value. The power units in the system are responsible for providing extra power and stabilizing the grid frequency. Figure 6.10 compares the grid frequency responses of three different scenarios:

Scenario 1: Conventional droop control without wind turbine frequency control. The nominal wind turbine power output (0.6 MW) is equal to the initial available wind power. Baseline wind turbine controller is applied to maximize wind energy capture.

Scenario 2: Conventional droop control with the proposed wind turbine frequency control. The nominal wind turbine power output (0.6 MW) is equal to the

available wind power. Wind energy capture is maximized during normal operation when grid frequency is around its nominal value.

Scenario 3: Conventional droop control with the proposed wind turbine frequency control. The nominal wind turbine power output (0.3 MW) is lower than the available wind power. The wind turbine is deloaded during normal operation.

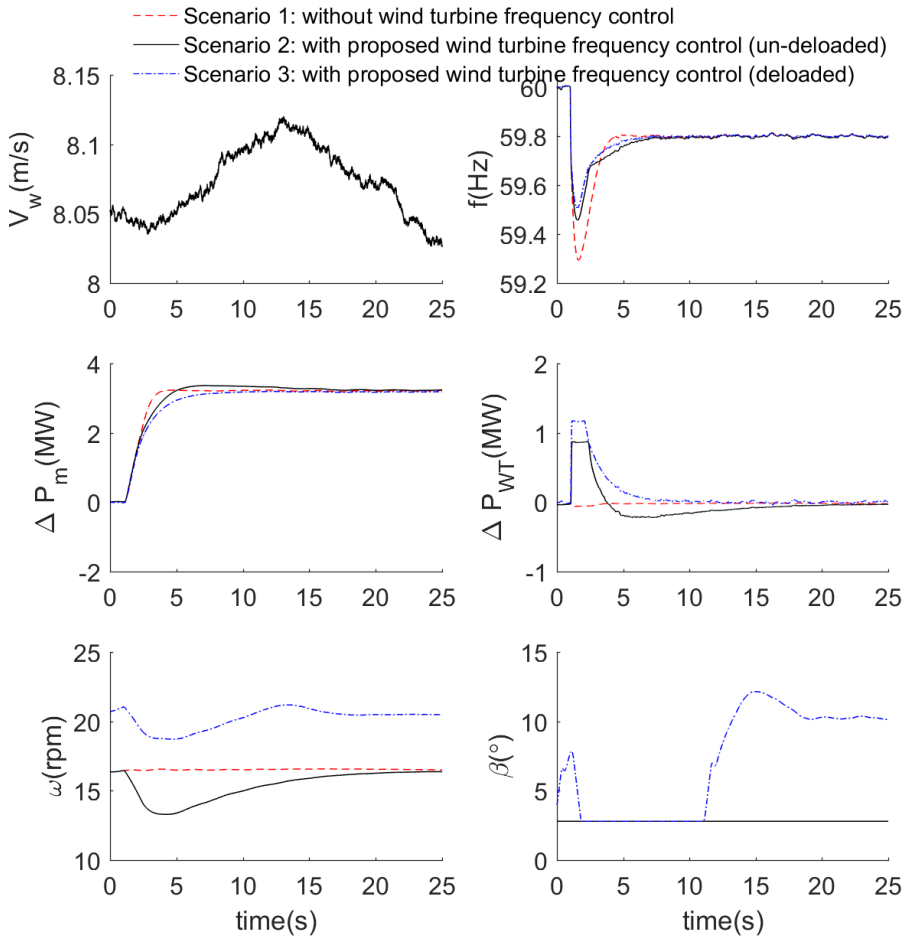

Figure 6.10: Performance comparison of droop control without and with wind turbine frequency control (un-deloaded and deloaded) following an under-frequency event.

The subplots in Figure 6.10 show the wind speed V_w, grid frequency f, conventional generator power output change (including diesel generator) from its nominal value ΔP_m, wind power output change from its nominal value ΔP_{WT}, turbine rotor speed ω and blade pitch angle β, respectively. Without the wind turbine frequency control, the conventional generators ramp up their power outputs after 3-4 seconds by droop control, resulting in a frequency dip of 59.28 Hz. With the proposed wind turbine frequency control, power is injected to the grid immediately after the frequency drop. This is achieved by slowing down the turbine rotor and releasing its rotational kinetic energy. As a result, the dip of grid frequency response is improved. Compare to Scenario 1, the proposed frequency control improves the lowest point of frequency response from 59.28 Hz to 59.46 Hz in Scenario 2. After slowing down the rotor speed, the wind turbine power output drops below the nominal power temporarily. Eventually, the wind turbine restores speed and nominal power output by withdrawing power from the grid. Unlike Scenarios 1 and 2, the wind turbine operates in deloaded mode during normal operation in Scenario 3. The wind turbine is operating around the rated speed before the under-frequency event. Immediately after the frequency drop, the blade pitch angle is adjusted to its optimal value for more wind energy capture. Also, as the turbine rotor slows down and approaches ω_{opt}, more wind energy is captured. With combined increased wind energy capture and released rotational kinetic energy, the grid frequency dip in Scenario 3 is further improved to 59.52 Hz. Additionally, the turbine rotor speed quickly restores to its rated value after the conventional generators ramp up their power outputs. Unlike Scenario 2, the deloaded wind turbine does not withdraw the power from the grid after releasing rotational kinetic energy. The rotor speed recovery is enabled by the deloaded wind power. The above simulations show that the wind turbine is more capable of supporting grid frequency with a deloaded nominal power output. However, this is at the

expense of less wind energy capture. A tradeoff analysis must be carried out for optimization of wind energy capture and frequency regulation capability.

b. Over-frequency Event

A wind profile with mean value around 9.2 m/s is used in this study. At 1 second, a sudden load decrease in subsystem 4 triggers an over-frequency event, which causes a grid frequency spike above its nominal value. The power units in the system must decrease their power outputs to stabilize the grid frequency. Figure 6.11 shows a comparison of grid frequency responses for three different scenarios:

Scenario 1: Conventional droop control without wind turbine frequency control. The nominal wind turbine power output (0.9 MW) is equal to the initial available wind power. Baseline wind turbine controller is applied to maximize wind energy capture.

Scenario 2: Conventional droop control with the proposed wind turbine frequency control. The nominal wind turbine power output (0.9 MW) is equal to the available wind power. Wind energy capture is maximized during normal operation when grid frequency is around its nominal value.

Scenario 3: Conventional droop control with the proposed wind turbine frequency control. The nominal wind turbine power output (0.6 MW) is lower than the available wind power. The wind turbine is deloaded during normal operation.

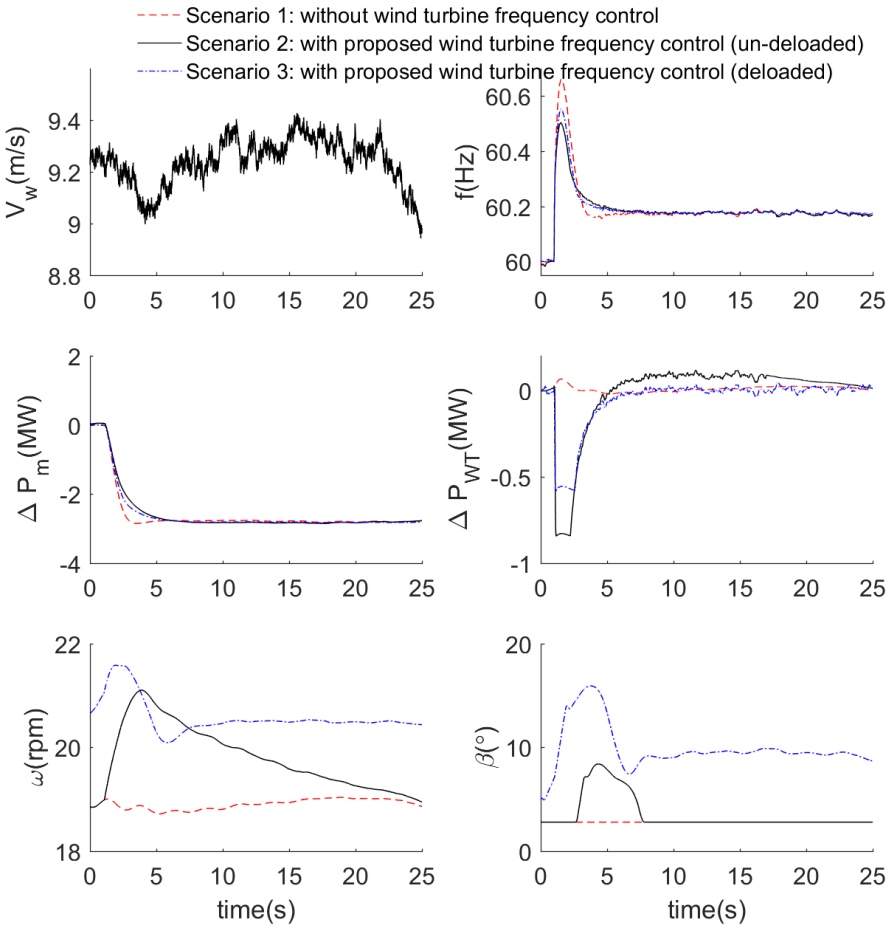

Figure 6.11: Performance comparison of droop control without and with wind turbine frequency control (un-deloaded and deloaded) following an over-frequency event.

The subplots in Figure 6.11 show the same physical parameters as Figure 6.10. As the wind speed varies more significantly, the grid frequency and wind turbine power output also experience more significant oscillations. Without wind turbine frequency control, the conventional generators implement droop control that decrease their power outputs and reaches steady state around 3-4 seconds in Scenario 1. With droop control only, the grid frequency reaches its highest point at 60.66 Hz. The proposed wind turbine frequency control is applied in Scenario 2, which takes advantage of fast wind turbine

power electronics. The wind turbine absorbs power from microgrid rapidly by accelerating the turbine rotor. As a result, the spike of grid frequency is reduced to 60.51 Hz. Eventually, the wind turbine restores to optimal power operation after the generators decrease their power outputs. The extra power stored in turbine rotor is injected back to the grid. Blade pitch controller successfully regulates the turbine rotor speed when it reaches the rated value, which prevents over-speeding. Scenario 3 shows the performances of a deloaded wind turbine frequency controller. Unlike its effect on under-frequency event, this controller worsens the grid response to over-frequency event compared to the un-deloaded case. This is due to that the deloaded wind turbine is less capable of absorbing extra power from grid with higher turbine rotor speed. In general, deloading wind turbine power output is not preferred for the case of over-frequency event.

6.5 SUMMARY

In this chapter, control designs are proposed for a wind turbine in conjunction with a diesel generator that implements primary frequency control in a microgrid. During a frequency deviation event, the diesel generator changes its power output according to its droop control. The slow response of the diesel generator may cause a deep dip and slow recovery of grid frequency. Therefore, a wind turbine is controlled in conjunction to provide extra power such that the combined power output of diesel generator and wind turbine can quickly track the droop control command. The immediate extra power is achieved by slowing down the turbine and releasing the rotational kinetic energy of the turbine rotor. The proposed wind turbine controller integrates a novel frequency supporting generator torque control and a $\mathcal{H}_2$ gain-scheduled pitch control for fast wind turbine power injection or absorption without causing wind turbine instability such as a

complete stop or over-speeding. In addition, the proposed controller demonstrates smooth control actions during transition between normal operations and frequency deviation events. The universal control design can be used for either un-deloaded or deloaded wind turbine operation based on different wind turbine nominal power outputs. Simulation results show that the proposed wind turbine control design effectively improves the grid stability by reducing the frequency deviation and recovery time following a power imbalance event. In the future work, wind turbine participation in secondary and tertiary frequency control will be studied. Also, the nominal wind turbine power output will be optimized considering the tradeoff between the wind turbine energy capture and frequency regulation capability.

Chapter 7: *Conclusions*

The key issues that increase the cost associated with wind energy include low energy conversion efficiency, high maintenance cost, wind power intermittency and its negative impact on grid frequency stability. This work is focused on wind turbine control designs to overcome the above challenges by maximizing wind energy capture, mitigating fatigue loading, overcoming wind intermittency and supporting grid frequency. The development of advanced control algorithms for wind energy systems can contribute significantly to reduction of the cost associated with wind energy.

In the first study, control algorithms are developed for wind energy capture maximization of a variable-speed wind turbine. During partial load operation, rotor speed is continuously adjusted to remain wind turbine optimal operation by manipulating the electromagnetic torque applied to the generator. In this work, a dynamic programming based real-time controller (DPRC) is developed, which uses torque and pitch control look-up tables resulting from off-line DP analysis. The DPRC has been proven to have a faster response to wind speed variation compared to the standard torque controller (STC). While DPRC may lose optimality considering model-plant mismatch, an adaptive gain modified optimal torque controller (AGMOTC) is proposed to further improve the controller robustness against model uncertainties. The AGMOTC drives the reference tip speed ratio (TSR) to its optimal value by an adaptive searching algorithm and applies the internal Proportional-Integral (PI) technique to rapidly track this reference TSR.

In the second study, fatigue loading mitigation techniques are developed to reduce the maintenance cost of a wind turbine. During partial load operation, a generator torque-based fatigue mitigation method is designed to reduce the impact of exacerbated tower bending moments due to the resonance effect. Combined AGMOTC with the fatigue

mitigation technique, the controller demonstrates improved efficiency and robustness in wind energy capture and reduced tower fatigue loading as compared to the conventional control method. During full load operation, a $\mathcal{H}_2$ optimization has been carried out for optimizing gain-scheduling for a Proportional-Integral blade pitch controller. The controller reduces the deviation between the turbine rotor speed and its rated value under volatile wind speeds, which results in mitigated drivetrain fatigue loading.

In the third study, battery energy storage systems (BESS) are integrated with wind turbines to mitigate wind intermittence and make wind power dispatchable as traditional power sources. With probabilistic wind speed forecast, a new power scheduling and real-time control approach has been proposed to improve the performance of an integrated wind turbine and battery system. The proposed algorithms significantly improves the performances of the integrated system over conventional control design with respect to maximizing energy output, mitigating power deviation from the scheduled target, limiting ramp rate, minimizing battery charging rate and reducing fatigue loads. Additionally, more significant improvements can be achieved with battery system of smaller capacity, which leads to potential reduction of battery capacity, thus the overall cost of wind energy.

Last but not least, control designs are oriented to wind turbine participation in grid primary frequency regulation. With the rise in wind turbine installations, grid stability is becoming a major challenge. The fast active power injection/absorption capability of wind turbine enables it to rapidly change its power output and stablize the grid frequency following an sudden power imbalnace event. In addition to quick response to grid frequency deviation event, the novel generator torque and blade pitch control laws avoid turbine instability such as a complete turbine shut-down or over-speeding. Simulation

results show that the proposed control design effectively improves the grid stability by reducing the frequency deviation and recovery time following a power imbalance event.

In this dissertation, various control algorithms with different objectives for reducing wind energy cost are presented. Integrating control designs considering tradeoffs between multiple objectives will be in high demand. By achieving the aforementioned control objectives and reducing the cost associated with wind energy, wind energy penetration can be further increased in the near future.

References

[1] "Studies Show Wind Power's Massive Potential," 2012. [Online]. Available: Inside Science.

[2] Global Wind Energy Council, "Global Wind Statistics 2016." [Online]. Available: http://www.gwec.net/global-figures/graphs/. [Accessed: 26-Apr-2017].

[3] S. Lindenberg, B. Smith, K. O'Dell, and others, "20% wind energy by 2030," *Natl. Renew. Energy Lab. NREL US Dep. Energy Renew. Energy Consult. Serv. Energ. Inc.*, 2008.

[4] "2015 United Nations Climate Change Conference," *Wikipedia, the free encyclopedia*. 13-Jan-2016.

[5] AWEA, "AWEA Wind Energy Agenda." [Online]. Available: http://www.awea.org/wind-energy-agenda.

[6] H. Taylor, *Large Majorities in U.S. and Five Largest European Countries Favor More Wind Farms*. The Harris Poll, Harris Interactive, 2010.

[7] "Wind Power Market, Update 2015 – Global Market Size, Average Price, Turbine Market Share, and Key Country Analysis to 2025," 2015. [Online]. Available: PR Newswire.

[8] "Monthly Energy Review." U.S. Energy Information Administration, 2016.

[9] R. Bryce, "The high cost of wind energy as a carbon-dioxide reduction method," *Manhattan Inst. Policy Res.*, vol. 11, pp. 1–9, 2011.

[10] E. W. E. Association, *Wind energy-the facts: a guide to the technology, economics and future of wind power*. Routledge, 2012.

[11] S. Eriksson, H. Bernhoff, and M. Leijon, "Evaluation of different turbine concepts for wind power," *Renew. Sustain. Energy Rev.*, vol. 12(5), no. 5, pp. 1419–1434, Jun. 2008.

[12] F. Toja-Silva, A. Colmenar-Santos, and M. Castro-Gil, "Urban wind energy exploitation systems: Behaviour under multidirectional flow conditions—Opportunities and challenges," *Renew. Sustain. Energy Rev.*, vol. 24, pp. 364–378, Aug. 2013.

[13] T. F. Ishugah, Y. Li, R. Z. Wang, and J. K. Kiplagat, "Advances in wind energy resource exploitation in urban environment: A review," *Renew. Sustain. Energy Rev.*, vol. 37, pp. 613–626, Sep. 2014.

[14] G. E. Concepts, *Market, cost, and technical analysis of vertical and horizontal axis wind turbines, Task# 2: VAWT vs. HAWT technology*. May, 2003.

[15] P. Gipe, *Wind energy basics*. Chelsea Green Pub. Co., 2009.

[16] M. L. E. N. Shaltout and others, "Optimal control of wind turbines for distributed power generation," 2015.

[17] E. H. Camm *et al.*, "Wind power plant collector system design considerations: IEEE PES wind plant collector system design working group," *2009 IEEE Power Energy Soc. Gen. Meet.*, 2009.

[18] "Pitch-regulated and Stall-regulated Wind Turbine." [Online]. Available: http://researchhubs.com/post/engineering/wind-energy/pitch-regulated-and-stall-regulated-wind-turbine.html. [Accessed: 14-Mar-2017].

[19] N. Wang, "Lidar-assisted feedforward and feedback control design for wind turbine tower load mitigation and power capture enhancement," Colorado School of Mines, 2013.

[20] J. D. Sørensen and J. N. Sørensen, *Wind energy systems: Optimising design and construction for safe and reliable operation*. Elsevier, 2010.

[21] M. A. Abdullah, A. H. M. Yatim, and C. W. Tan, "A study of maximum power point tracking algorithms for wind energy system," in *2011 IEEE First Conference on Clean Energy and Technology (CET)*, 2011, pp. 321–326.

[22] M. A. Abdullah, A. H. M. Yatim, C. W. Tan, and R. Saidur, "A review of maximum power point tracking algorithms for wind energy systems," *Renew. Sustain. Energy Rev.*, vol. 16, no. 5, pp. 3220–3227, 2012.

[23] S. M. R. Kazmi, H. Goto, H.-J. Guo, and O. Ichinokura, "Review and critical analysis of the research papers published till date on maximum power point tracking in wind energy conversion system," in *Energy Conversion Congress and Exposition (ECCE), 2010 IEEE*, 2010, pp. 4075–4082.

[24] N. Wang, K. E. Johnson, and A. D. Wright, "Comparison of Strategies for Enhancing Energy Capture and Reducing Loads Using LIDAR and Feedforward Control," *IEEE Trans. Control Syst. Technol.*, vol. 21, no. 4, pp. 1129–1142, Jul. 2013.

[25] D. Schlipf *et al.*, "Direct speed control using lidar and turbine data," in *American Control Conference (ACC), 2013*, 2013, pp. 2208–2213.

[26] D. Schlipf *et al.*, “Prospects of optimization of energy production by lidar assisted control of wind turbines,” 2011.

[27] K. G. Pierce, B. S. Gerber, and S. Herr, *Variable tip speed ratio tracking control for wind turbines*. Google Patents, 2012.

[28] K. E. Johnson, L. J. Fingersh, M. Balas, and L. Pao, “Methods for increasing region 2 power capture on a variable speed HAWT,” in *Paper No. AIAA-2004-0350, Proc. 23rd ASME Wind Energy Symposium, Reno, NV*, 2004, pp. 103–113.

[29] K. E. Johnson, L. Y. Pao, M. J. Balas, and L. J. Fingersh, “Control of variable-speed wind turbines: standard and adaptive techniques for maximizing energy capture,” *IEEE Control Syst.*, vol. 26, no. 3, pp. 70–81, Jun. 2006.

[30] Y. D. Song, B. Dhinakaran, and X. Y. Bao, “Variable speed control of wind turbines using nonlinear and adaptive algorithms,” *J. Wind Eng. Ind. Aerodyn.*, vol. 85, no. 3, pp. 293–308, Apr. 2000.

[31] J. B. Freeman and M. J. Balas, “An investigation of variable speed horizontal-axis wind turbines using direct model-reference adaptive control,” in *Proc. 18th ASME Wind Energy Symp*, 1999, pp. 66–76.

[32] E. Koutroulis and K. Kalaitzakis, “Design of a maximum power tracking system for wind-energy-conversion applications,” *IEEE Trans. Ind. Electron.*, vol. 53, no. 2, pp. 486–494, Apr. 2006.

[33] Q. Wang and L. Chang, “An intelligent maximum power extraction algorithm for inverter-based variable speed wind turbine systems,” *IEEE Trans. Power Electron.*, vol. 19, no. 5, pp. 1242–1249, Sep. 2004.

[34] S. M. Barakati, M. Kazerani, and J. D. Aplevich, “Maximum Power Tracking Control for a Wind Turbine System Including a Matrix Converter,” *IEEE Trans. Energy Convers.*, vol. 24, no. 3, pp. 705–713, Sep. 2009.

[35] A. Soetedjo, A. Lomi, and W. P. Mulayanto, “Modeling of wind energy system with MPPT control,” in *2011 International Conference on Electrical Engineering and Informatics (ICEEI)*, 2011, pp. 1–6.

[36] S. M. Raza Kazmi, H. Goto, H.-J. Guo, and O. Ichinokura, “A Novel Algorithm for Fast and Efficient Speed-Sensorless Maximum Power Point Tracking in Wind Energy Conversion Systems,” *IEEE Trans. Ind. Electron.*, vol. 58, no. 1, pp. 29–36, Jan. 2011.

[37] H. J. Sutherland, “On the fatigue analysis of wind turbines,” Sandia National Labs., Albuquerque, NM (US); Sandia National Labs., Livermore, CA (US), 1999.

[38] E. A. Bossanyi, “Wind turbine control for load reduction,” *Wind Energy*, vol. 6, no. 3, pp. 229–244, 2003.

[39] T. Burton, D. Sharpe, N. Jenkins, and E. Bossanyi, *Wind energy handbook*. John Wiley & Sons, 2001.

[40] E. A. Bossanyi, “Further load reductions with individual pitch control,” *Wind Energy*, vol. 8, no. 4, pp. 481–485, 2005.

[41] N. Wang, K. E. Johnson, and A. D. Wright, “FX-RLS-based feedforward control for LIDAR-enabled wind turbine load mitigation,” *Control Syst. Technol. IEEE Trans. On*, vol. 20, no. 5, pp. 1212–1222, 2012.

[42] F. Dunne, L. Y. Pao, A. D. Wright, B. Jonkman, and N. Kelley, “Adding feedforward blade pitch control to standard feedback controllers for load mitigation in wind turbines,” *Mechatronics*, vol. 21, no. 4, pp. 682–690, 2011.

[43] Y. Zhang, Z. Chen, and M. Cheng, “Proportional resonant individual pitch control for mitigation of wind turbines loads,” *IET Renew. Power Gener.*, vol. 7, no. 3, pp. 191–200, 2013.

[44] K. A. Stol and M. J. Balas, “Periodic Disturbance Accommodating Control for Blade Load Mitigation in Wind Turbines,” *J. Sol. Energy Eng.*, vol. 125, no. 4, p. 379, 2003.

[45] K. Z. Ostergaard, P. Brath, and J. Stoustrup, “Gain-scheduled Linear Quadratic Control of Wind Turbines Operating at High Wind Speed,” in *IEEE International Conference on Control Applications, 2007. CCA 2007*, 2007, pp. 276–281.

[46] J. Smit, “Increased Energy Yield using the Smart Rotor.”

[47] D. Schlipf, D. J. Schlipf, and M. Kühn, “Nonlinear model predictive control of wind turbines using LIDAR,” *Wind Energy*, vol. 16, no. 7, pp. 1107–1129, Oct. 2013.

[48] X. Jiang, B. Dong, L. Xie, and L. Sweeney, “Adaptive Gaussian Process for Short-Term Wind Speed Forecasting.,” in *ECAI*, 2010, pp. 661–666.

[49] C.-T. Li, H. Peng, and J. Sun, “MPC for reducing energy storage requirement of wind power systems,” in *American Control Conference (ACC), 2013*, 2013, pp. 6607–6612.

[50] B. S. Borowy and Z. M. Salameh, “Dynamic response of a stand-alone wind energy conversion system with battery energy storage to a wind gust,” *Energy Convers. IEEE Trans. On*, vol. 12, no. 1, pp. 73–78, 1997.

[51] M. Khalid and A. V. Savkin, “A model predictive control approach to the problem of wind power smoothing with controlled battery storage,” *Renew. Energy*, vol. 35, no. 7, pp. 1520–1526, 2010.

[52] V. Marano, G. Rizzo, and F. A. Tiano, “Application of dynamic programming to the optimal management of a hybrid power plant with wind turbines, photovoltaic panels and compressed air energy storage,” *Appl. Energy*, vol. 97, pp. 849–859, 2012.

[53] T.-Y. Lee, “Operating schedule of battery energy storage system in a time-of-use rate industrial user with wind turbine generators: a multipass iteration particle swarm optimization approach,” *Energy Convers. IEEE Trans. On*, vol. 22, no. 3, pp. 774–782, 2007.

[54] T.-Y. Lee, “Operating schedule of battery energy storage system in a time-of-use rate industrial user with wind turbine generators: a multipass iteration particle swarm optimization approach,” *Energy Convers. IEEE Trans. On*, vol. 22, no. 3, pp. 774–782, 2007.

[55] P. Nema, R. K. Nema, and S. Rangnekar, “A current and future state of art development of hybrid energy system using wind and PV-solar: A review,” *Renew. Sustain. Energy Rev.*, vol. 13, no. 8, pp. 2096–2103, 2009.

[56] U. Focken, M. Lange, K. Mönnich, H.-P. Waldl, H. G. Beyer, and A. Luig, “Short-term prediction of the aggregated power output of wind farms—a statistical analysis of the reduction of the prediction error by spatial smoothing effects,” *J. Wind Eng. Ind. Aerodyn.*, vol. 90, no. 3, pp. 231–246, 2002.

[57] Y. Jeong, K. Johnson, and P. Fleming, “Comparison and testing of power reserve control strategies for grid-connected wind turbines,” *Wind Energy*, vol. 17, no. 3, pp. 343–358, 2014.

[58] J. Aho, A. Buckspan, L. Pao, P. Fleming, and others, “An active power control system for wind turbines capable of primary and secondary frequency control for supporting grid reliability,” in *Proc. 51st AIAA Aerospace Sciences Meeting Including the New Horizons Forum and Aerospace Exposition*, 2013.

[59] E. Ela *et al.*, *Active Power Controls from Wind Power: Bridging the Gap*. National Renewable Energy Laboratory, 2014.

[60] J. M. Jonkman, S. Butterfield, W. Musial, and G. Scott, *Definition of a 5-MW reference wind turbine for offshore system development*. National Renewable Energy Laboratory Golden, CO, 2009.

[61] S. De Rijcke, P. Tielens, B. Rawn, D. Van Hertem, and J. Driesen, “Trading Energy Yield for Frequency Regulation: Optimal Control of Kinetic Energy in Wind Farms,” *IEEE Trans. Power Syst.*, vol. 30, no. 5, pp. 2469–2478, Sep. 2015.

[62] J. Aho *et al.*, “A tutorial of wind turbine control for supporting grid frequency through active power control,” in *American Control Conference (ACC), 2012*, 2012, pp. 3120–3131.

[63] K. V. Vidyanandan and N. Senroy, “Primary frequency regulation by deloaded wind turbines using variable droop,” *IEEE Trans. Power Syst.*, vol. 28, no. 2, pp. 837–846, May 2013.

[64] A. D. Hansen, “Evaluation of power control with different electrical and control concept of wind farm: Part 2–Large systems,” Project UpWind, 2010.

[65] J. Ekanayake and N. Jenkins, “Comparison of the response of doubly fed and fixed-speed induction generator wind turbines to changes in network frequency,” *IEEE Trans. Energy Convers.*, vol. 19, no. 4, pp. 800–802, Dec. 2004.

[66] J. Morren, J. Pierik, and S. W. H. de Haan, “Inertial response of variable speed wind turbines,” *Electr. Power Syst. Res.*, vol. 76, no. 11, pp. 980–987, Jul. 2006.

[67] M. Kayikci and J. V. Milanovic, “Dynamic Contribution of DFIG-Based Wind Plants to System Frequency Disturbances,” *IEEE Trans. Power Syst.*, vol. 24, no. 2, pp. 859–867, May 2009.

[68] E. Loukarakis, I. Margaris, and P. Moutis, “Frequency control support and participation methods provided by wind generation,” in *2009 IEEE Electrical Power Energy Conference (EPEC)*, 2009, pp. 1–6.

[69] R. G. de Almeida and J. A. P. Lopes, “Participation of Doubly Fed Induction Wind Generators in System Frequency Regulation,” *IEEE Trans. Power Syst.*, vol. 22, no. 3, pp. 944–950, Aug. 2007.

[70] L. Johnston, F. Díaz-González, O. Gomis-Bellmunt, C. Corchero-García, and M. Cruz-Zambrano, “Methodology for the economic optimisation of energy storage systems for frequency support in wind power plants,” *Appl. Energy*, vol. 137, pp. 660–669, Jan. 2015.

[71] S. K. Pandey, S. R. Mohanty, and N. Kishor, “A literature survey on load–frequency control for conventional and distribution generation power systems,” *Renew. Sustain. Energy Rev.*, vol. 25, pp. 318–334, Sep. 2013.

[72] L. Liang, J. Zhong, and Z. Jiao, “Frequency regulation for a power system with wind power and battery energy storage,” in *Power System Technology (POWERCON), 2012 IEEE International Conference on*, 2012, pp. 1–6.

[73] J. W. Choi, S. Y. Heo, and M. K. Kim, “Hybrid operation strategy of wind energy storage system for power grid frequency regulation,” *IET Gener. Transm. Distrib.*, 2015.

[74] H. Bevrani, A. Ghosh, and G. Ledwich, “Renewable energy sources and frequency regulation: survey and new perspectives,” *IET Renew. Power Gener.*, vol. 4, no. 5, pp. 438–457, Sep. 2010.

[75] L. Xie *et al.*, “Wind Integration in Power Systems: Operational Challenges and Possible Solutions,” *Proc. IEEE*, vol. 99, no. 1, pp. 214–232, Jan. 2011.

[76] Z. Ma, Z. Yan, M. L. Shaltout, and D. Chen, “Optimal Real-Time Control of Wind Turbine During Partial Load Operation,” *Control Syst. Technol. IEEE Trans. On*, vol. 23, no. 6, pp. 2216–2226, 2015.

[77] Z. Ma, M. L. Shaltout, and D. Chen, “Adaptive Gain Modified Optimal Torque Controller for Wind Turbine Partial Load Operation,” p. V002T18A002, Oct. 2014.

[78] Z. Ma, M. L. Shaltout, and D. Chen, “An Adaptive Wind Turbine Controller Considering Both the System Performance and Fatigue Loading,” *J. Dyn. Syst. Meas. Control*, vol. 137, no. 11, p. 111007, 2015.

[79] M. L. Shaltout, Z. Ma, and D. Chen, “An economic model predictive control approach using convex optimization for wind turbines,” in *2016 American Control Conference (ACC)*, 2016, pp. 3176–3181.

[80] Z. Ma, M. L. Shaltout, and D. Chen, “Optimal Power Dispatch and Control of an Integrated Wind Turbine and Battery System,” *J. Dyn. Syst. Meas. Control*, Mar. 2017.

[81] Z. Ma and D. Chen, “Optimal power dispatch and control of a wind turbine and battery hybrid system,” in *American Control Conference (ACC), 2015*, 2015, pp. 3052–3057.

[82] J. M. Jonkman and M. L. Buhl Jr, “FAST user’s guide,” *Natl. Renew. Energy Lab. Gold. CO Tech. Rep. No NRELEL-500-38230*, 2005.

[83] G. Bywaters, “Northern Power Systems WindPACT Drive Train Alternative Design Study Report,” 2004.

[84] J. F. Hall and D. Chen, “Dynamic Optimization of Drivetrain Gear Ratio to Maximize Wind Turbine Power Generation—Part 1: System Model and Control Framework,” *J. Dyn. Syst. Meas. Control*, vol. 135, no. 1, p. 011016, 2013.

[85] D. Palejiya, J. Hall, C. Mecklenborg, and D. Chen, “Stability of Wind Turbine Switching Control in an Integrated Wind Turbine and Rechargeable Battery System: A Common Quadratic Lyapunov Function Approach,” *J. Dyn. Syst. Meas. Control*, vol. 135, no. 2, pp. 021018–021018, Feb. 2013.

[86] J. F. Hall and D. Chen, “Control of a variable ratio gearbox and mechanical brake to maximize wind energy production,” in *American Control Conference (ACC), 2012*, 2012, pp. 3014–3019.

[87] S. Heier, *Grid integration of wind energy conversion systems*. Wiley, 1998.

[88] M. Harris, M. Hand, and A. Wright, “Lidar for turbine control,” *Natl. Renew. Energy Lab. Gold. CO Rep. No NRELTP-500-39154*, 2006.

[89] B. J. Jonkman and M. L. Buhl, “Turbsim user’s guide,” *Nat Renew Energy Lab Gold. CO USA Tech Rep NRELEL-500-36970*, 2004.

[90] P. Brath, J. Stoustrup, and others, “Estimation of effective wind speed,” in *Journal of Physics: Conference Series*, 2007, vol. 75, p. 012082.

[91] M. L. Buhl, “WT_Perf user’s guide,” *Natl. Wind Technol. Cent. Natl. Renew. Energy Lab. Gold. CO*, 2004.

[92] C. Modes, “User’s Guide to BModes,” 2007.

[93] D. L. Elliott, C. G. Holladay, W. R. Barchet, H. P. Foote, and W. F. Sandusky, “Wind energy resource atlas of the United States,” *NASA STIRecon Tech. Rep. N*, vol. 87, p. 24819, 1987.

[94] J. F. Manwell, J. G. McGowan, and A. L. Rogers, *Wind energy explained: theory, design and application*. John Wiley & Sons, 2010.

[95] H. Gerber and M. L. Buhl, “MLife User’s Guide,” *Natl. Renew. Energy Lab. Gold. CO USA*, 2012.

[96] S. M. Pandit, S.-M. Wu, and others, *Time series and system analysis with applications*. Wiley New York, 1983.

[97] “Modern estimation of the parameters of the Weibull wind speed distribution for wind energy analysis.” [Online]. Available:

http://www.sciencedirect.com.ezproxy.lib.utexas.edu/science/article/pii/S0167610599001221. [Accessed: 19-Mar-2017].

[98] S. Y. D. Dubey, "Normal and Weibull distributions," *Nav. Res. Logist. NRL*, vol. 14, no. 1, pp. 69–79, 1967.

[99] T. J. Cole, "The LMS method for constructing normalized growth standards.," *Eur. J. Clin. Nutr.*, vol. 44, no. 1, pp. 45–60, 1990.

[100] D. Garson, *Testing statistical assumptions*. North Carolina: Statistical associates Publishing, 2012.

[101] S. S. Choi and H. S. Lim, "Factors that affect cycle-life and possible degradation mechanisms of a Li-ion cell based on LiCoO2," *J. Power Sources*, vol. 111, no. 1, pp. 130–136, 2002.

[102] D. Lew, "NREL: Western Wind Resources Dataset." [Online]. Available: http://wind.nrel.gov/public/WWIS/Wind_Data/. [Accessed: 03-Feb-2017].

[103] M. Scheuerer, D. Möller, and others, "Probabilistic wind speed forecasting on a grid based on ensemble model output statistics," *Ann. Appl. Stat.*, vol. 9, no. 3, pp. 1328–1349, 2015.

[104] P. Economics, *State of the Market Report for the MISO electricity markets*. Report, 2010.

[105] S. W. Smith and others, "The scientist and engineer's guide to digital signal processing," 1997.

[106] R. H. Lasseter and P. Paigi, "Microgrid: A conceptual solution," in *Power Electronics Specialists Conference, 2004. PESC 04. 2004 IEEE 35th Annual*, 2004, vol. 6, pp. 4285–4290.

[107] M. Yazdanian and A. Mehrizi-Sani, "Distributed Control Techniques in Microgrids," *IEEE Trans. Smart Grid*, vol. 5, no. 6, pp. 2901–2909, Nov. 2014.

[108] M. Shahabi, M. R. Haghifam, M. Mohamadian, and S. A. Nabavi-Niaki, "Microgrid Dynamic Performance Improvement Using a Doubly Fed Induction Wind Generator," *IEEE Trans. Energy Convers.*, vol. 24, no. 1, pp. 137–145, Mar. 2009.

[109] J. M. Mauricio, A. Marano, A. Gomez-Exposito, and J. L. M. Ramos, "Frequency Regulation Contribution Through Variable-Speed Wind Energy Conversion Systems," *IEEE Trans. Power Syst.*, vol. 24, no. 1, pp. 173–180, Feb. 2009.

[110] A. Zertek, G. Verbic, and M. Pantos, “A Novel Strategy for Variable-Speed Wind Turbines’ Participation in Primary Frequency Control,” *IEEE Trans. Sustain. Energy*, vol. 3, no. 4, pp. 791–799, Oct. 2012.

Vita

Zheren Ma was born in Suzhou, China and he received the B.S. degree in Mechanical Engineering with special focus on mechatronics from Shanghai Jiaotong University, Shanghai, China, in 2013. After graduation, he started his Ph.D. program in Mechanical Engineering from University of Texas at Austin. His current research interests include modeling and control strategy development for renewable energy systems, drilling mechanics or hydraulics systems as well as physiological systems.

Email: zhrm@utexas.edu

This manuscript was typed by the author.